12-2013

CHARACTERIZATION OF OSLDS FOR USE IN SMALL FIELD PHOTON BEAM DOSIMETRY

Christopher Pham

CHARACTERIZATION OF OSLDS FOR USE IN SMALL FIELD PHOTON BEAM DOSIMETRY

by

Christopher Loi Pham, B.S.

APPROVED:

David Followill, Ph.D.
Supervisory Professor

Stephen Kry, Ph.D.

Paola Alvarez, M.S.

Peter Balter, Ph.D.

Dershan Luo, Ph.D.

Francesco Stingo, Ph.D.

APPROVED:

Dean, The University of Texas
Graduate School of Biomedical Sciences at Houston

CHARACTERIZATION OF OSLDS FOR USE IN SMALL FIELD PHOTON BEAM DOSIMETRY

A

THESIS

Presented to the Faculty of
The University of Texas
Health Science Center at Houston
and
The University of Texas
M.D. Anderson Cancer Center
Graduate School of Biomedical Sciences
in Partial Fulfillment

of the Requirements

for the Degree of

MASTER OF SCIENCE

By

Christopher Loi Pham, B.S.
Houston, TX

December 2013

Acknowledgements

I would like to first thank my advisor, Dr. David Followill, for this tremendous opportunity to work at the RPC and on a project that will help achieve the RPC's mission. His patience and guidance throughout this study along with his inexplicable knowledge of the subject matter stimulate my curiosity and helped me grow as a Medical Physicist. I would also like to thank my committee members: Dr. Stephen Kry, Paola Alvarez, Dr. Dershan Luo, Dr. Peter Balter, and Dr. Francesco Stingo. Dr. Kry wrote the Monte Carlo code necessary for my project and assisted in data analysis. Paola was pivotal mentor for my project, spending countless hours educating me about OSLD, data analysis, and helping me perform irradiations deep into the night. Dr. Luo provided clinical expertise in the subject matter that was useful throughout the project. Dr. Balter trained me on how to operate a linac and provided me with machine data that I otherwise would not be able to obtain. Dr. Stingo's statistical knowledge helped in data analysis that was crucial in any scientific work.

My project would not be complete if it weren't for the RPC staff. They trained me on the OSLD system, provided me with materials needed for the project, and helped me ship my phantom to institutions nationwide. I would also like to thank John Costales for building everything I used for this project from the phantom to the tools used to make the masks.

I want to thank my fellow classmates at the RPC Elizabeth McKenzie, Olivia Huang, and Jim Neihart for providing me insight to my project and other science related topics.

Lastly I want to thank my entire family, Minh, Helene, Sylvia, Sophia, Johnson, Simon, Syrus, Sienna, and Joshua, for supporting me these past few years. I specifically want to thank my dad, through the hardships he endured this past year, he continued to stay positive. To my loving grandma, you have taught me so much and I will truly miss you. Their strength, love, and support kept me motivated throughout graduate school.

CHARACTERIZATION OF OSLDS FOR USE IN SMALL FIELD PHOTON BEAM DOSIMETRY

Christopher Loi Pham, B.S.

Supervisory Professor: David Followill, Ph.D.

Abstract

The goal of this study was to redesign a Radiological Physics Center (RPC) mailable remote audit tool used for stereotactic radiosurgery (SRS) single beam dosimetry. A prototype phantom was designed and built housing nanoDot (Landauer Inc., Glenwood, IL) Al_2O_3:C optically stimulated luminescence dosimeters (OSLDs) whose visible active luminescent area has been masked. The phantom has two measurement points with two OSLDs at each location and a film insert for localization purposes only. The masked OSLDs were characterized accounting for various correction factors associated with OSLD dose calculations. The uncertainties for each correction factor were also investigated. It was determined that the linearity, depletion, fading, and energy correction factors were identical to the RPC commissioning data for non-masked OSLDs. The element correction factor (ECF) for masked OSLDs must be determined separately. Two new correction factors were introduced to the OSL dose calculation formula, scatter and field size dependence factor. The field size dependence factor was proven to be unity. The minimum field size the masked OSLD system can accommodate as an audit tool was determined to be 10 mm diameter field for circular cones or 1 x 1

cm^2 field sizes. The overall system uncertainty was 3.72% (95% C.I.) for irradiations performed using a 1 x 1 cm^2 field size. The uncertainty was suitable in advocating a ±5% acceptance criterion for RPC remote audits. Feasibility studies were performed at various locations on multiple SRS treatment configurations. CyberKnife, linac based cones, and MLC trial audits produced an average RPC OSLD measured to institution reported dose ratio of 0.982 with a standard deviation of 0.036.

Table of Contents

List of Figures

List of Tables

List of Equations

1 Introduction

1.1 Statement of the Problem

Small photon fields have seen an increase use in modern radiotherapy techniques specifically in stereotactic procedures and large uniform and nonuniform fields composed of small fields. Technological advances in linear accelerator design such as the Brainlab m3 (Brainlab Inc., Feldkirchen, Germany) micro multileaf collimator (mMLC) with thin leaf sizes and stereotactic specific treatment units including the CyberKnife (Accuray Inc., Sunnyvale, CA) and Gamma Knife (Elekta Instrument, Stockholm, Sweden) have enabled small field delivery. With small field sizes comes the potential for greater dosimetric errors due to the partial occlusion of the photon beam source, lack of lateral charged particle equilibrium, and volume averaging. Stereotactic radiosurgery delivers large doses in small number of fractions to a target. Dosimetric deviations can result in increased normal tissue toxicity and reduced local tumor control. The need for a remote audit tool to verify planned dose delivered by an institution is essential in reducing errors and maintaining consistency between institutions participating in clinical trials.

The Radiological Physics Center (RPC) ensures dosimetric accuracies at institutions participating in National Cancer Institute (NCI) funded clinical trials. They employ many audit tools to achieve this goal that includes mailed optically stimulated luminescence detectors (OSLD) for external beam output verification. In addition to the reference beam OSLD audits, the RPC also currently has a small field size single beam photon phantom that uses thermoluminescence detectors

(TLD) instead of OSLD. This small field size audit phantom features a 3 mm diameter TLD packet at two depths (1.5 and 7.5 cm) and the capability to include film. However, since the RPC is currently transitioning from TLDs to OSLDs as their primary passive detector for use in small field dosimetry, the RPC is investigating the use of OSLD to verify small field size dosimetry.

The use of TLDs by the medical physics community has an extensive history and was the passive detector of choice for decades. TLD had a range of uses from *in vivo* dosimetry to a remote audit tool[1] with good accuracy and precision[2]. However, there are many drawbacks to using TLDs including one time use, cost, long waiting periods before reading, and energy dependence. OSLDs have addressed many of the problems associated with TLDs that make them a good replacement. The equivalent accuracy and lower uncertainty, makes OSLD a dependable remote audit dosimeter[3-5]. To date, there is a lack of published data on the use of OSLD in small field dosimetry. This project looks to investigate the use of OSLD in small field dosimetry, particularly the novel idea of masking the OSLD's active area, thereby allowing the RPC to measure and verify the output for even smaller field sizes as part of the RPC's remote audit tool program.

1.2 Background

1.2.1 Stereotactic Radiosurgery

Stereotactic radiosurgery (SRS) uses high energy ionizing radiation delivered using a single fraction with small field sizes to treat intracranial and certain spine lesions and provides a noninvasive treatment tool compared with using a surgical knife. First developed by Lars Leksell in the 1940s, orthovoltage SRS was first

used to treat dysfunctional loci in the brain[6]. In the following years, megavoltage (MV) beams were used in the first 3-D treatment of a brain lesion in 1948 and the first frame-based treatment occurred in 1956. SRS is used for, but not limited to, treating single metastasis[7], isolated primary brain tumors[8], arteriovenous malformations[9], and tumors such as pituitary adenoma and acoustic neuroma[10]. There are currently three modalities of SRS treatment: heavy charged particles, cobalt 60 gamma-rays, and megavoltage x-rays[11] of which x-rays are the most commonly used and are investigated in this work. Intracranial treatments start by immobilizing the patient's head by using either a stereotactic frame mounted on the patient's skull or frameless mask setup. A computed tomography (CT) and/or magnetic resonance imaging (MRI) scan is taken where the tumor can be localized. These images are transferred to the treatment planning system which will calculate the correct dose distribution to the localized tumor while minimizing dose to the surrounding normal tissue.

Dosimetric and spatial accuracy are key factors in SRS treatments. Linear accelerator (linac) based SRS treatments use multiple noncoplanar beam arcs converging on the machine isocenter[11]. The machine isocenter may not be a point but in reality it is a sphere due to the three rotational axes from the gantry, table, and collimator. The size of the sphere needs to be as small as possible with the common value of 1mm diameter for SRS[12]. The dose distribution can be tailored to the shape of the lesion using multiple arc angles and weights with multiple isocenters for cones or shaping the aperture dynamically with a MLC[11] thus the need for accurate doses at the correct location. Another important aspect in spatial

accuracy is patient positioning. Patients are positioned by using the imaging device, lasers, and a floor stand with a set or bearings attached to the collimator system to account for any gantry rotation uncertainties[12]. These three tools help to ensure the patient is setup correctly and aligned to the nominal isocenter.

Small field sizes used in SRS treatments are shaped by either circular collimators or MLC each with their advantages and disadvantages. Circular beams produce sharper beams with higher dose gradients for small fields. Circular collimators tend to be closer to the patient, therefore reducing the penumbra of the beam[11]. The sharp dose falloffs achieved by SRS treatments result in minimizing the dose to adjacent organs at risk. Circular collimators come in various sizes ranging from 5 mm to 60 mm diameter and are typically comprised of tungsten alloy. Mini or micro multileaf collimators (mMLC) are also used in SRS where the individual leaves have widths between 2 and 5 mm[13]. Mini MLCs can conform to the shape of the lesion by moving its individual leaves. The leaves can automatically shape the lesion as the gantry rotates.

Brain metastases vary in size, and may be spherical or non-spherical in shape. When treating spherical targets, isodose distributions and dose volume histograms for both mMLCs and circular collimators are typically similar[14-15] with an advantage to circular collimators used to treat small symmetric lesions[16]. Lesions smaller than 1cm are typically not treated with mMLCs due to the leaf widths producing jagged field edges[13]. For larger lesions both mMLCs and circular collimators can be used. However, mMLCs have been shown to accurately conform isodose distributions to non-spherical and large targets resulting in better

organ at risk sparing as compared to dose distributions delivered using circular collimators[17]. mMLCs provide a more homogeneous dose distribution as compared to circular collimators when treating large lesions due to large dose inhomogeneities caused by field overlap within the target when using circular collimators. Lethal dose to normal tissue and brain toxicity can occur with using circular collimators for treating non-spherical tumors[12-13].

1.2.2 Small Field Dosimetry

Small radiation fields, defined as field sizes less than 3 cm x 3 cm[18], have seen increased usage due to the advent of improved treatment techniques specifically used for SRS such as the Gamma Knife, CyberKnife, IMRT, etc. Therefore, radiation dose accuracy for these small fields is essential in treatment planning. Multiple errors have been reported in SRS treatments throughout the years including: incorrect calibration of linacs, cranial localization errors, and backup jaws set incorrectly for cones[16]. Das et al.[19] saw a 12% difference in output factor at various institutions while Li et al.[20] reported a 5% difference in percent depth dose (PDD) values for a 6 mm x 6 mm field size for the same linac at multiple institutions. Based on these incidents alone, accurate small field dosimetry is essential to safely deliver radiotherapy to patients.

Several dosimetry measurement challenges have been documented when dealing with small field sizes due to the lack of lateral charged particle equilibrium, partial blocking of the beam source, and volume averaging[18]. Lateral charged particle disequilibrium occurs if the beam has high energy or in narrow fields where the maximum range of secondary electrons is greater than the width of the beam[21].

Electrons scattered beyond the beam edges are not necessarily compensated for by electrons scattered back within the defined radiation field size. In addition, smaller field sizes result in less of the flattening filter being seen by the point of measurement causing the number of primary photons reaching the measurement point to be reduced. The partial occlusion of the beam limits the size of detectors that can be used to measure small fields. Lack of charged particle equilibrium and source occlusion leads to a drop in dose along the central axis and overlapping penumbrae results in the full width at half maximum not equal to the collimator setting[21]. In addition, the presence of the detector produces perturbation of charged particle fluence which is hard to quantify[18,21]. Radiation detectors produce a signal averaged across its detector volume. For large field sizes, these detectors measure a mostly homogeneous section of the beam avoiding the penumbra region and thus a constant signal across the detector. However, with small field sizes, a chamber that is too large will measure a radiation field that is not constant across its detecting volume due to the penumbra and sharp fall off with these small fields. Penumbra width as defined by the distance between the 20% and 80% dose lines narrows dramatically as the collimator field size decreases[21] therefore increasing the curvature at the peak of the dose profile[22]. In small fields, measuring the penumbra can occur which leads to volume averaging and, in addition to the lack of lateral charged particle equilibrium and source occlusion, results in a drop in output[21].

There are many commercially available radiation detectors that have been manufactured specifically for use in small field dosimetry. Micro-ionization

chambers, diodes, film, diamond detectors, MOSFETs, TLDs, and gel have the potential to measure small fields but choosing the correct dosimeter can be challenging. Clinical practice has indicated that when multiple dosimeters are used, the detector with the highest measured value is used sometimes and at other times the average value for all the detectors is used[23]. Many authors[24-28] have also used Monte Carlo dose calculations to compare their simulations with measured data. Monte Carlo must be used with caution and should always be accompanied and benchmarked with experimental data to rule out any uncertainties with the particle transport characteristics, detector and radiation geometry modelling[21,53].

A key component to accurate dosimetry measurements in small fields is the positioning of the dosimeter within the field. Since there is a minimal or no dose plateau in the center of these small fields, it is very important that the sensitive volume of the small detector be placed as centered in the field as possible to locate the sensitive volume with the flattest part of the dose distribution. Figure 1.1 shows a small field dose profile of a 5 mm diameter field. Positioning should be checked at shallow and deep depths such that the detector does not deviate as it moves to different depths in a water phantom[29].

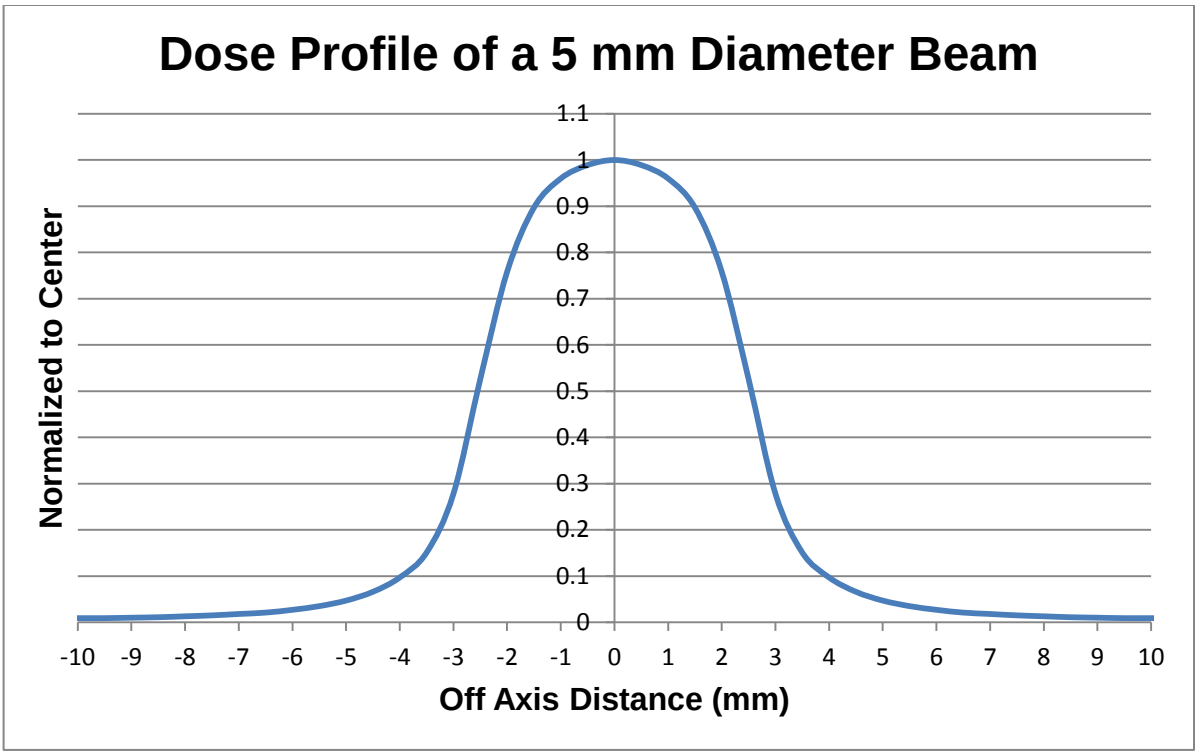

Figure 1.1: Dose profile for a 5 mm diameter field defined by a circular collimator. The lack of a flat plateau can be seen in the dose profile.

1.2.3 Radiological Physics Center

The Radiological Physics Center's (RPC) mission is to ensure consistency and dosimetric accuracy in radiation therapy from institutions participating in clinical trials. Founded in 1968[30] and funded by the National Cancer Institute (NCI), the RPC's objective is to assure NCI and the Cooperative Groups that these institutions across the United States and overseas are delivering clinically comparable and consistent radiation doses.

The RPC's mission is accomplished through a variety of ways that range from a mailed remote dosimetry program to an onsite visit to a participating institution by an RPC physicist. The remote dosimetry program initially started using thermoluminescent dosimeters (TLDs) in 1977 but in 2010 transitioned to optically

stimulated luminescent dosimeters (OSLDs)[31]. The OSLD technology is beneficial to the mailed dosimetry program due to simpler readout procedures, nondestructive readout, minimal fading, and minimal energy dependence, and reuse of the dosimeter. Examples of the mailable acrylic miniphantoms that contain the dosimeters are shown in Figure 1.2. The RPC monitors approximately 14,000 photon, electron, and proton beams per year at over 1,900 institutions through its remote beam audit program using OSLD[30].

Figure 1.2: Examples of two acrylic miniphantoms used by the RPC as a remote audit tool for external beam. Miniphantoms for photons (A) and electrons (B) are shown.

The RPC currently uses a full block phantom to remotely measure and verify small field dosimetry. The current small field dosimetry TLD full phantom is shown in Figure 1.3. The advantage with this system is that the backscatter factor is accounted for as opposed to the miniphantoms where the backscatter factor must be incorporated into the dose calculation. However, the full phantom does have its disadvantages. Its large size and various parts makes it non ideal for measuring different energies in a timely manner. For quick and easy measurements for various energies, the RPC sends out the miniphantoms. The full block phantom was intended to be used only for small field sizes. The current system houses a 3

mm diameter TLD packet as seen in Figure 1.3. With the growing use of small fields in radiation therapy, the RPC wants to transition to OSLDs as a remote audit tool for small photon beam fields.

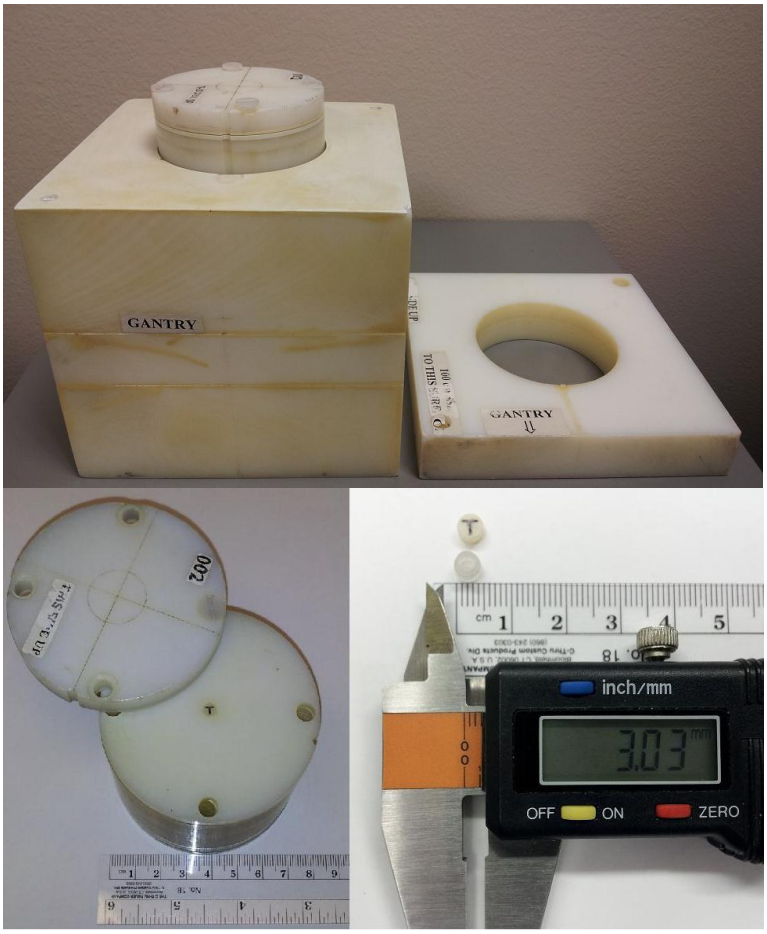

Figure 1.3: TLD full block phantom. Top – TLD cylindrical insert with base and lid. Bottom left – TLD cylindrical insert with TLD bucket in the center. Bottom right – Diameter of the TLD bucket.

1.2.4 Optically Stimulated Luminescence Dosimeters (OSLDs)

1.2.4.1 Introduction to OSLDs

Optically stimulated luminescence dosimeters have seen an increase in popularity as personnel dosimeters in the past decade. First proposed in the 1950s[32], OSLDs are now well established and are commercially available[33]. OSL

has been used in archeology as a dating tool to estimate environmental dose from natural minerals that have been around for thousands of years[34]. OSL is similar to thermoluminescence where ionizing radiation creates an electron hole pair in the material. Charges migrate from the valence band to the conduction band and fall into energy traps that are energetically between these bands. External stimulation leads to electron-hole recombination that releases photons in the optical range. The introduction of Al_2O_3:C (carbon doped aluminum oxide)[35] provided a practical material for OSL to be used as a radiation dosimeter. Carbon doped aluminum oxide was initially intended for use as a thermoluminescent material due to its high sensitivity. The high sensitivity due to carbon doping and other attractive factors makes OSLDs favorable as a personnel dosimeter. Carbon doped aluminum oxide OSLDs were first commercially available in 1998 and introduced by Landauer Inc. OSLDs are used in multiple ways today from *in vivo* dosimetry to personnel dose monitoring with film badges to verification of radiotherapy or diagnostic beam dose rates. Landauer's nanoDot OSLDs were initially designed for patient dosimetry but are now used as a point dose radiation detector throughout the medical physics community.

1.2.4.2 Phenomenon of OSL

Optically stimulated luminescence detectors are similar to thermoluminescent detectors in that they both share the same dosimetric mechanism. OSL and TLD require ionizing radiation to create an electron hole pair in the material. Charges migrate to the valence and conduction band and fall into energy traps. External stimulation releases photons in the optical range. Two energy bands, conduction

and valence, are separated by a forbidden band. The forbidden band or band gap is essential in OSL and TL processes. The crystal lattice structure is purposely produced with imperfections during fabrication, resulting in local energy bands, called traps, in the forbidden band[36]. The traps act as luminescent centers where light is emitted when an electron and hole recombine[37]. Ionizing radiation that interacts with the crystal excites an electron from the valence band causing the electron to move to the conduction band and leaving a hole in the valence band. This event, Process 1, is depicted in Figure 1.4.

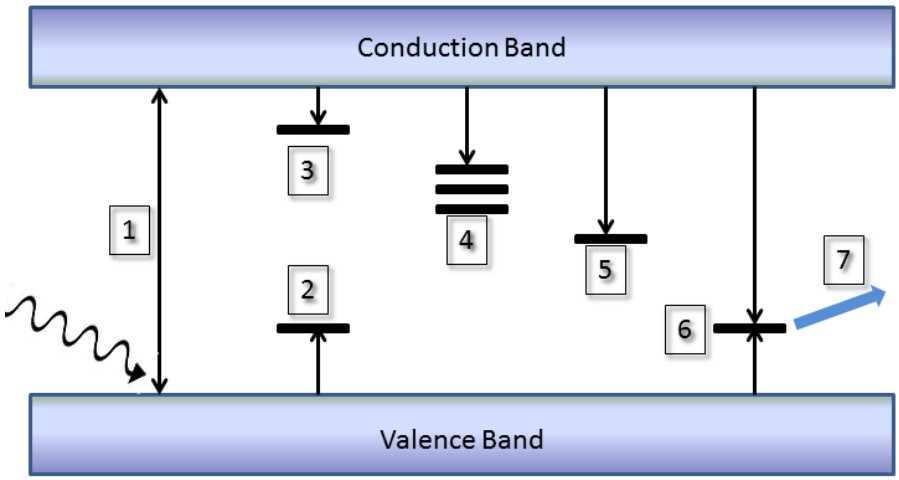

Figure 1.4: OSL process diagram. Ionizing radiation (sinuous arrow) excites an electron to the conduction band and a hole to the valence band indicated by Process 1. The hole combines with an F-center in Process 2. Process 3 are the shallow traps. Process 4 are the dosimetric traps. Process 5 are the deep traps. The photostimulated electron combines with a hole at the F^+-center in Process 6 where it will relax and emit a measureable blue light shown in Process 7.

The electrons that migrate to the conduction band are free to move in the crystal lattice but tend to either fall back to the valence band and recombine with a hole or fall into a trap caused by a defect in the crystal. The trapped charge concentration at localized energy levels is proportional to the total absorbed dose.

Electrons in the conduction band can fall into the shallow traps depicted as Process 3 in Figure 1.4. These shallow traps are localized energy levels close to the edge of the conduction band[33]. The electron's proximity to the conduction band allows it to jump back to it from the shallow traps promptly after irradiation. The probability of electrons escaping these traps is high even at room temperature. Signal is consequently lost in the shallow traps due to a decrease in charge concentrations at these energy levels following irradiation. Therefore, a delay on the order of days is necessary for the OSL signal to stabilize. During the readout process, OSL signal is initially increased after optical stimulation. The stimulated electrons from the dosimetric trap or medium traps are captured by the shallow traps. The signal will eventually stabilize once the shallow traps have been filled and the number of electrons captured by the shallow traps equals the number of electrons leaving them[33].

Medium traps, the most important traps for dosimetry, are located between the shallow and deep traps. The medium traps are depicted as Process 4 in Figure 1.4. The medium traps are also known as dosimetric traps because the levels are used in dosimetry. Several trap layers are depicted because there is a spectrum light that can optically stimulate electrons out of the OSL trap layers[38]. The energies at the dosimetric traps are stable at room temperature for extended period of time but are not so deep that charge cannot be released with visible light[39].

Deep traps, depicted as Process 5 in Figure 1.4, are the furthest from the conduction band. The deep traps require a large amount of energy to release the electron from the trap back to the conduction band. Normal readout procedures are

unlikely to release the electron from the trap due to the large energy gap. Sensitivity of the crystal can change as a result of deep traps being filled[38]. Initially these traps are vacant, but over time and multiple irradiations, the deep traps are filled, making these traps less competitive. The result is an increase in the number of electron recombination and an increase in sensitivity of the dosimeter. Optically annealing the dosimeter can empty some deep traps, but not all[40].

1.2.4.3 Carbon Doped Aluminum Oxide (Al_2O_3:C)

Aluminum oxide is the most widely used material in OSL dosimetry. There are a variety of ways to grow the Al_2O_3 crystal[41]. The most common variant are crystals grown in the presence of carbon, which introduces oxygen vacancies in the lattice. The high purity Al_2O_3 is initially melted at high temperatures and allowed to recrystallize where dopants are introduced causing oxygen vacancies. F-centers, or recombination centers, are created by the oxygen vacancies in the Al_2O_3:C[42]. The oxygen vacancies can be occupied by one electron creating an F^+-center making the overall lattice positively charged or two electrons creating a neutral F-center[42]. Once a hole is created, the hole is free to move in the valence band and combine with an F-center to create a F^+-center seen in Process 2 in Figure 1.4. The F and F^+ centers are the recombination centers and emit light when stimulated[42]. An optically stimulated electron is ejected out of a trap and moved to the conduction band where it can recombine with holes at a positively charged F^+-center. Process 6 depicts this event in Figure 1.4. An excited F-center is produced where it will relax back to an F-center and emits a photon, Process 7 in Figure 1.4, around 410-420nm[42] that can be observed and measured.

OSL dosimeters have become a popular passive detector due to the favorable characteristics of Al_2O_3:C, ease of use, and overall accuracy. Its linear response up to 50 Gy[33] and high sensitivity, 40-60 times greater than LiF TLD-100[43], make it an excellent material for dosimetry. One disadvantage to Al_2O_3 is the high effective atomic number of 11.28[44]. This causes the crystal to have an over response to low energy x-rays[35] in the kilovoltage range.

The readout process is much simpler and less time consuming with OSLDs as compared to TLDs. OSLDs are optically stimulated while TLDs are stimulated using heat. Stimulation times for OSLDs are on the order of seconds compared to minutes for TLDs. Due to the high sensitivity of Al_2O_3:C, only a small portion of the trapped charges are stimulated after each reading allowing the user to reread the dosimeter multiple times. OSLDs are reusable where the signal is erased by optically bleaching the Al_2O_3:C up to an accumulated dose of 20 Gy[37]. The dosimeters can be manufactured cheaply while having uniformity in sensitivity and other dosimetric properties[33]. The numerous advantages of Al_2O_3:C used in OSLDs provide the community with an excellent tool for medical dosimetry.

1.3 Hypothesis and Specific Aims

1.3.1 Hypothesis

The hypothesis for this study was: *Optically stimulated luminescent dosimeters whose visible active luminescent area have been masked can be used as a remote audit tool to measure small photon fields down to a 7.5 mm diameter field size with an accuracy of ±5% as compared to existing dosimetry measurements and Monte Carlo calculations with an uncertainty of less than 2%.*

1.3.2 Specific Aims

The specific aims for this project were:

- Determine the reproducibility of various mask sizes

  Masks of various apertures (1 mm, 2 mm, and 3 mm) were created and applied to the OSLDs. The readings of each OSLD and masks must be reproducible and fall within a certain uncertainty criteria.

- Develop and design a phantom that uses masked OSLD

  Phantom must be made of a durable material that can withstand the hardships of being mailed from institution to institution. The material shall have properties similar to that of water. The size and shape should incorporate full backscatter component of a small photon beam field. The phantom will house OSLDs at specific depths and will also include a film holder for localization purposes. As a remote audit tool, it should be easy to use by any physicist at an institution.

- Characterization of the masked OSLD system

  There are many properties of the OSLD and phantom system determined before it can be used as a viable remote audit tool. The masked OSLD will be characterized by determining correction factors such as the dose linearity, depletion between readings, signal fading over time, element correction factor, the energy correction factor, phantom scatter correction factor, and field size dependence correction factor.

- Perform a feasibility study of the small field size remote audit tool

  Small field photon beam dose measurements of the system must be accurate and the uncertainty within the system must be known. The system must be accurate and feasible when sent to institutions participating in clinical trials. The acceptance criteria of ±5% will be used for the small field photon beam audit program currently implemented by the RPC's external beam remote audit program.

2 Methods and Materials

2.1 Phantom Design

The stereotactic radiosurgery phantom was designed as a remote audit tool used to verify the dose prescribed to a specific point within the phantom using a specific field size. The RPC currently employs a single beam SRS phantom that houses TLDs as the passive detector seen in Figure 1.3. This project altered the current design by replacing the TLDs with masked OSLDs. Although the dimensions of the base and lid remained the same as the previous design, the cylindrical insert has been redesigned for OSLDs. The phantom was designed such that full backscatter conditions were met, which was accounted for in the base of the phantom.

High Impact Polystyrene was chosen as the material for the SRS phantom. Solid phantoms are advantageous over water filled phantoms in that they are much easier to use and do not have complicated loading procedures. In addition, OSLDs are not waterproof; therefore a separate compartment would have to be built inside the water phantom to house the OSLDs. High Impact Polystyrene has a density of 1.04 g/cm^3 and an effective atomic number of 5.29, which are similar to that of water[45]. The material used for the SRS phantom must be physically durable, relatively cheap to manufacture, and reproducibly machined to high accuracy. High Impact Polystyrene addressed all those needs and was a suitable material for the SRS phantom.

The cylindrical insert was designed to house two OSLD at each measurement point, 1.5 cm and 7.5 cm, and a film plate. Two OSLDs were stacked at each measurement point where the physical depths are located at the center of the two stacked OSLDs. The use of multiple OSLDs at each depth provided two independent measurements that can be averaged and compared to one another. The two inserts were carefully machined such that the masked OSLD's active area was directly centered in the insert. A film plate was added to the insert situated above the OSLDs located at a depth of 1.5 cm. This film was not meant for dose measurements but only for localization purposes. Its intended use was to verify if the institution correctly placed the phantom during irradiation. Three pin prick holes, shown in Figure 2.1, were drilled at the top of the insert where a needle can be placed inside of each hole to mark predetermined distances from the center of the phantom. The SRS phantom was designed not only to be easy to use by both the institution and the RPC, where the film and OSLDs can be easily loaded and unloaded.

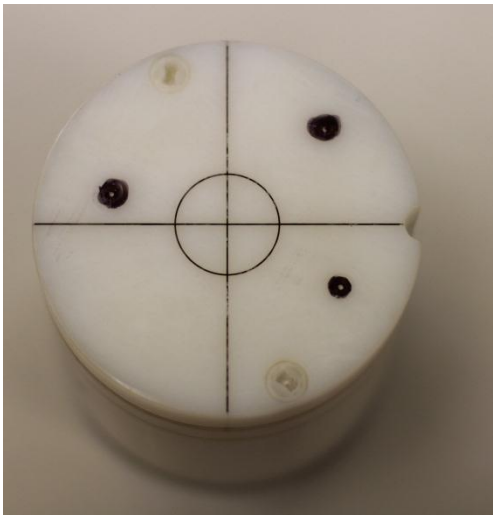

Figure 2.1: Cylindrical insert with pin prick holes used for film localization.

2.2 OSLD System

2.2.1 Landauer nanoDot

The OSLDs used in this study were the Al_2O_3:C nanoDot manufactured by Landauer Inc. (Landauer Inc., Glenwood, IL). The RPC has used the nanoDots for several years now and with great success in their remote audit program where measured uncertainty remained below 3%4. Thousands of nanoDots coming from multiple batches are currently employed in the audit program.

Each nanoDot is comprised of a retractable disk with an active Al_2O_3:C material inside a light tight plastic casing and a unique barcode for easy identification. The plastic casing measures 1 x 1 x 0.2 cm^3 seen in Figure 2.2. The casing has a density of 1.03 g/cm^3. The casing is to ensure that no signal depletion occurs due to outside light exposure. The active Al_2O_3:C material is 5 mm in diameter and 0.2 mm thick. Al_2O_3:C crystals are grown in batches where multiple batches are crushed into a powder and mixed together. The powder is also mixed with a binding agent and imprinted on thin polyester tape where disks are punched out and used in the nanoDots[46]. Mixing provides uniformity between all the dosimeters however the amount of powder in each nanoDot may vary, causing sensitivity differences between individual dosimeters in the batch.

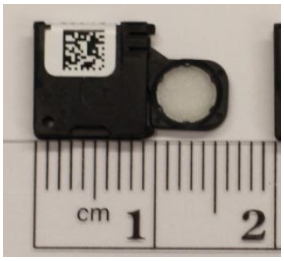

Figure 2.2: Opened nanoDot OSLD with exposed Al_2O_3:C.

2.2.1.1 Masked OSLDs

For this study, different sized masks were used to cover the active area of the OSLD. The mask aperture sizes investigated were 1 mm, 2 mm, and 3 mm in diameter shown in Figure 2.3. Figure 2.4 compared the standard OSLD with the masked OSLD. The idea behind placing masks on the Al_2O_3:C was that when the OSLDs are read, only signal from the active area defined by the mask aperture would be measured and all other light emitted by the OSLD would be absorbed by the mask.

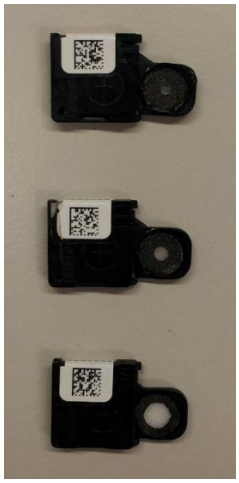

Figure 2.3: Masked OSLDs with 1mm (top), 2mm (middle), and 3mm (bottom) diameter masks.

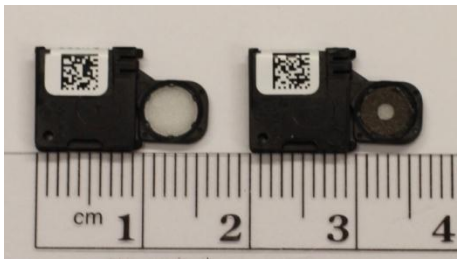

Figure 2.4: Comparing standard OSLD (left) to a 2mm masked OSLD (right)

Making masks required precision and accuracy in order to create reproducible and equivalent size masks. Black label stickers were used for the masking material. A special hole punching tool, shown in Figure 2.5, was carefully

machined such that the center hole punch was as close to the mask size desired and each mask punched out was identical to all other masks with the same aperture size. Masks were made by hammering this tool into sticker.

Figure 2.5: Hole punching tool used to create various sized masks. From left to right: 1 mm, 2 mm, and 3 mm.

The masks were carefully removed from the tool using tweezers avoiding any damage to the masks. If any tears or uneven center holes were created, these masks were discarded and a new one was made. Applying the mask onto the OSLD required careful attention not to damage the active layer with the tweezers. Overall, approximately one hundred masked OSLDs were created for this study.

2.2.1.2 Reproducibility

Once the masks had been applied to each nanoDot OSLD, a reproducibility study was needed to determine if the masked dots could provide consistent readings not only within each individual dot but also similar to dots irradiated to the same dose. Four OSLDs were used for each mask and dose point. The masked OSLDs were irradiated to 50 MU, 100 MU, 200 MU, and 300 MU using a Varian 6EX unit (Varian Medical Systems, Palo Alto, CA) at M.D. Anderson Cancer Center.

Each masked OSLD was irradiated individually in a High Impact Polystyrene phantom, placed 2 cm from the top of the phantom. An SSD of 100 cm and 10 x 10 cm^2 field size irradiation setup was used as depicted in Figure 2.6. The corrected OSLD readings were read out and compared to one another using a coefficient of variation (CoV) analysis. A CoV of less than 2% was desirable in this study.

Figure 2.6: Reproducibility setup. Each dot is placed in the removable grey insert. Irradiations are performed for each mask and at four different doses.

2.2.2 OSLD Readout

2.2.2.1 MicroStar Reader

The microStar reader developed by Landauer, shown in Figure 2.7, is used by the RPC to read nanoDot OSLDs. A single nanoDot was loaded onto the holder

and placed inside the pull out drawer. A light tight environment was produced once the drawer was closed to ensure no light leakage into the reader that may perturb the readout or damage the photomultiplier tube (PMT). Once inside the reader, the knob was turned causing the reader to push the nanoDot disc out of the cassette and in between the LED array and PMT. Figure 2.8 shows the readout schematic where light emitted from the 36 LED array stimulates light emission from the dosimeter that was collected by the PMT. This process of continuous illumination of the dosimeter while collecting the signal is known as continuous wave OSL (CW-OSL)[33]. The data obtained from the reader was recorded on a personal computer and can easily be exported for further analysis.

Figure 2.7: Landauer's microStar reader with holder. nanoDots are loaded into the holder and placed inside the black tray. The readout process commences once the knob is turned.

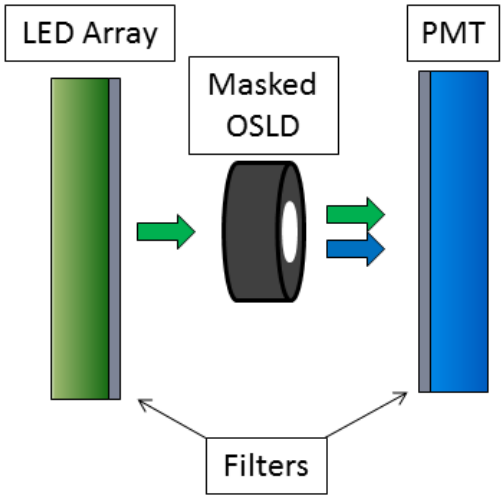

Figure 2.8: Schematic of OSL readout process.

Filters, shown in Figure 2.8, are placed to remove unwanted stimulation light coming into the PMT. The microStar reader uses two color glass band pass filters: Schott OG515 and Hoya B-370. The Schott OG515 filters the light emitted by the LED and has a LED-filter combination peak emission of 540nm[37]. The Hoya B-370 is placed in front of the PMT and the PMT-filter combination has a peak emission at 420nm[37] which is the emission of the F-centers.

2.2.2.2 Standards and Controls

Each reading session begins and ends with the reading of standards. Standards were OSLDs irradiated under a very controlled setting to approximately 100 cGy to the OSLD using a ^{60}Co unit. All standard OSLDs were placed in an acrylic miniphantom and irradiated on the Cobalt V2 unit at M.D. Anderson Cancer Center. The two standards defined the dose to count ratio for each session.

In addition to reading standard OSLDs, control OSLDs were read at the beginning, middle, and end of each session to monitor the consistency of the

reading session. Controls were irradiated to approximately 90 cGy on the Cobalt C unit at M.D. Anderson Cancer Center. The purpose of controls was to determine if the reader sensitivity has drifted throughout the OSLD reading session. If a drift occurred in the control that differed from that of the standards by more than ±1.5%, then rereading the OSLD was recommended. Irradiation of standard and control OSLDs were done separately in order to guarantee independence between these two dose references inside the OSLD reading process

2.2.2.3 Readout Procedure

The microStar required a warm up period of at least 30 minutes prior to reading any OSLDs. Before the start of each session, a series of quality control tests were performed by turning the knob to three preset positions shown in Figure 2.7. The first position was DRK, which recorded the dark current or electronic noise in the system when the LED was turned off. The second position was CAL, which recorded the number of counts when the PMT was exposed to a ^{14}C source located inside the reader. The last position was LED, which recorded the counts when the LED array was turned on for a set period of time. Each of the quality control tests were performed five times before and after the session and compared to baseline values to verify that the reader has not deviated and was working correctly.

The session started by reading one OSLD standard followed by one OSLD control, then OSLDs of interest. The unique barcode assigned to each individual OSLD was scanned then inserted into the holder where it was placed inside the drawer of the reader. Once the drawer was closed, the knob was turned from the home position (H/P) to the reading position (E1) which slides the dosimeter disk out

of the cassette and activated the LED array. The LED array was turned on for seven seconds and the counts were collected by the PMT. The software displayed and recorded the total counts collected by the PMT after seven seconds on the Landauer software. Once the LED array was turned off, the knob was turned back to the home position, which also returned the dosimeter disk back into the cassette. This process was repeated three times for each dosimeter. Once all of the OSLDs were read, the last step was to read one control and one standard followed by the quality control tests to finish the session.

2.3 OSLD Irradiations

2.3.1 Cobalt 60

Two ^{60}Co units were used in this study. Dose was determined by the amount of time the beam was on. With a half-life of 5.26 years for ^{60}Co, dose can be calculated by using the following equation:

$$\text{Dose} = \text{Output} * (0.5)^{\left(\frac{\text{d}}{365.25*5.26}\right)} * (\text{time} + \text{end effect}) \quad (2.1)$$

Output is the calibrated machine output in cGy/min. The variable “d” is the number of days from the calibration date to the irradiation date. Time is the beam on time displayed on the console in minutes. The end effect accounts for the time required for source transit.

Standards were irradiated on the Cobalt V2 unit at M.D. Anderson Cancer Center. The unit was calibrated on October 15, 2005 and produced an output of 147.9 cGy/min at a distance of 79.25 cm SSD with an end effect of 0.01 minutes. The second cobalt unit used in the study was the Cobalt C unit at M.D. Anderson

Cancer Center. Calibration occurred on October 15, 2005 with an output of 84.73 cGy/min to the jig or 77.54 cGy/min at 80 cm SSD with an end effect of 0.01 minutes. In order to determine the time needed for each unit to deliver a specific dose, time was obtained by back solving Equation 2.1.

2.3.2 6 MV Photons

All irradiations using a 6 MV beam were performed on either a Varian 6EX Clinac or Varian 21EX Clinac (Varian Medical Systems, Palo Alto, CA) linac at M. D. Anderson Cancer Center. The Varian 6EX was used to determine reproducibility and linearity while all other measurements were irradiated using the Varian 21EX linac. The linac was calibrated using TG-51 protocol prior to irradiation. Dose can be calculated by the following formula:

$$\mathrm{Dose} = \mathrm{MU} * \mathrm{PDD} * \mathrm{OF} * \mathrm{Output} \tag{2.2}$$

MU is the monitor unit setting. PDD is the percent depth dose. OF is the output factor for a specific field size. Output is the dose to muscle at d_{max} for SSD = 100 cm and a field size set to 10 x 10 cm^2 at a reference depth determined by the TG-51 protocol and given in cGy/MU.

2.4 OSLD Characterization

2.4.1 Dose Equation

OSLD dose calculations were performed by applying the following equation:

$$\mathrm{Dose} = (\mathrm{Avg\ Corrected\ Rdg}) * \mathrm{ECF} * \mathrm{S} * \mathrm{K_L} * \mathrm{K_F} * \mathrm{K_E} * \mathrm{K_{Sc}} * \mathrm{K_{FSD}} \tag{2.3}$$

where the average corrected reading is the average of the depletion corrected reading, ECF is the element correction factor unique to each individual OSLD, S is

the system sensitivity, K_L is the linearity correction factor, K_F is the fading correction factor, K_E is the energy correction factor, K_{Sc} is the phantom scatter correction factor, and K_{FSD} is the field size dependence correction factor.

The average corrected reading was obtained from three individual raw readings obtained from the reader. The first reading was not depletion corrected however the second and third readings were corrected. The coefficient of variation (COV) was calculated for the three depletion corrected readings. The RPC required that the COV be less than 2% and any OSLDs with readings that cause the COV to exceed 2% were not used.

2.4.2 Depletion Correction Factor

One of the advantages of OSLDs is their ability to be read multiple times. Reading OSLDs multiple times is advantageous because it can improve statistics, allows rereading after suspicious reading sessions, or even to be read again at a later date. With each subsequent reading, a small amount of the trapped charge is depleted and this depletion of signal must be corrected for using the following equation:

$$K_D = \frac{1}{(-5.148 * 10^{-6}) * n^2 + (-1.277 * 10^{-3}) * n + 1} \quad n = 0,1,2 \qquad (2.4)$$

Where n is the reading number starting at 0 for the first reading. Equation 2.4 is specific for a reader with a seven second reading cycle. Approximately 0.2% of the signal is reduced per reading. In order to determine the depletion correction factor relationship, an OSLD was read 10 times consecutively compared to the RPC which normally reads an OSLD 20-50 times consecutively. The counts were normalized

to the first reading and plotted versus reading number. Five dosimeters were used to determine signal depletion for this study and the results were averaged and fitted to obtain a depletion correction factor. The measured fit was compared to the RPC's depletion correction fit obtained during commissioning of the batch within 10 readings. The depletion correction factor was applied to the raw OSLD reading.

2.4.3 Element Correction Factor

The nanoDots are manufactured where the Al_2O_3:C crystals are mixed together to minimize variations within a batch. However, some inherent differences in sensitivity of each nanoDot occur within the same batch such as heterogeneity in Al_2O_3:C deposited on the dosimeter. In order to account for these differences in sensitivity, an element correction factor (ECF) was determined for each dosimeter. The ECF values used in this work were determined by irradiating 112 dosimeters to a known dose, 25 and 100cGy, in a ^{60}Co beam. The ratio of the average reading of the group to the dosimeter's raw reading defined the ECF for that specific OSLD. This process was repeated for every OSLD. The RPC required that individual sensitivities be within ±5% of the batch and those with greater ECF values were not used. When an irradiated dosimeter was read, its unique ECF for that particular dosimeter was multiplied by the reading in order to correct for deviations in sensitivity within the batch.

A separate ECF test was performed to compare the ECF values obtained with masked OSLDs to the RPC's ECF for the same OSLD. All 112 masked OSLDs were irradiated to a known dose using a ^{60}Co unit. The Co-C unit located in M.D. Anderson Cancer Center was used for irradiations. Roughly 35 OSLDs were

place on a rotating jig at a time that rotated at 10 revolutions per minute. The jig was situated 3.5 mm above a platform that was 80 cm SSD. A 25 x 25 cm^2 was used to irradiate the entire rotating jig.

2.4.4 System Sensitivity

The system sensitivity factor is used as calibration factor in the reading session. This factor is able to correlate OSLD reading and dose. Standard OSLDs were irradiated to a known dose in a ^{60}Co unit and used to define the system sensitivity. Standards were read at the beginning and end of each session with each being read three times and depletion corrected. System sensitivity is calculated by the following formula:

$$S = \frac{\text{Expected Dose to Standard}}{\text{Avg(Avg Corrected Rdg}_{\text{std}}) * K_{F,std} * K_{L,std}} \quad (2.5)$$

Expected dose to the OSLD standard is the actual dose delivered to the standards by the ^{60}Co unit. The Avg(Avg Corrected Rdg_{std}) is the average of the two depletion corrected readings at the beginning and end of each session. $K_{F,std}$ is the fading correction factor for the standards and depends on the number of days that have passed since irradiation to the date of reading. $K_{L,std}$ is the linearity correction factor.

2.4.5 Linearity Correction Factor

The nanoDot OSLD (Al_2O_3:C) readings show a supra-linear dependence with dose. With increasing dose, more deep energy traps are filled resulting in more shallow traps getting filled also. Since deep traps are rarely stimulated this changes the dose response to a specific dose. The effect is more drastic at higher doses.

However, since we are irradiating the OSLDs to 2 Gy, this dose does not modify the response by much. The linearity correction factor accounts for this effect.

Since the configuration of the OSLDs was modified by the masks, the previously determined linearity corrections were brought into question. The linearity correction factor for the masked OSLD was obtained with three independent irradiations. Each OSLD was placed one by one in a polystyrene phantom and irradiated using a 6 MV x-ray beam. Four doses were chosen to determine the dose linearity response: 50 cGy, 100 cGy, 200 cGy, and 300 cGy. For each trial of measurements, four OSLDs were irradiated at each dose. This process was repeated for each of the different mask aperture sizes: 1 mm, 2 mm, and 3 mm.

After reading each OSLD and applying its unique ECF value, an average number of counts were calculated for each dose and mask aperture. The average counts were divided by the corresponding dose to obtain a relationship between counts and dose. A dose response curve was generated by plotting the dose per count to each dose tested. Another figure was generated to determine K_L by normalizing each dose to count to that at 100 cGy for each mask size. A linear fit was applied to each mask aperture size data and compared to the commissioning data for standard unmasked OSLDs that the RPC had already determined from the following equation. The RPC K_L value is given by the following equation.

$$K_L = -0.000245071 * (\text{raw dose}) + 1.02451 \quad (2.6)$$

Raw dose is the known dose delivered by the ^{60}Co unit. The two constants were determined previously by the RPC upon commissioning the OSLD batch used in this study. Normalizing the dose response to 100 cGy provides a K_L value equal to

1 for OSLDs irradiated to 100 cGy. For this study, institutions will be asked to irradiate the masked OSLDs to 200 cGy so the K_L value will not be equal to one. Normalization at 200 cGy could be performed, however to be consistent with how the RPC commissioned the OSLD batch originally, the normalization to 100 cGy was maintained. This allows the comparison of the masked OSLD factors to the unmasked OSLD correction factors.

2.4.6 Fading Correction Factor

OSLD reading fading occurs post irradiation and is the small signal loss due to electrons in shallow traps recombining shortly after irradiation. Al_2O_3:C experiences a sharp signal drop within 15 minutes post irradiation[37]. Over the course of the 5 days following that first 15 minutes, a signal drop of 2-3% can be observed[47].

The fading correction factor for a batch was determined by irradiating OSLDs to an identical dose on different days ranging from 1 to 120 days to the read date. Once all the dosimeters have been irradiated at their respective day intervals, all the OSLDs were read together. The OSLD counts versus days post irradiation were plotted and the inverse of the relation between the two was given by the following equation as the correction factor:

$$K_F = \frac{1}{1.005 * d^{-0.0072}} \quad (2.7)$$

Where d is the number of days post irradiation. This fading correction factor was applied to every OSLD that was read in this study. In order to allow the OSLD to

reach a stable and relatively flat region of the fading curve, OSLDs were not read any earlier than 3 days post irradiation.

2.4.7 Energy Correction Factor

The energy correction factor accounts for the change in OSLD response due to the change in energy from irradiating OSLD standards in a ^{60}Co beam to the experimental measurements performed using a 6 MV X-ray beam. Standards and controls are irradiated in acrylic miniphantoms using a ^{60}Co beam. The standards are used to define the system sensitivity mentioned in Section 2.4.3. The change in energy results in a decreased sensitivity of the OSL material and is accounted for in the energy correction factor.

In order to determine the energy correction factor, six OSLDs in miniphantoms were irradiated to a known dose in ^{60}Co and another six OSLDs with a 6 MV beam. The correct time was determined for the ^{60}Co unit and the correct monitor units (MU) were determined after performing TG-51[48] in order to deliver 200 cGy to d_{max}. Irradiations performed on the 6 MV linac used an SSD of 100 cm while ^{60}Co setup required an SSD of 80 cm and both used a 10 x 10 cm^2 field size setup. Once the dosimeters were irradiated and read, Equation 2.3 was rearranged to obtain the K_E for a 6 MV beam as shown in equation 2.8:

$$K_E = \frac{\text{Dose}}{(\text{Avg Corrected Rdg}) * \text{ECF} * S * K_L * K_F * \text{BSF} * \text{ISQ}} \quad (2.8)$$

Notice that two terms were omitted from Equation 2.8, K_{Sc} and K_{FSD}, and are not needed to determine K_E. The terms will be explained in more detail in the following sections. Dose is the expected dose of approximately 200 cGy delivered to the

measurement point. S is the system sensitivity defined by the miniphantom irradiated using ^{60}Co, in which the readings have been corrected. K_L is the linearity correction factor seen in Equation 2.6 and accounts for the expected dose of 200 cGy. K_F is the fading correction factor. BSF is the back scatter factor applied to the miniphantom to calculate dose to a full phantom. ISQ is the inverse square correction since OSLDs in the miniphantoms irradiated in the 6 MV were not positioned at d_{max}. K_E values were obtained for each OSLD and the set was averaged to provide an overall system K_E.

2.4.8 Phantom Scatter Factor

Experimental irradiations are performed in a High Impact Polystyrene phantom using a 6 MV beam. As stated previously, system sensitivity is defined using a miniphantom irradiated with a ^{60}Co beam. The phantom scatter factor accounts for the change in material densities of the miniphantom to the High Impact Polystyrene phantom, 1.18 g/cm^3 to 1.04 g/cm^3 respectively. The phantom scatter factor was determined by irradiating both the miniphantom and the full phantom with a 6 MV beam. A 10 x 10 cm^2 field and 100 cm SSD setup was used. The equation for K_{Sc} is given by the following formula:

$$K_{Sc} = \frac{\text{Dose}}{(\text{Avg Corrected Rdg}) * \text{ECF} * S * K_L * K_F} \tag{2.9}$$

Dose is the actual dose delivered to the full phantom using the 6 MV beam. S is the system sensitivity defined by the 6 MV irradiated miniphantom that has been ECF, linearity, fading, inverse square, and backscatter corrected. All other terms are

same as above. A total of six K_{Sc} values were calculated and averaged to determine the system's K_{Sc} value.

2.4.9 Field Size Dependence Factor

The advent of new radiotherapy technologies and dosimetric difficulties associated with small fields led Alfonso et al. to develop a new formalism to determine absorbed dose for small fields[49]. The formalism introduces a machine specific reference field at a reference depth and compares it to a clinical field at the reference point. The equation that relates the two quantities is given by:

$$D_{w,Q_{clin}}^{f_{clin}} = D_{w,Q_{msr}}^{f_{msr}} * \Omega_{Q_{clin},Q_{msr}}^{f_{clin},f_{msr},} \tag{2.10}$$

$$\Omega_{Q_{clin},Q_{msr}}^{f_{clin},f_{msr},} = \frac{M_{Q_{clin}}^{f_{clin}}}{M_{Q_{msr}}^{f_{msr}}} * k_{Q_{clin},Q_{msr}}^{f_{clin},f_{msr},} \tag{2.11}$$

Where Ω converts absorbed dose to water for a machine specific reference field to absorbed dose to water in a clinical field. $k_{Q_{clin},Q_{msr}}^{f_{clin},f_{msr},}$ corrects the two readings for the two fields and is a factor that accounts field size differences, phantom material, geometry, and beam quality of the reference and machine specific reference field[49]. Multiple studies have determined the $k_{Q_{clin},Q_{msr}}^{f_{clin},f_{msr},}$ correction factor for several detectors and several linacs using Monte Carlo simulations[50-53]. This study renames the $k_{Q_{clin},Q_{msr}}^{f_{clin},f_{msr},}$ correction factor and replaces it with the field size dependence factor, K_{FSD}.

Multiple detectors were used to determine the true dose at various small field sizes. The Exradin A16 micro ion chamber (Standard Imaging Inc., Middleton, WI),

the Exradin D1H and D1V diode detectors (Standard Imaging Inc., Middleton, WI and personal communication), and Monte Carlo dose calculations were used to determine output factors for multiple small field sizes.

The Exradin A16 has a collecting volume of 0.007 cm^3 and an inner diameter collecting volume of 2.4 mm. Ionization charge produced by the electrons liberated inside the air cavity within the collecting volume can be measured. The detector can be related to an ion chamber that has been calibrated and is NIST traceable to determine true dose. In this work, the dosimeter was used to measure the relative signal between the 10 x 10 cm^2 reference field and the small field sizes.

The Exradin D1V and D1H diodes are P-type silicon diodes with an internal circular active area of 1 mm^2. The advantages of diodes are their high sensitivities, rapid response, and small size[11]. The depletion zone, the interface between the n and p-materials, develops an electric field. Irradiating the diode creates electron hole pairs within the depletion zone that results in a radiation-induced current[11] that can be measured by an electrometer.

The Monte Carlo dose calculations were performed using MCNPX[54,55] (versions 2.5e, Los Alamos National Laboratory, Los Alamos, NM). Both electron and photon energy depositions were tracked. A previously benchmarked model of a Varian 2100 6 MV beam was used[55]. Photon tallies were used at 1.5 and 7.5 cm depth with dimensions of 2 x 2 x 6 mm^3 and 2 x 2 x 10 mm^3 respectively. Output factors were determined by calculating and relating the photon dose at each measurement point for various field sizes.

Output factors were measured for 0.6 x 0.6, 1 x 1, 1.5 x 1.5, 2 x 2, 3 x 3, 4 x 4, 6 x 6, 10 x 10 cm^2 fields using the three Exradin detectors while Monte Carlo calculations determined the output factors for all but the 0.6 x 0.6 cm^2 field. The output factor commissioning data measured with a cc04 chamber was used to compare the three Exradin detectors and Monte Carlo calculations for certain field sizes. All irradiations were performed with a 6 MV beam at 100 cm SSD and measurements were made in the RPC water phantom at 1.5 cm and 7.5 cm depth for each field size. The detector setup for the Exradin A16 is shown in Figure 2.9 and the field size superimposed on the detector can be seen in Figure 2.10.

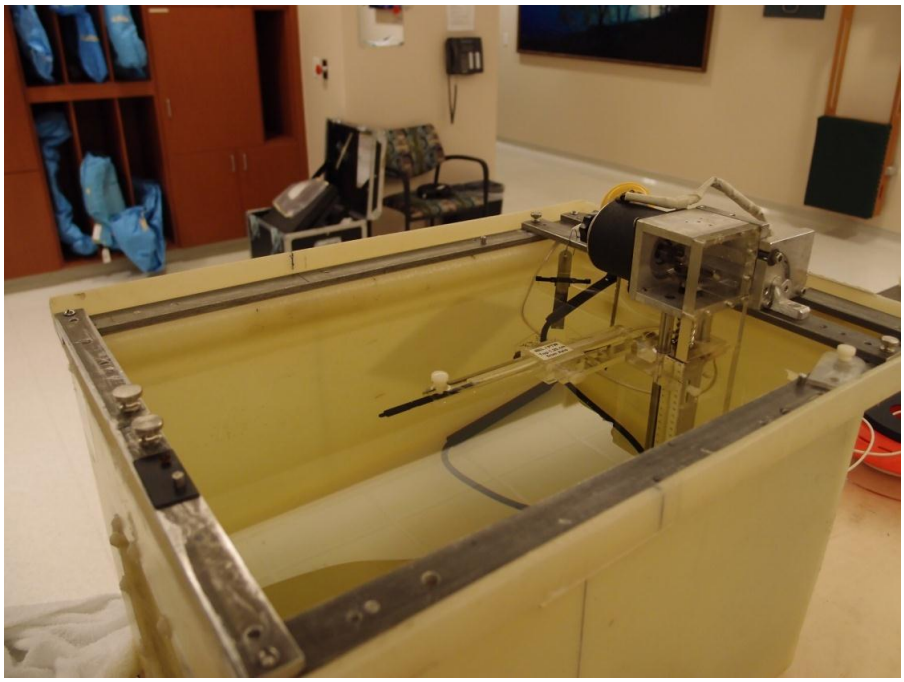

Figure 2.9: Detector setup to determine output factor. An Exradin A16 in the RPC water phantom at 1.5 cm depth.

Figure 2.10: Exradin A16 with two field sizes superimposed. Left – 0.6 x 0.6 cm^2. Right – 1 x 1 cm^2.

The Exradin D1V and D1H diodes used the same setup however the orientation of the two diodes were different. The D1V was placed vertically while the D1H was positioned horizontally as shown in Figure 2.11.

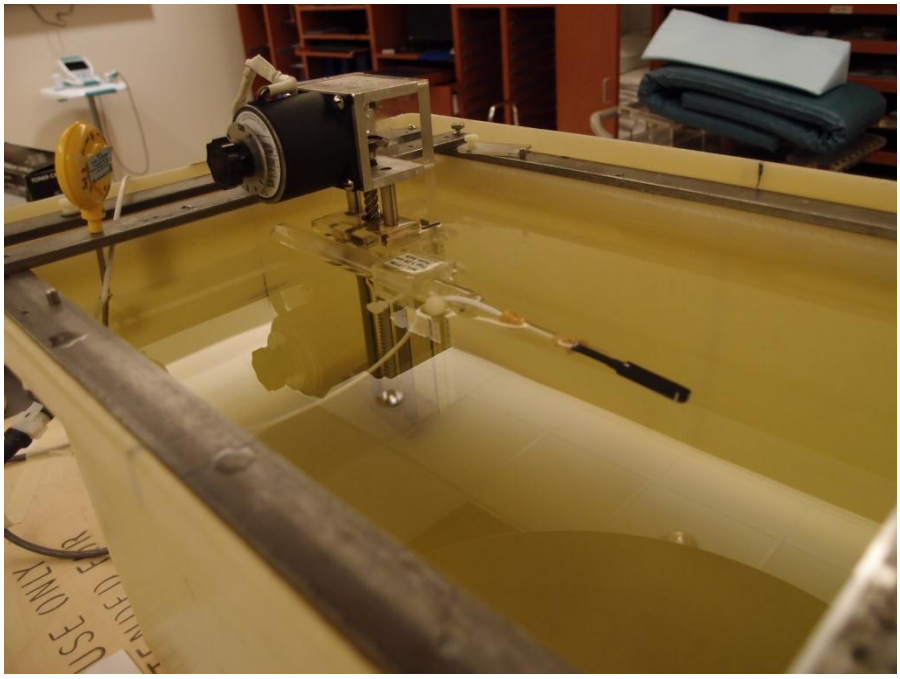

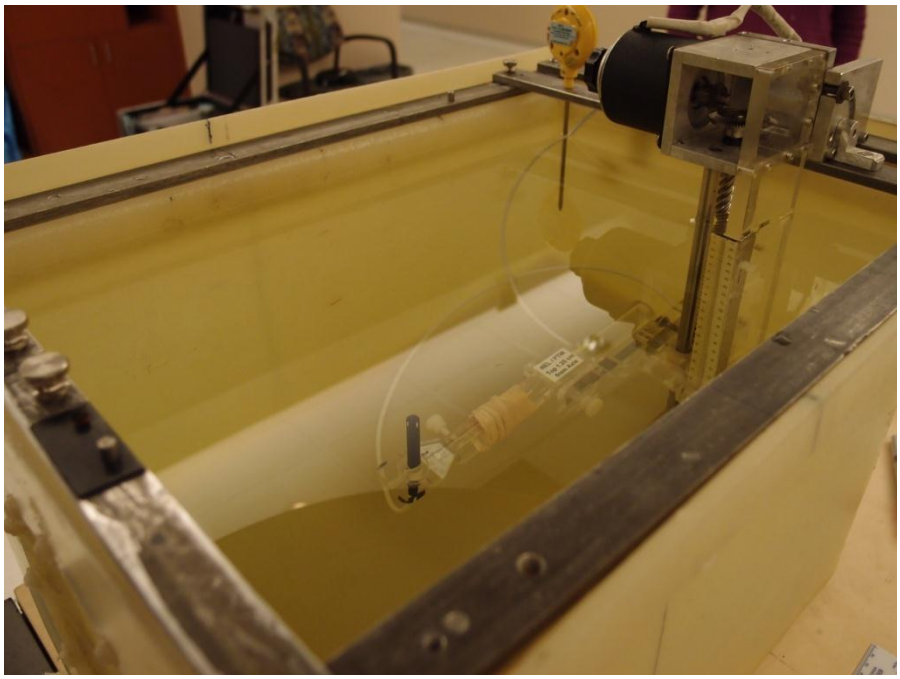

Figure 2.11: Exradin D1H (top) and Exradin D1V (bottom) setup.

The field size dependence correction factor was determined by solving for K_{FSD} in Equation 2.3 knowing all of the other correction factors. K_{FSD} is given by the following formula:

$$K_{FSD} = \frac{\text{Dose}}{(\text{Avg Corrected Rdg}) * ECF * S * K_L * K_F * K_E * K_{Sc}} \quad (2.12)$$

K_{FSD} is the ratio of the measured output factor to that measured by the phantom with masked OSLDs. The measured output factor in the numerator is determined by using various dosimeters. The measured output factor of the phantom can be determined by delivering a known dose to the OSLD and applying correction factors to the OSLD reading to obtain the correct measured output of the phantom seen in the denominator. The MUs required to deliver a dose of 200 cGy for each field size was calculated by rearranging Equation 2.2 and solving for MUs where the PDD is equal to one at d_{max} = 1.5cm. The output was determined by performing a TG-51 calibration to obtain a cGy/MU relation for a reference 10 x 10 cm^2 field size. The

output factors were measured using the Exradin A16, Exradin D1V, Exradin D1H, and Monte Carlo. Francescon et al. determined correction factors, $k^{f_{clin},f_{msr},}_{Q_{clin},Q_{msr}}$, for the Exradin A16[50] and Exradin diodes (personal communication) measuring various small field sizes which were used to correct the measured output factors. The four output factors were averaged and used to determine the correct number of MUs to deliver for each field size to obtain a dose of 200 cGy. Six OSLDs were used to determine K_{FSD} for each of the small field sizes and the average determined the system's K_{FSD} correction factor for each field size.

2.5 Film Measurements

Radiochromic film is a widely used dosimetric tool in radiation therapy. The film changes color after irradiation and does not require any post processing procedures. The resultant image depicts the ratio of radiation impinged on the film to radiation transmission through it, optical density (OD), which can be measured. Advantages of radiochromic film include high spatial resolution, low spectral sensitivity, no angular dependence, and tissue equivalence (Z = 6.84)[56].

Gafchromic EBT film (ISP, Wayne, NJ) and Gafchromic EBT2 film (ISP, Wayne, NJ) were used in this study. When these two films were irradiated, the radiosensitive layer undergoes a partial polymerization causing a color change that darkens with increased dose[56]. The films were designed to measure doses on the range from 1 cGy to 8 Gy for EBT and 1 cGy to 40 Gy for EBT2. Typical doses performed in this study range from 2-5 Gy. The RPC uses EBT2 extensively, which has been characterized for each batch. However, the EBT film used in this study has not been characterized yet. EBT films were cut into 4 x 5 cm^2 pieces and were

placed at d_{max} under a 6MV beam in a solid water phantom with adequate backscatter material and irradiated to different doses ranging from 25 cGy to 7 Gy with a setup of 100 cm SSD using a 35 x 35 cm^2 field size. Films were read and an optical density (OD) versus dose calibration curve was generated shown in Figure 2.12.

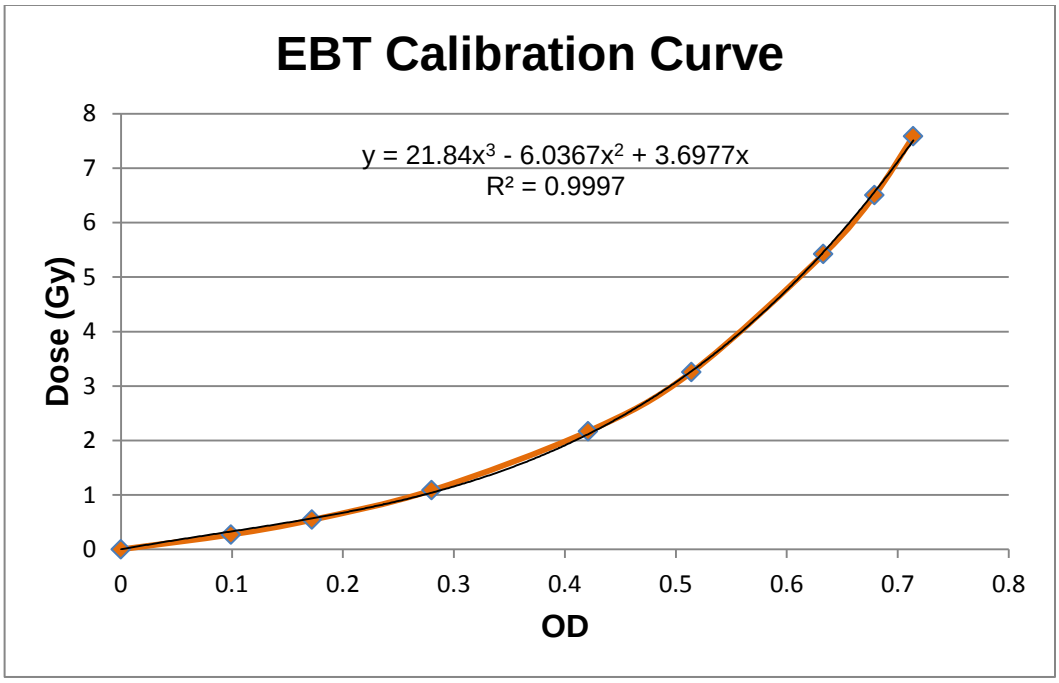

Figure 2.12: EBT calibration curve

In this study, EBT films were used to measure profiles of multiple small field sizes, which were compared with the diameter of the masked OSLD active area. These comparisons provided an idea as to which field sizes the masked OSLD could measure correctly without any signal loss due to volume averaging across the dosimeter. The profiles also provided an indication of the under response of the masked OSLD caused by any small shift in the phantom during irradiation. The field sizes investigated included: 0.6 x 0.6, 1 x 1, 1.5 x 1.5, 2 x 2, and 3 x 3 cm^2. Films were irradiated to 500 MUs in a water phantom at two depths 1.5 cm and 7.5

cm. The center of the film was marked using the crosshairs from the linac. Figure 2.13 shows a setup of a film irradiation.

Films placed in the remote audit phantom were used only for localization purposes. The center of the film was determined by using pin pricks with a known coordinate system in the phantom. After irradiation, the films were placed in a black envelope in order to reduce light exposure and were read at least five days post irradiation.

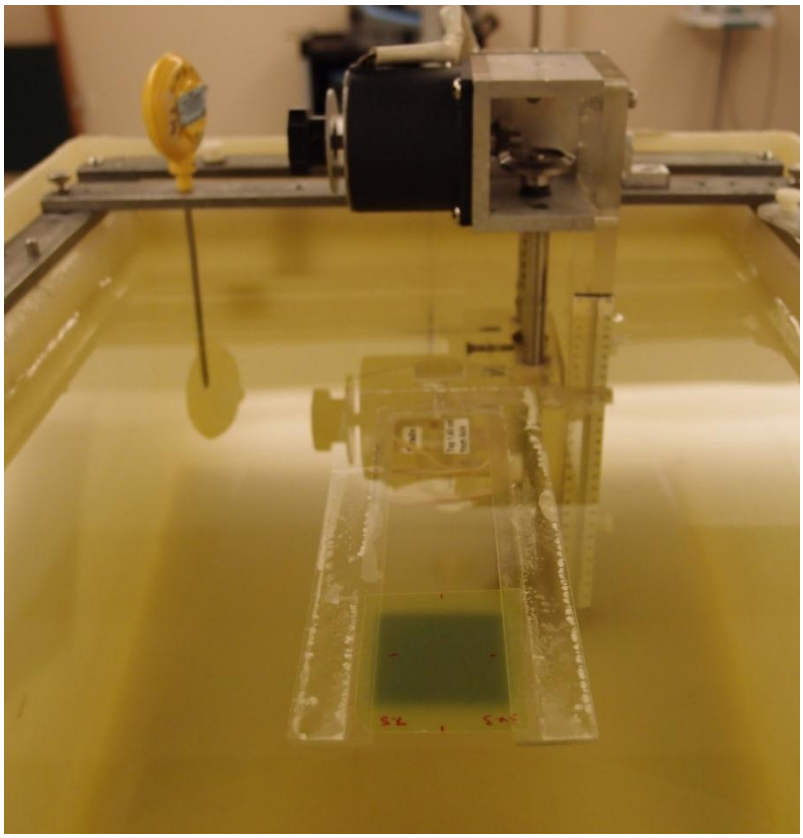

Figure 2.13: Film irradiation in the RPC water phantom using a customized film holder. EBT2 film placed at 1.5 cm depth irradiated with 500 MU using a 3 x 3 cm^2 field. Crosshairs were used to mark the film.

The CCD Microdensitometer Model CCD100 (Photoelectron Corporation, Lexington, MA) was used to evaluate the OD for both EBT and EBT2 film. A light tight box housed an LED light tray and a CCD camera. The light tray emits light at a

wavelength around 600-700 nm, which matches closely to the optical absorption spectrum of the film. The CCD camera mounted above the light tray detected light transmitted through the film. The camera was placed 44 cm above the light tray and focused on an area approximately 150 mm by 150 mm. The resolution of the CCD camera was 512 x 512 pixels with a pixel size of 0.3 mm. Calibrating the system required imaging a blank film and setting the image as the "flat field" which was subtracted from measured films. Variations within the system were accounted for by the flat field. Spatial calibration was determined by using a grid with 10 mm spacing. Images were saved and exported for further analysis.

2.6 Optical Annealing

One advantage of using OSLDs is that they are reusable. Previous work has shown that OSLDs are stable with a dose accumulation up to 20 Gy[37]. For accumulated doses above 20 Gy, OSLD sensitivity changes are observed[37]. The RPC uses a 10 Gy accumulated dose limit for each OSLD which was also applied in this study. The OSL signal can be removed by either annealing or optically annealing (bleaching) the dosimeter. Annealing requires high temperatures close to 900˚C to remove most if not all of the filled traps[57,58]. This is unreasonable since the plastic casing was not designed for such high temperatures. Optically annealing, or bleaching, depends on the wavelength and intensity of the light, which can determine the amount of time needed to anneal. The RPC uses a custom built cabinet to anneal the OSLDs shown in Figure 2.14. Two 54 watt fluorescent bulbs are at the top and bottom of the cabinet. The lamps are equipped with a UV filter that filters out UV photons with wavelengths less than 395 nm that can cause

further ionizations during the annealing process. Each OSLD that was used in this project was annealed for at least 24 hours to ensure adequate liberation of all energy traps.

Figure 2.14: Optical annealing box at the RPC.

2.7 Remote Audit Trials

Once the masked OSLDs were characterized, the next step was to determine the feasibility of the system by sending the phantom to multiple institutions as a remote audit tool. Physicists were asked if they were willing to participate in the audit free of charge to test their cones or MLC system. Institutions were provided with instructions on the phantom setup, the phantom loaded with OSLDs and film, instructions on how to reload the phantom with new OSLDs and film, and irradiation forms.

Once the phantom returned to the RPC, the OSLDs and films were read out. The two OSLDs in the phantom were averaged and the predetermined correction factors were applied generating the RPC measured dose. The ratio of the RPC measured to the institution's reported dose was calculated to determine agreement.

Film was used to verify correct positioning of the radiation beam/phantom and was used to account for any discrepancies in the dose comparison. In addition to irradiating the SRS phantom, institutions were asked to perform the normal RPC output check using the miniphantoms as a precaution if any large deviations were seen in the measurements.

2.7.1 Instructions

Slight modifications were made to the already existing RPC instructions for single beam SRS phantom irradiations. The instructions are shown in Appendix 6.3.1. The instructions provided the physicists with a step by step process on phantom setup and phantom loading. Due to uncertainties in small fields, accurate phantom positioning was emphasized in the instructions. Only one prototype was created for this study, but all of the audits required multiple irradiations hence the need for loading instructions. Physicists were asked to deliver 200 cGy to the 1.5 cm depth measurement point for a 6 MV beam.

2.7.2 Irradiation Forms

Irradiation forms were used to document the work performed by the physicist. The irradiation forms used in the audits are shown in Appendix 6.3.2. The form asked for information pertaining to demographics, treatment unit, manufacturer of the cones or MLCs, and output of the beam. Monitor unit settings, output factors, and PDD were documented for each cone or MLC designation.

3 Results

3.1 Phantom Design

The phantom prototype was made of High Impact Polystyrene (HIPS) and had dimensions of approximately 15 x 15 x 16 cm^3. The full phantom prototype shown in Figure 3.1 includes a lid, base, and cylindrical cone. HIPS was chosen because it is easy to machine, robust, durable, and relatively inexpensive to manufacture. HIPS is also roughly water equivalent with a density of 1.04 g/cm^3 and can approximate the dosimetric properties of water. Due to large size of the phantom, full scatter conditions are met when irradiations were performed. In addition, the RPC has a vast amount of experience using HIPS in other phantoms also used as remote audit tools such as anthropomorphic phantoms.

Figure 3.1: Full phantom prototype. The phantom is comprised of a lid, base, and cylindrical cone and houses four OSLDs at two depths and a film insert.

The cylindrical insert is located at the center of the full phantom in Figure 3.1 and houses two types of dosimeters: film and OSLDs. Shown in Figure 3.2, the insert is comprised of multiple sections all connected by two large plastic screws. Two measurement points were chosen, one at 1.5 cm depth and the other at 7.5 cm depth. Two OSLDs were placed at each depth for measurement purposes. A film plate was added above the 1.5 cm measurement point and can hold a 55 mm diameter piece of film. The film was not meant to be used for dosimetry but to verify user setup position accuracy. The top section of the insert has three small holes indicated by the large black dots seen in Figure 3.2. These holes help guide a sharp needle used to create pin pricks on the film. The pin pricks help determine the relation of the image on the film to the center of the phantom.

Figure 3.2: Cylindrical insert. The insert is separated into multiple compartments: a film plate and two OSLDs at 1.5 cm and 7.5 cm depth each.

The physical dimensions of the insert are shown in a cross sectional view in Figure 3.3. Going from top to bottom, the second two millimeters thick section is the film plate where a small 55 mm diameter grove was machined such that a piece of film can firmly be placed on. The next section holds the two OSLDs. A 1cm x 1 cm wide square with a depth of 4 mm was carefully drilled into the section. Since the active area of the nanoDot is not directly at the center of the cassette, a 1mm shift in both x and y direction was accounted for in the design of the cylindrical insert. The cylindrical insert was designed such that the 1.5 cm depth and 7.5 cm depth are located in between the two OSLDs. The average dose of the two OSLDs will represent the dose to the measurement depth. Additional schematics of the phantom design can be seen in the Appendix 6.1 where Figures 6.1 details the lid and base dimensions, Figure 6.2 depicts the top view of the insert, and Figure 6.3 shows the location of the pin pricks relative to the center of the phantom.

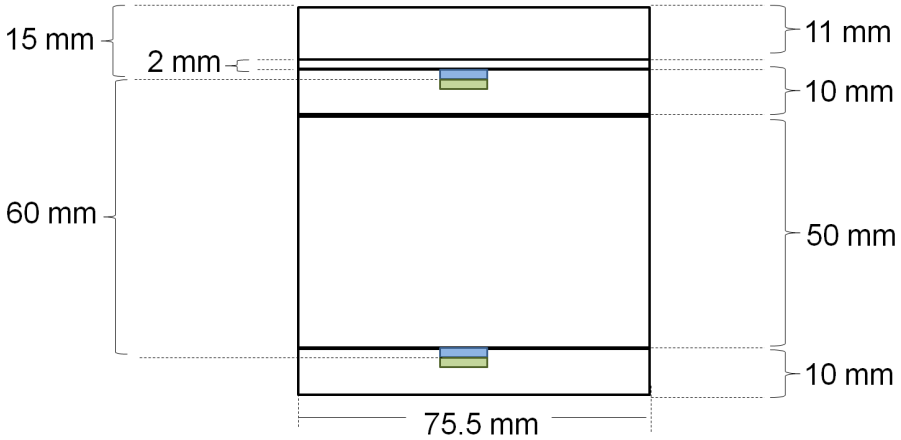

Figure 3.3: Sagittal view of insert. Multiple sections of the insert are seen where the 2 mm insert holds film and each of the 10 mm sections holding 2 OSLDs represented by the blue and green rectangles.

3.2 Reproducibility

Irradiations were performed on each of the three aperture size masked OSLDs at four different doses. The depletion and ECF corrected readings were compared to one another at their respective dose and mask size. Coefficient of variation analysis was used to determine the reproducibility of the masks at different doses. Table 3.1 illustrates the reproducibility study.

Table 3.1: Coefficient of variation analysis of the three different aperture sizes. Each aperture was irradiated using four different doses.

Aperture	MU	CoV
1 mm	50	4.96%
1 mm	100	7.04%
1 mm	200	5.18%
1 mm	300	7.62%
2 mm	50	1.21%
2 mm	100	1.16%
2 mm	200	0.82%
2 mm	300	1.91%
3 mm	50	1.62%
3 mm	100	0.78%
3 mm	200	1.07%
3 mm	300	1.65%

As depicted in Table 3.1, the 2 mm and 3 mm had a desirable CoV of less than 2% at each dose. However, the 1 mm masked OSLDs had CoVs ranging from 4.96%-7.62%. The high CoV can be due to nonuniformity in the LED light distribution of the OSLD reader. The OSLD reader uses a mechanical system to open each nanoDot; therefore positional accuracies play an even larger role in the number of counts recorded. Due to the high CoV of the 1 mm masked OSLDs, it was decided that they would not be used for the remainder of the study. Both the 2

mm and 3 mm apertures provided CoVs of less than 2% making either one a suitable candidate for the study. Since the RPC already uses a 3 mm diameter TLD packet for SRS measurements, the 2 mm aperture was selected to be the best size and was used for the remainder of the study to measure smaller field sizes than the current TLD program.

3.3 Element Correction Factor

Due to the inherent heterogeneity of the Al_2O_3:C distribution on the OSL nanoDot, an element correction factor (ECF) was needed to correct each nanoDot relative to the average of the batch. Originally, the RPC defined ECF was used for the masked OSLD.

The first test was to irradiate the OSLDs to 25 cGy each which is the standard procedure performed by the RPC during commissioning of a new batch. A histogram of all of the ECF values is depicted in Figure 3.4.

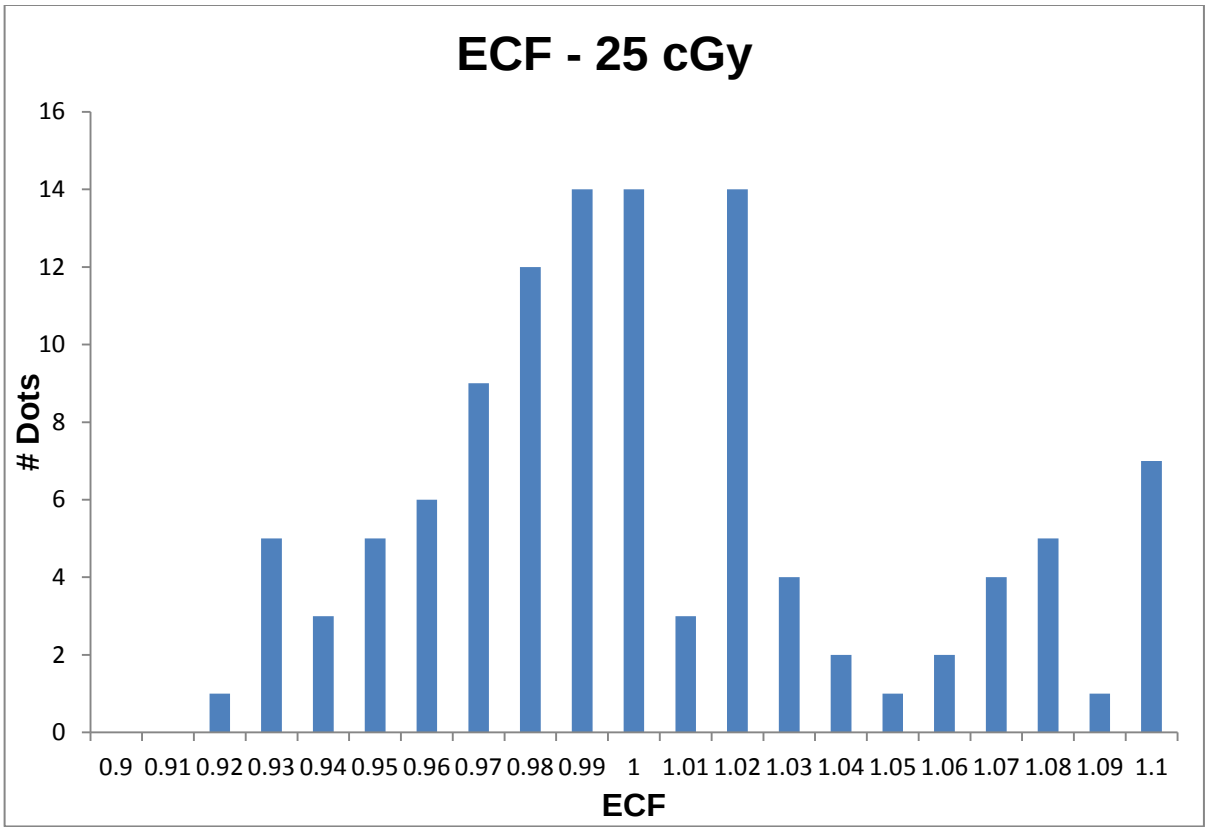

Figure 3.4: Histogram of OSLD ECF values irradiated with 25 cGy. Each OSLD was compared to the average of the batch to define an ECF for the individual OSLD.

After analyzing the data in Figure 3.4 above, it was believed that 25 cGy was too low of a dose for ECF determination since the number of counts for each OSLD dosimeter was reduced greatly because of the masks. The signal produced from a 25 cGy irradiation had large coefficient of variation many above 2%. This helps explain the large differences and spread in ECF values determined from the 25 cGy irradiation. A repeat study was performed irradiating all the OSLDs to 100 cGy instead of the normal 25 cGy. The results are shown in Figure 3.5.

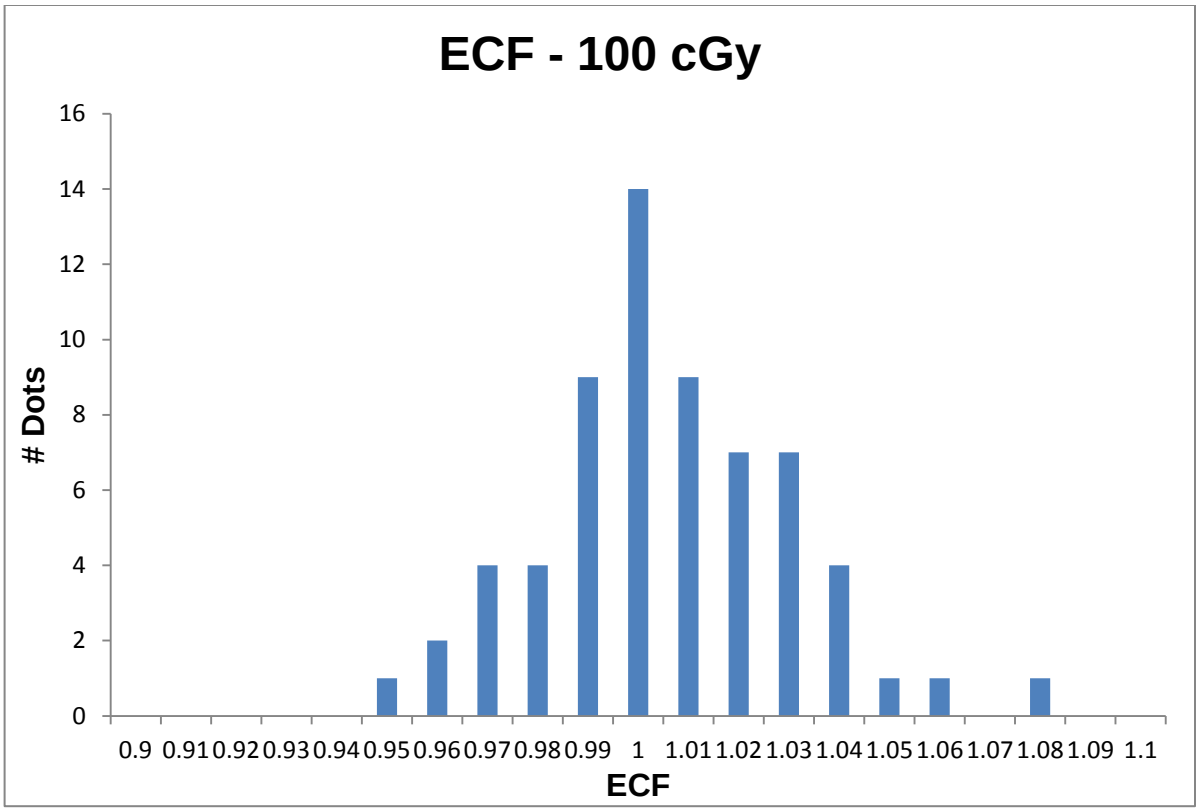

Figure 3.5: Histogram of OSLD ECF values irradiated with 100 cGy. Each OSLD was compared to the average of the batch to define an ECF for the individual OSLD.

The histogram in Figure 3.5 shows a Gaussian distribution, which is expected for this type of measurements. Overall the coefficients of variations for OSLDs irradiated to 100 cGy were much better than the 25 cGy with the majority being less than 2%. Table 3.2 compares 10 out of 64 randomly sampled OSLDs irradiated to both 25 and 100 cGy with the RPC values.

Table 3.2: Measured ECF value comparison. Randomly selected ECFs irradiated to 25 and 100 cGy are compared to one another and to the RPC ECF values.

OSLD	RPC	25 cGy	100 cGy	Diff (25 and 100)	Diff (RPC and 100)
1	1.014	1.006	0.999	0.70%	-1.48%
2	1.063	1.019	1.022	-0.30%	-3.86%
3	0.99	1.021	1.010	1.08%	2.02%
4	1.032	0.998	0.992	0.60%	-3.88%
5	0.989	0.987	0.969	1.82%	-2.02%
6	0.965	0.958	0.943	1.57%	-2.28%
7	1.005	0.969	0.969	0.00%	-3.58%
8	1.001	0.982	0.976	-0.61%	-2.50%
9	1.066	1.034	1.036	0.19%	-2.81%
10	1.012	0.966	0.985	1.97%	-2.67%

There was a difference from -0.61% to 1.97% from irradiating the masked OSLDs with 25 cGy and 100 cGy and difference of -3.88% to 2.02% between the RPC ECF to the 100 cGy ECF. Therefore, the ECF for the small field size audit masked OSLD system had to be determined by irradiating each OSLD to 100 cGy and determining new ECFs for the masked OSLD.

3.4 System Sensitivity

System sensitivity was typically derived from irradiating standards to 100 cGy. These standards defined the dose to count ratio for the session. For this study, masked OSLDs were used as standards as opposed to the normal unmasked OLSDs typically used by the RPC. Standards were irradiated before determining the energy correction factor and the field size dependence factor. In addition, masked standards were used for each session of the remote audit trials. Table 3.3 lists some system sensitivity values determined in this study.

Table 3.3: System sensitivity values. Three independent standards were irradiated to 100 cGy. The system sensitivity converted the OSLD counts to dose.

OSLD	Dose (cGy) per Count	CoV (%)
1	0.00089978	0.26
2	0.00090223	
3	0.00089760	

The three standards agreed well with one another and were highly reproducible with a coefficient of variation of 0.26%.

3.5 Linearity Correction Factor

Three separate irradiation trials were performed to determine the masked OSLD linearity correction factor. A total of 48 OSLDs, 4 for each dose per trial, were irradiated. An example of an un-normalized dose response of an individual trial is show in Figure 3.6.

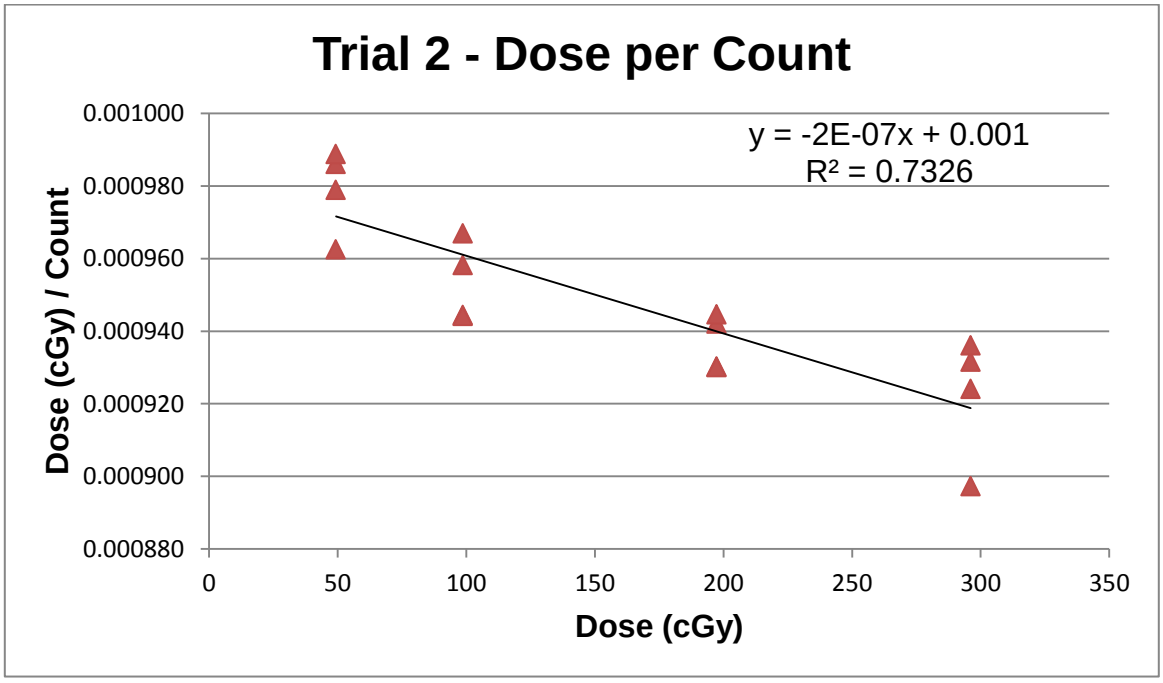

Figure 3.6: Dose response versus dose for Trial 2.

All individual dose response values were normalized to the average dose response value at 100 cGy. The results of all three separate trials are shown in Figure 3.7.

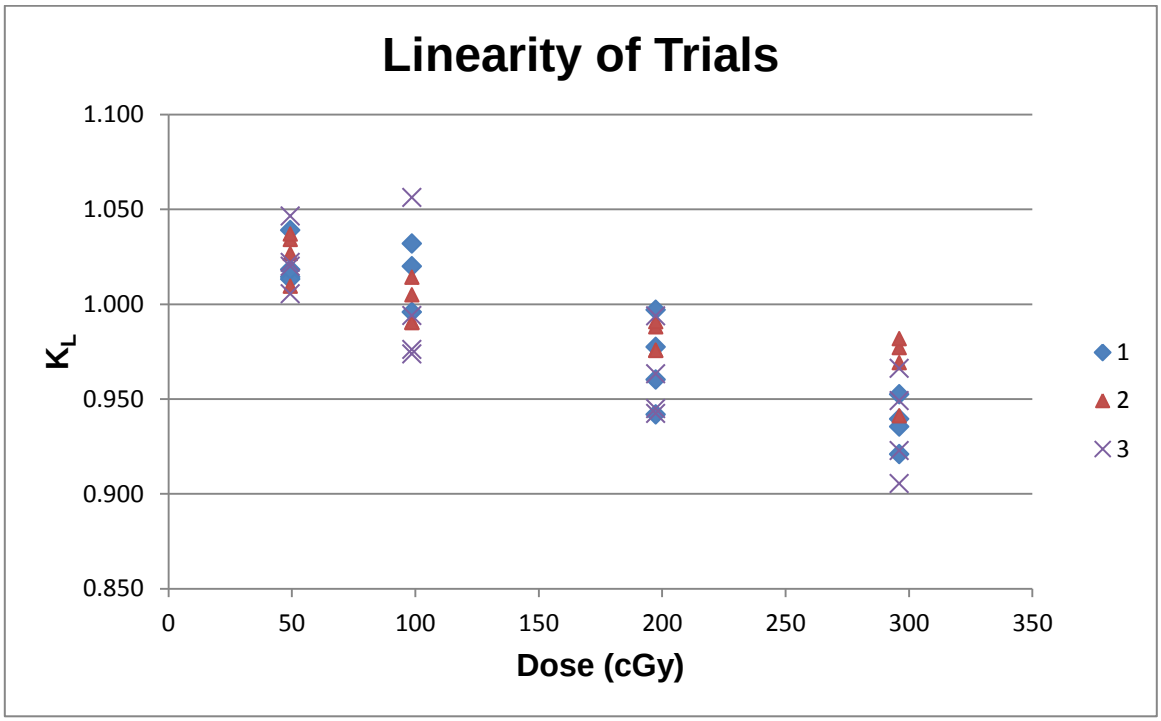

Figure 3.7: Normalized dose response relative to the average dose response at 100 cGy.

An average K_L value was calculated at each dose point for the three separate trials seen in Figure 3.7. These averages were normalized to 100 cGy making $K_L = 1.0$ at that dose. Figure 3.8 shows the linearity curves for the three separate trials normalized to 100 cGy.

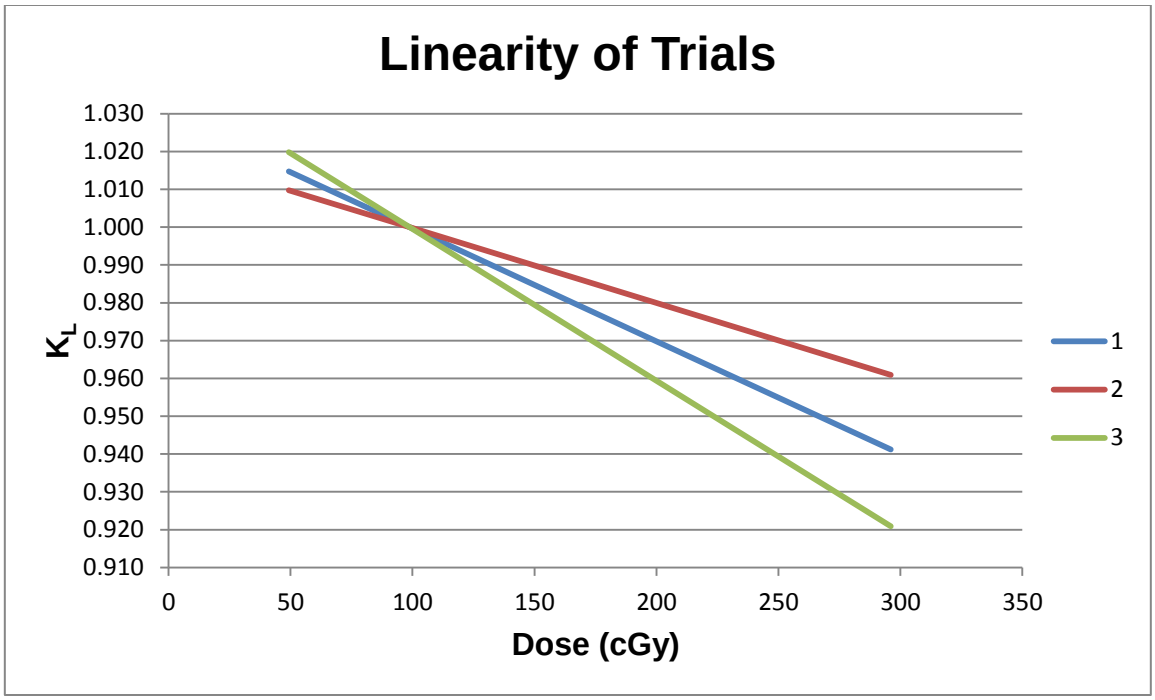

Figure 3.8: Linearity for each separate trial.

The K_L lines of trials 2 and 3 agreed to 1% at 50 cGy and 2% at 200 cGy with trial 1 falling between trials 2 and 3. As dose is increased, a larger disagreement is seen specifically at 300 cGy where the differences between the K_L lines of trials 2 and 3 are 4%.

The linearity correction factors of the three trials were combined to form one single K_L linear fit. The formula for linear fit is K_L = (a x dose) +b where a = -0.0003 and b = 1.0295 determined from the averages of the three trials.

$$K_L = -0.0003 * (\text{raw dose}) + 1.0295 \quad (3.1)$$

The four dose points were inserted into the formula where the fit was normalized to 1.0 at 100 cGy. The final K_L linearity correction factor was the normalized fit shown in Figure 3.9 with the 68% and 95% confidence intervals, which represent one and two standard deviations, respectively.

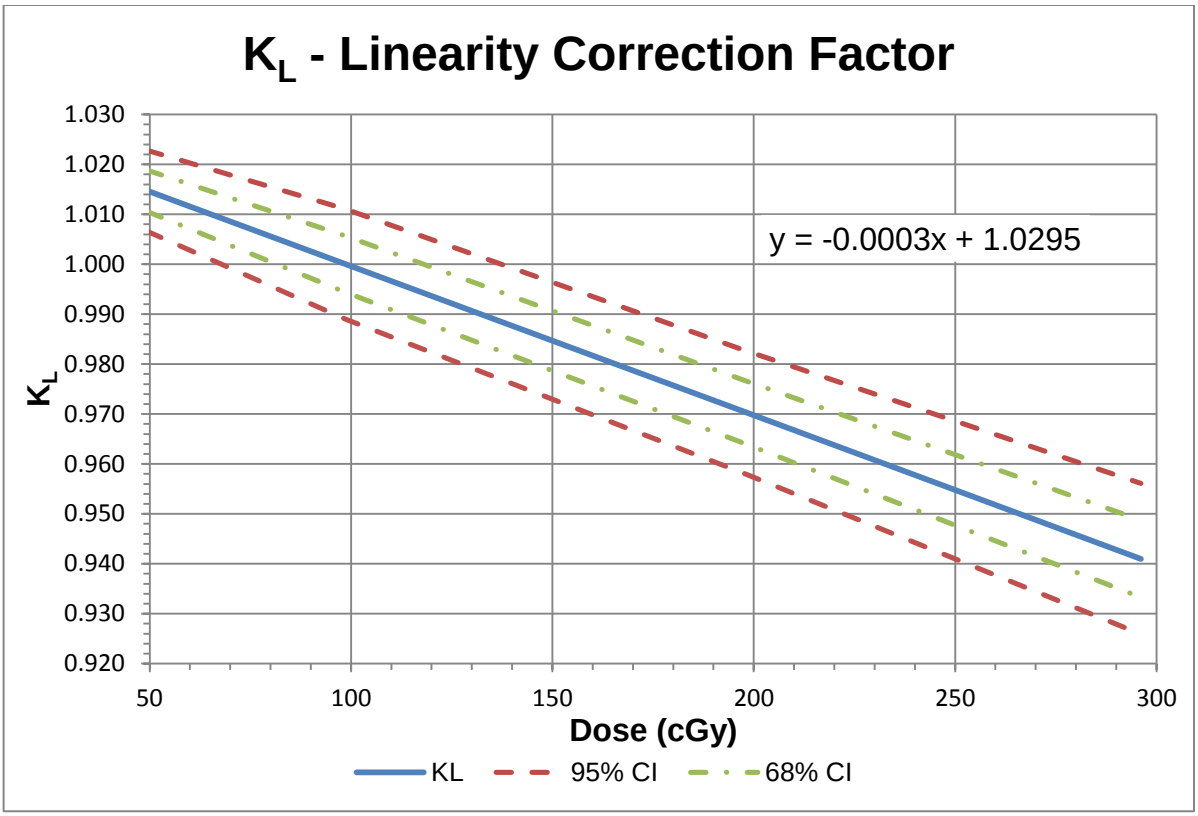

Figure 3.9: Normalized linearity correction factor based on the independent trials. The green and red dashed lines represent the 68% (1σ) and 95% (2σ) confidence intervals respectively.

Figure 3.9 shows the 68% confidence interval of the K_L linear fit for doses between 190 to 210 cGy to be approximately 1.1% or ±0.55%. The remote audit program asks institutions to deliver 200 cGy to 1.5 cm depth measurement point, therefore σ = ±0.55% can be expected as the uncertainty for the linearity correction factor and was used in the final uncertainty calculation.

3.6 Depletion Correction Factor

Five randomly sampled OSLDs were read to determine the depletion correction factor for this study. Each masked nanoDot was read ten times where the subsequent readings were normalized to the initial reading. The average results along with standard deviations (1σ) are plotted in Figure 3.10.

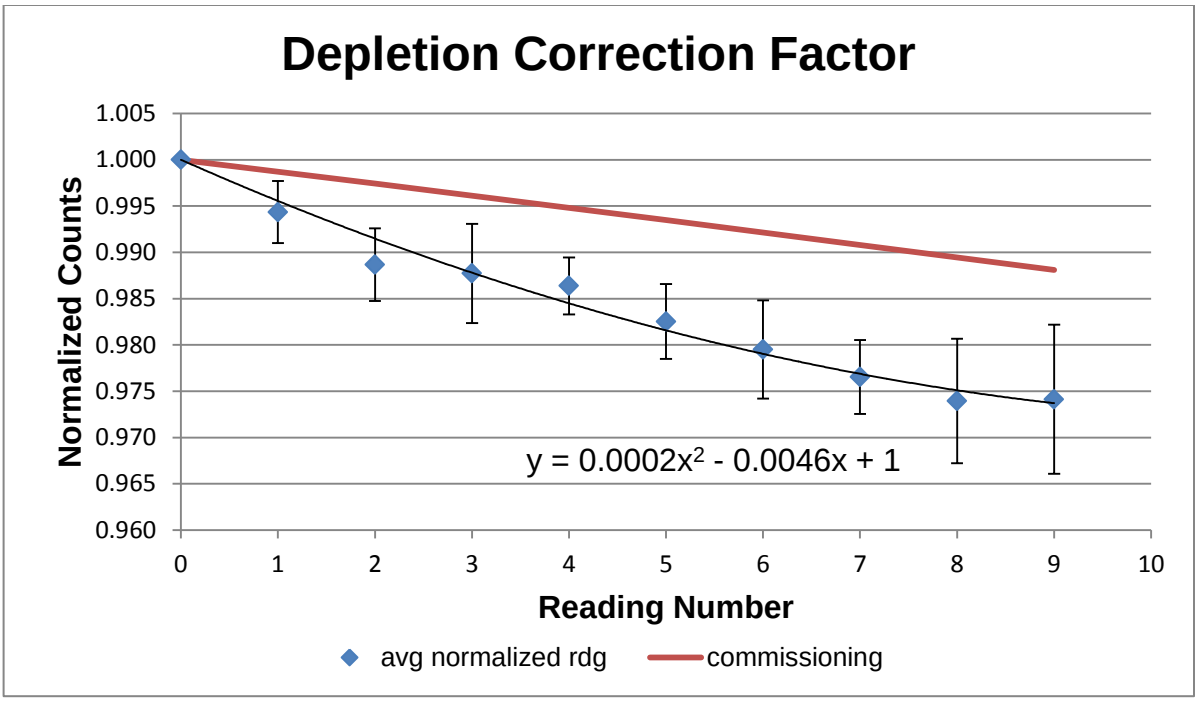

Figure 3.10: Measured masked OSLD versus RPC unmasked commissioning depletion correction factor. Five nanoDots were read and normalized to obtain a quadratic fit.

A quadratic fit was obtained from the data set and used to compare the measured masked OSLD equation with the RPC's unmasked OSLD commissioning depletion correction equation in Equation 2.4. The two fits agreed initially, but as more readings were performed, an apparent disagreement was seen. The RPC uses one depletion correction factor for all of their readers, however each reader still undergoes a depletion test to verify using this technique. If the new quadratic fit was within 1% of RPC's depletion correction quadratic fit than the old equation can be used. The equation in Figure 3.10 compared with Equation 2.4 agreed to within 1% within the first five readings. In a typical session, each OSLD was read three times therefore using Equation 2.4 for the study was justified.

3.7 Energy Correction Factor

The system sensitivity from masked OSLDs irradiated in a miniphantom using a ^{60}Co source was used for the masked OSLDs irradiated with a 6 MV beam. Equation 2.8 was used to determine the energy correction factor and the results of four separate trials are shown in Table 3.4.

Table 3.4: Energy correction factors of four trials.

Trial	K_E
1	1.014
2	1.017
3	1.016
4	1.006

The average of the four separate trials was 1.013 with a standard deviation (1σ) of 0.005. This value was compared with the RPC's K_E commissioning data for unmasked OSLDS of 1.011. The measured and commissioned data were similar and within a standard deviation therefore the RPC commissioned value for unmasked OSLDs of K_E = 1.011 will be used for the masked OSLD system.

3.8 Phantom Scatter Factor

The system sensitivity defined by irradiating a miniphantom using a 6 MV beam was used for the irradiations performed on the full phantom using the same 6 MV beam. Six trials were performed using Equation 2.9 to calculate K_{Sc} for the system. The results of the trials are shown in Table 3.5.

Table 3.5: Phantom scatter factor of six separate trials.

Trial	K_{Sc}
1	1.004
2	1.027
3	1.001
4	1.027
5	1.018
6	0.998

The six trail results ranged from 0.998 to 1.027 with an average of 1.013 with a standard deviation (1σ) of 0.013. The phantom scatter factor was a new factor introduced into OSLD dose equation and $K_{Sc} = 1.015$ was used for the remainder of the study.

3.9 Field Size Dependence Factor

The output factors used to determine the field size dependence factors were measured using the Exradin A16 micro ion chamber, Exradin D1V and D1H diodes, and Monte Carlo simulations. The A16[50] and D1V (personal communication) output factors were corrected using the average k_Q for a Siemens and Elekta machine published by Francescon et al. Figures 3.11 and 3.12 show the output factors of the various devices measured at 1.5 and 7.5 cm depth for multiple field sizes, respectively. The CC04 data presented on each figure were from the M.D. Anderson commissioning data for the accelerator used to determine K_{FSD}.

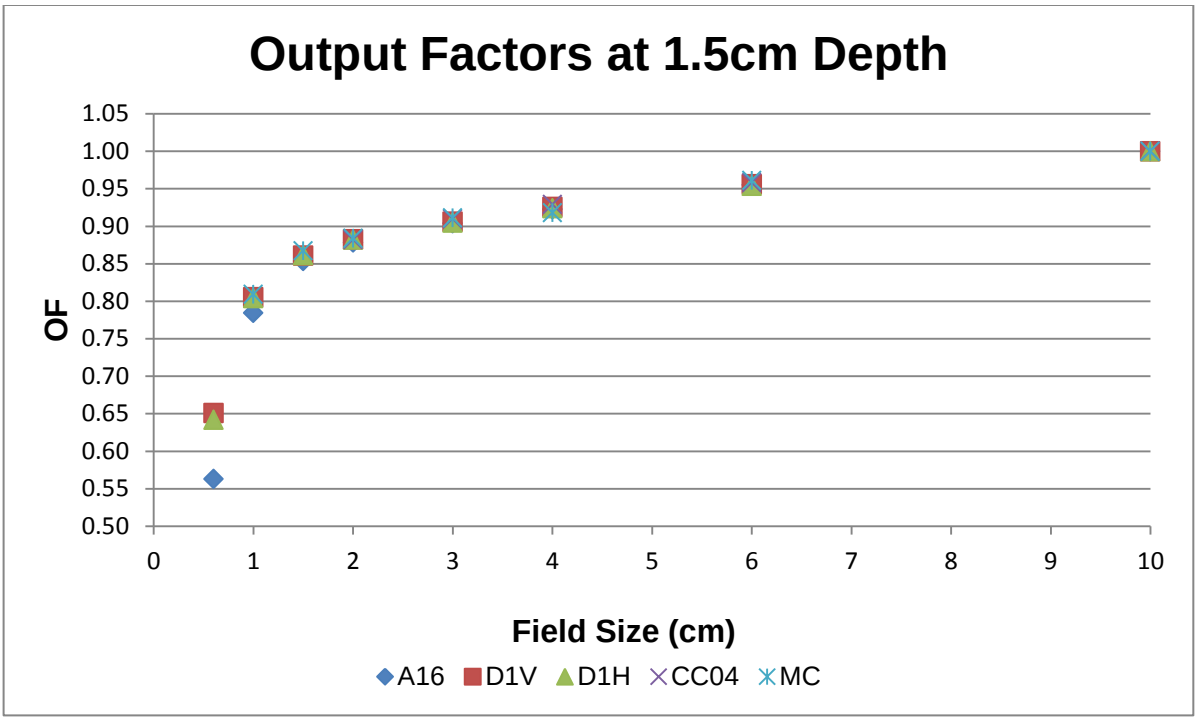

Figure 3.11: Output factors of the Exradin A16 micro ion chamber, Exradin D1V and D1H diodes, and Monte Carlo simulations measured at 1.5 cm depth. The square field sizes measured ranged from 0.6 cm to 10 cm.

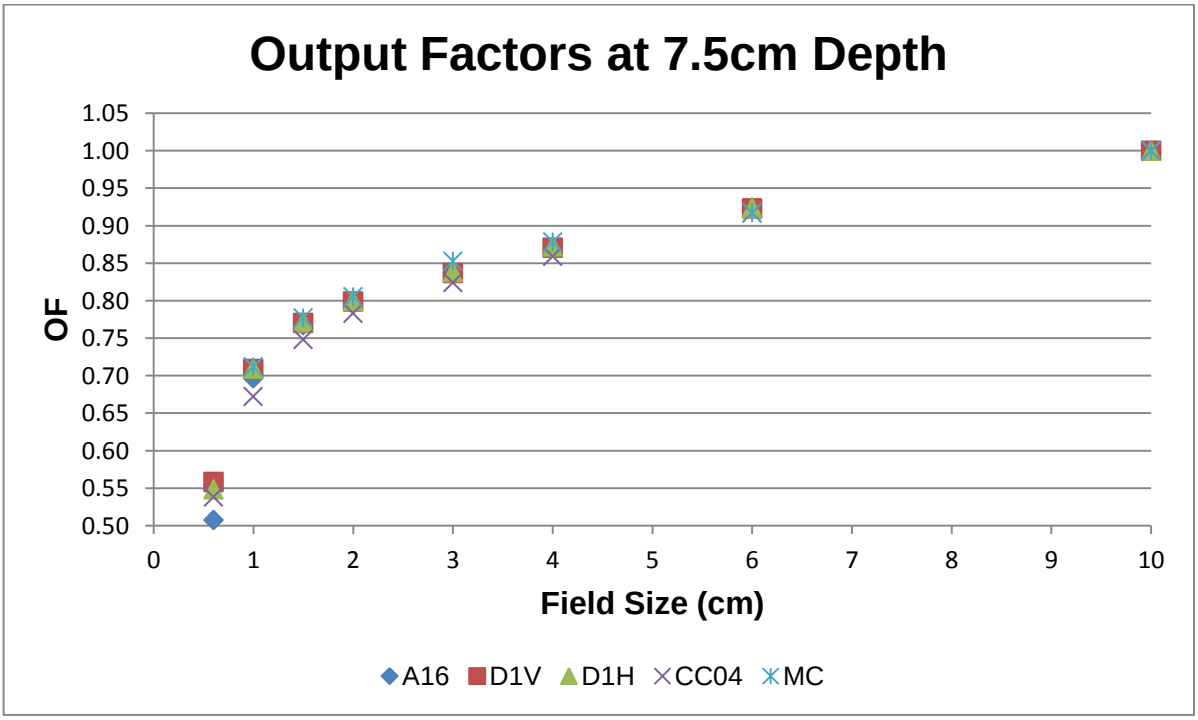

Figure 3.12: Output factors of the Exradin A16 micro ion chamber, Exradin D1V and D1H diodes, and Monte Carlo simulations measured at 7.5 cm depth. The square field sizes measured ranged from 0.6 cm to 10 cm.

The output factors from Figures 3.11 and 3.12 matched up well within each set for large field sizes however at small field sizes (≤ 1.5 cm) less agreement is seen. Large differences were seen at 0.6 x 0.6 cm^2 for the A16 due to volume averaging effects and possible positioning error. In Figure 3.12, a 3% correction was applied to the Monte Carlo calculations and the results were normalized to the 6 x 6 cm^2 field. This modification was justified due to the confidence in the ion chamber measurements at this field size and less confidence in the Monte Carlo calculations.

The field size dependence factor was determined by using Equation 2.12 where the output factors from Figures 3.11 and 3.12 were used to calculate dose. Six nanoDot OSLDs were used for each field size and the average K_{FSD} with one standard deviation were plotted in Figure 3.13. Table 3.6 shows an example of one data set from Figure 3.13.

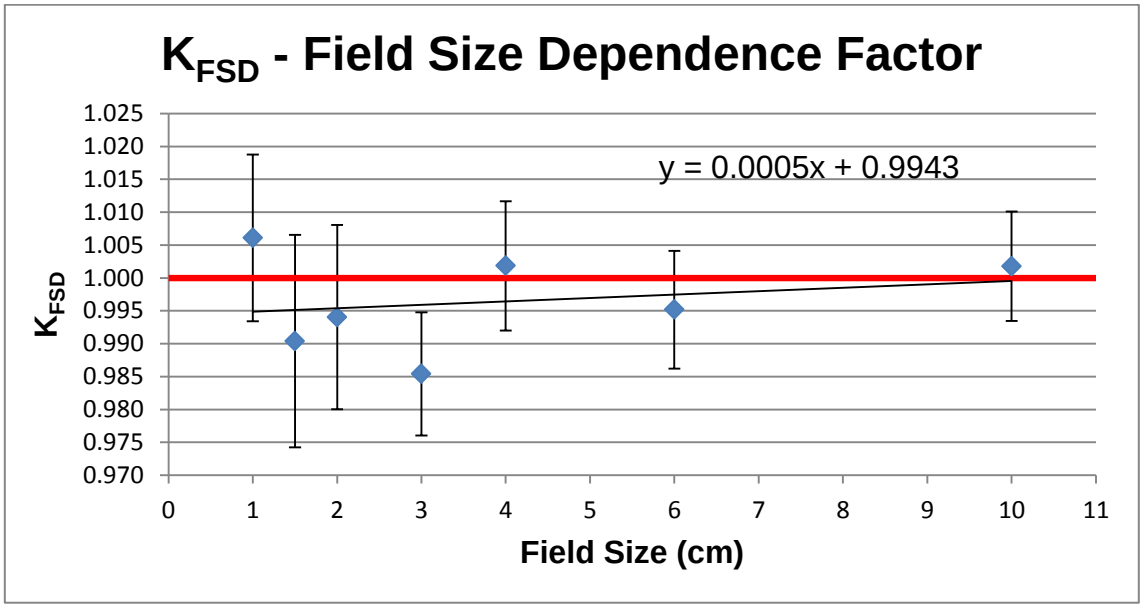

Figure 3.13: Field size dependence factor for various field sizes. The average results plotted with standard deviations. A linear fit was applied to the results. The red line represents unity.

Table 3.6: Field size dependence factor for a 1 x 1 cm^2 field.

1x1 cm^2	
n	6
Mean	1.006
Min-Max	0.994-1.024
Standard Deviation	0.013

The average K_{FSD} ranged from 0.985 to 1.006. A linear fit was applied to the data and compared to unity. A linear regression statistical analysis showed that there was no statistically significant difference between the slope of the linear fit and unity ($p = 0.443$). The same test proved that the intercept was statistically significantly different than 0 ($p < 0.05$). The statistical analysis confirmed that $K_{FSD} = 1$ for the masked OSLD system. To determine the uncertainty of K_{FSD}, the 68% and 95% confidence intervals were plotted with a KFSD = 1 for each field size in Figure 3.14.

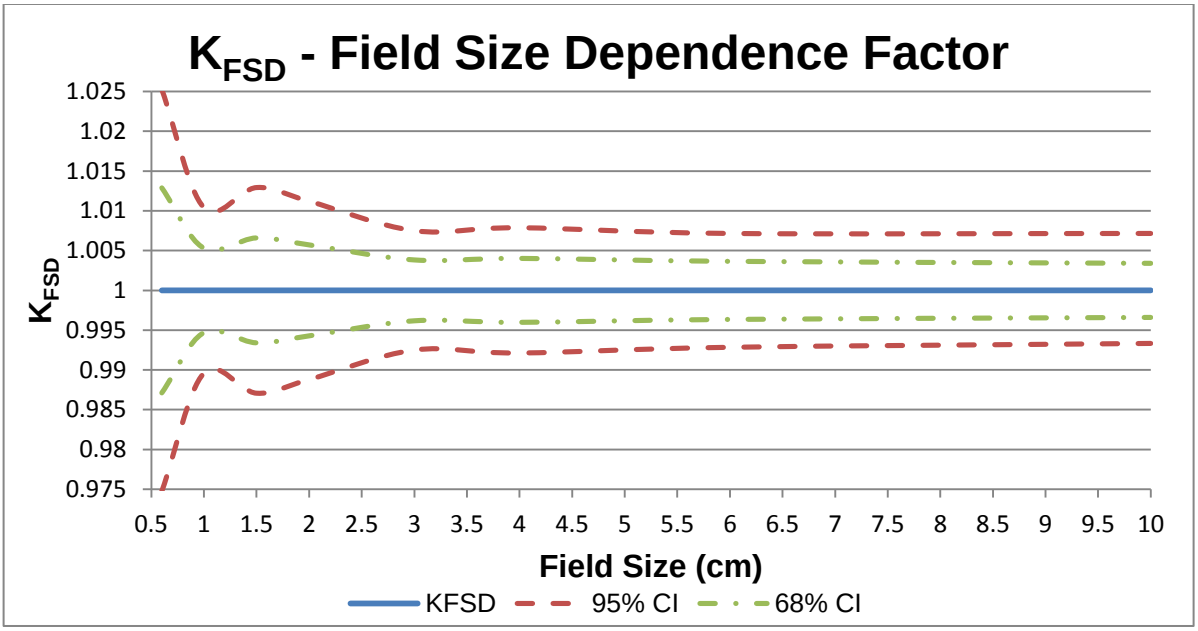

Figure 3.14: Field size dependence factor, $K_{FSD}=1$, for multiple field sizes. The green and red dashed lines represent the 68% (1σ) and 95% (2σ) confidence intervals respectively.

Figure 3.14 shows the 68% confidence interval of the KFSD for a 1 x 1 cm^2 field size to be 1% or ±0.5%. The remote audit program asks institutions to use either a 1 x 1 cm^2 or 10 mm field size, therefore σ = ±0.5% can be the expected uncertainty for the field size dependence factor at these field sizes.

3.10 Film Profiles

Once the masked OSLDs were characterized, a study was performed to determine the field size limitation for the system. Film profiles were measured at 0.6 x 0.6, 0.7 x 0.7, 1 x 1, 1.5 x 1.5, 2 x 2, and 3 x 3 cm^2 field sizes at both 1.5 cm and 7.5 cm depth. Figure 3.15 - 3.17 shows the results for 0.6 x 0.6, 0.7 x 0.7, and 1 x 1 cm^2 field sizes at 1.5 cm depth. The remaining field sizes and depths are shown in Appendix 6.2, Figures 6.4 - 6.11. Within each figure there are three sets of lines. The black lines represent the 2 mm masked OSLD coverage on the profile. The red lines correspond to a 1 mm shift of the masked OSLD. The green lines cover the full active area of an unmasked OSLD.

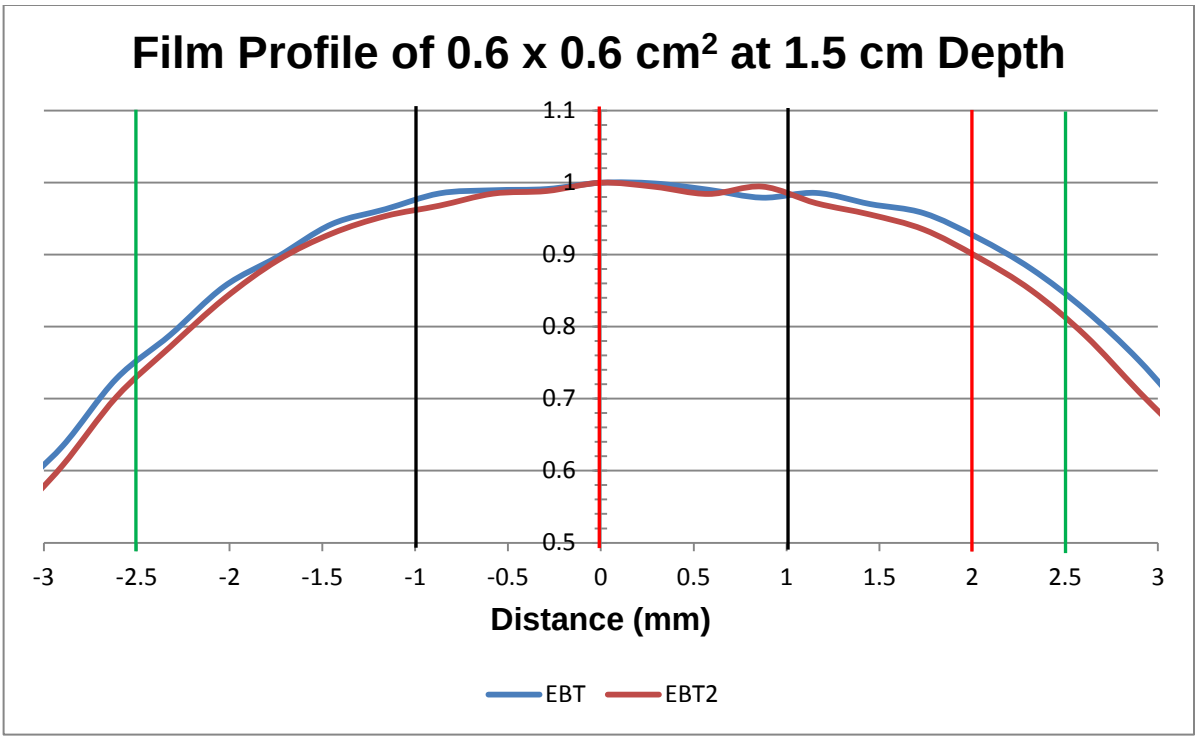

Figure 3.15: Film profiles of EBT and EBT2 for a 0.6 x 0.6 cm^2 field size.

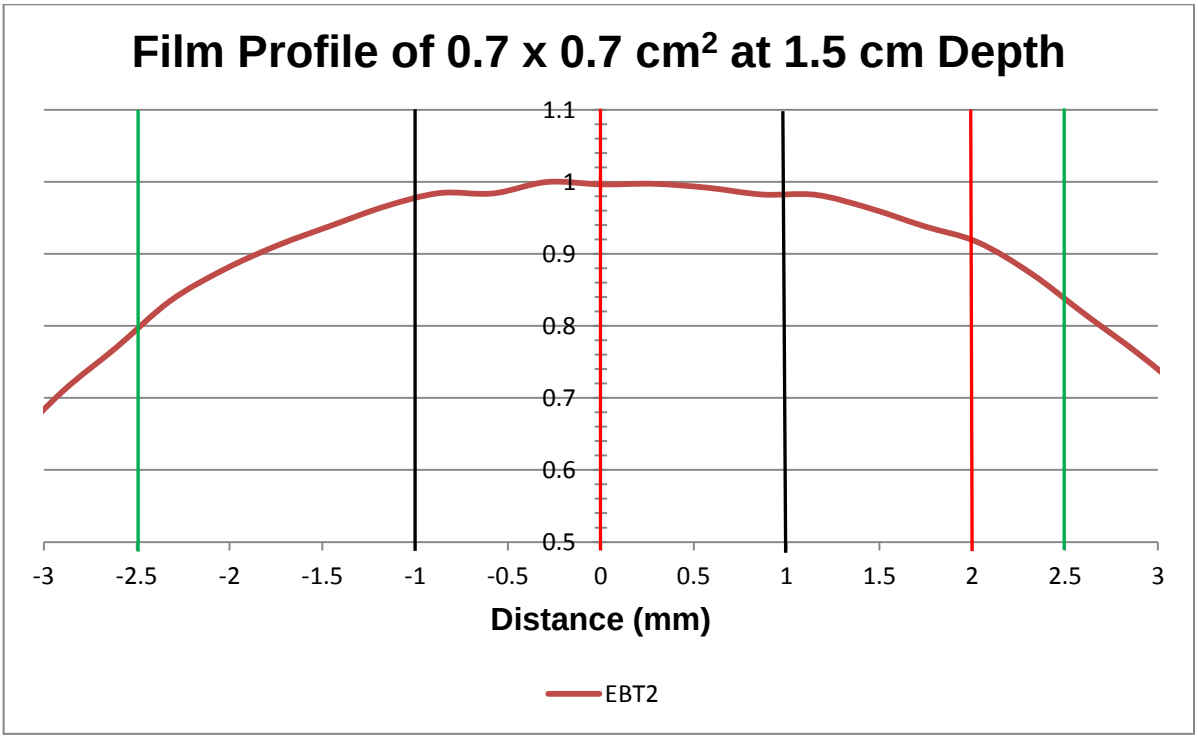

Figure 3.16: Film profile of EBT2 for a 0.7 x 0.7 cm^2 field size.

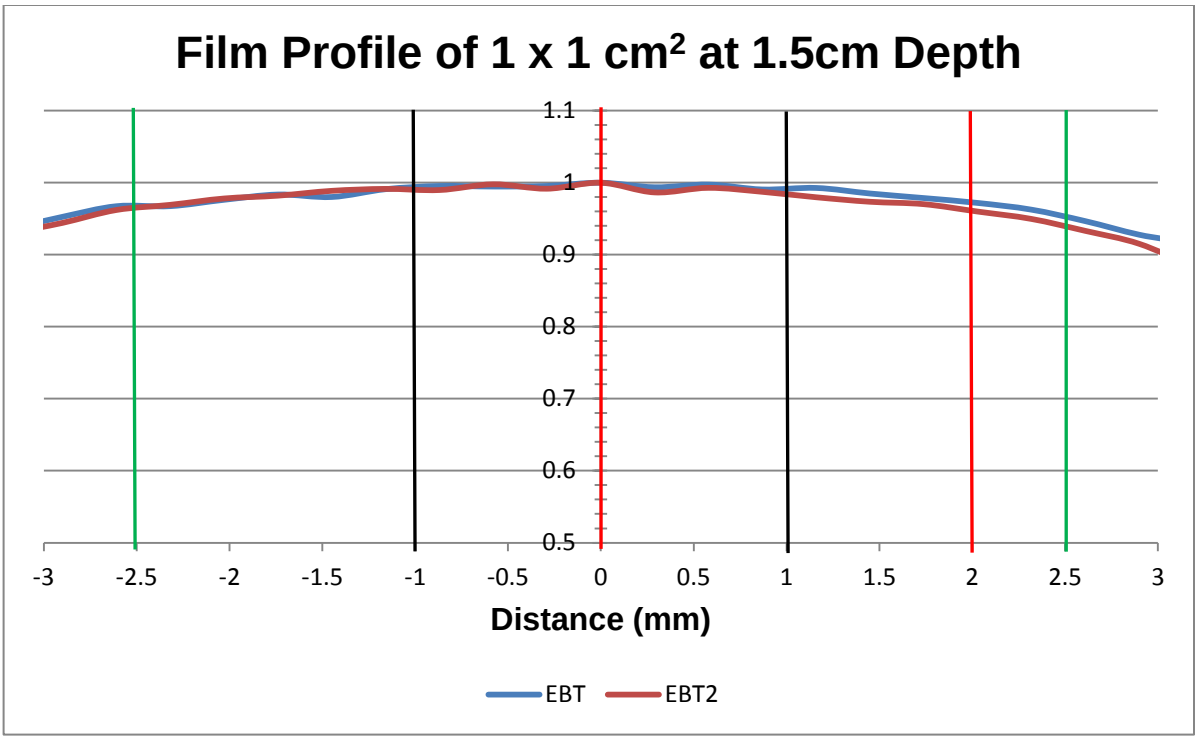

Figure 3.17: Film profiles of EBT and EBT2 for a 1 x 1 cm^2 field size.

For circular collimators, the equivalent square equation is given by the following equation.

$$a = r * \sqrt{\pi} \tag{3.2}$$

Where a is one side of a square field and r is the radius of the circular collimator. An example of circular field sizes compared with their equivalent square field sizes is shown in Table 3.7.

Table 3.7: Circular collimator sizes converted to equivalent square field sizes.

Cone Size (mm)	Radius (mm)	Equivalent Square (mm)
7.5	**3.75**	**6.65**
10	**5**	**8.86**
12.5	**6.25**	**11.08**

The profiles from Figures 3.15 - 3.17 with the 2 mm masked OSLD overlay resulted in defining a minimum field size of 1 x 1 cm^2 for MLC defined SRS systems and 10 mm diameter fields for CyberKnife and cone systems. A 1 mm shift for 0.6 x

0.6 cm^2 can cause roughly a 5% signal reduction due to volume averaging. Therefore the 0.6 x 0.6 cm^2 and 0.7 x 0.7 cm^2 field sizes were eliminated for this study.

3.11 Remote Audit Trials

Multiple remote audits were performed in this study using CyberKnife, linac-based cones, and MLCs to define small fields at six different institutions. Each institution was asked to deliver a dose to a measurement point as calculated by the treatment planning system. The results of the audit are shown in Table 3.8 - 3.10 for various treatment units and field sizes.

Table 3.8: Result of two audits using a CyberKnife unit and various field sizes.

Trial	Cone Size (mm)	Institution Reported Dose (cGy)	RPC Calculated Dose (cGy)	RPC/Institution
1	7.5	199.5	184.6	0.925
2	7.5	200.0	185.8	0.929
1	10	199.6	192.3	0.964
2	10	200.0	191.2	0.956
1	12.5	200.1	194.0	0.970
2	12.5	200.0	192.6	0.963

Table 3.9: Result of three audits using a linac based cones for various field sizes and machines. The Elekta Synergy machines used Elekta circular collimator stereotactic cones while the Varian TrueBeam used BrainLab cones.

Trial	Machine	Cone Size (mm)	Institution Reported Dose (cGy)	RPC Calculated Dose (cGy)	RPC/Institution
4	Truebeam BL	7.5	200.0	201.8	1.009
6	TrueBeam BL	7.5	200.0	185.5	0.927
3	Elekta Synergy	10	200.0	199.3	0.996
4	TrueBeam BL	10	200.0	197.7	0.988
6	TrueBeam BL	10	200.0	188.8	0.950
4	TrueBeam BL	12.5	199.0	200.9	1.004
6	TrueBeam BL	12.5	200.0	197.0	0.985
3	Elekta Synergy	15	200.0	197.0	0.985
3	Elekta Synergy	20	200.0	200.5	1.003

Table 3.10: Result of two audit using MLCs for various field sizes.

Trial	Machine	Field Size (cm^2)	Institution Reported Dose (cGy)	RPC Calculated Dose (cGy)	RPC/Institution
5	Varian Novalis	1x1	200.0	205.5	1.027
6	TrueBeam	1x1	200.0	197.0	0.985
5	Varian Novalis	2x2	200.0	211.0	1.055
6	TrueBeam	2x2	200.0	208.8	1.044

The CyberKnife results from Table 3.8 under responded for all the field sizes with the measured to reported dose ratio improving with increasing field size. The average RPC measured to institution reported dose ratio was 0.951±0.0176 for the CyberKnife system. The linac-based cone trials overall performed well with an average ratio of 0.983±0.026. The MLC trials had an average ratio of 1.006±0.021 between the measured and reported dose for a 1 x 1 cm^2 field and a ratio of 1.050±0.006 for a 2 x 2 cm^2 field.

The dose profiles of the 7.5 mm and 10 mm cones used on the CyberKnife unit is shown in Figures 3.18 and 3.19. Both profiles show a fairly centered setup with little volume averaging over the masked OSLD. The profiles for the other institutions are shown in Appendix 6.4, Figures 6.12-6.21. The majority of the profiles showed a correct phantom setup by the institution.

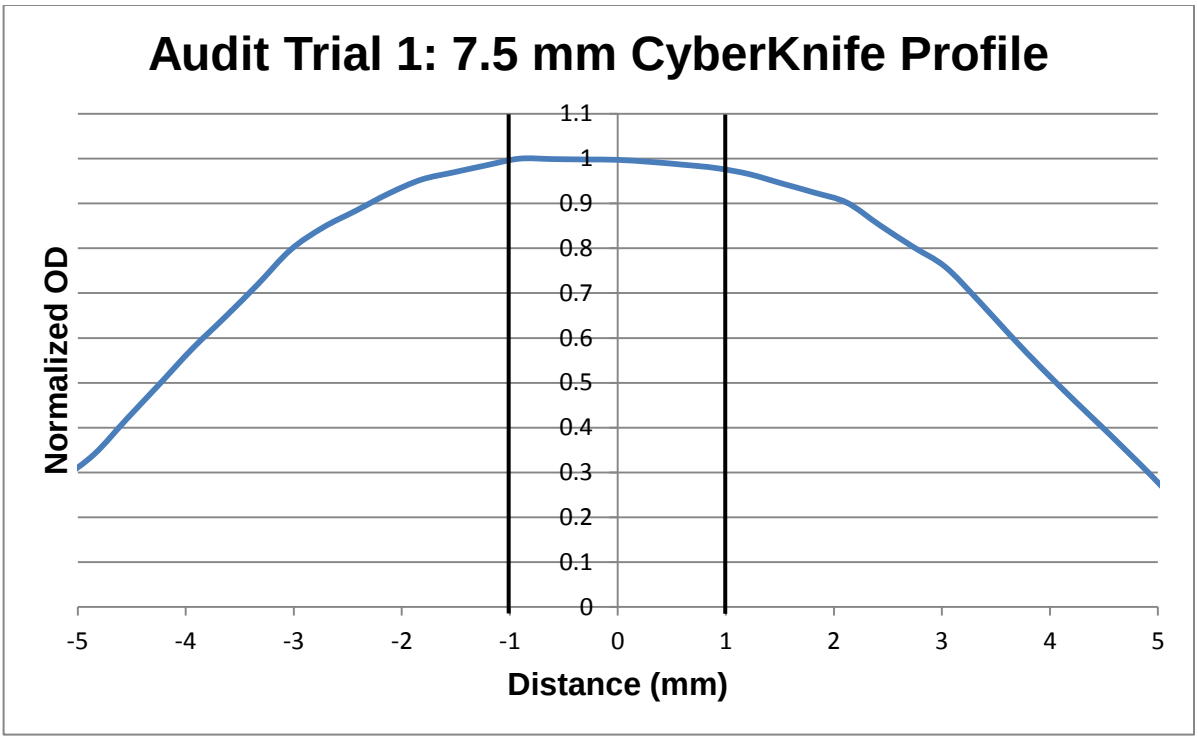

Figure 3.18: Trial 1 dose profile for a 7.5 mm diameter field.

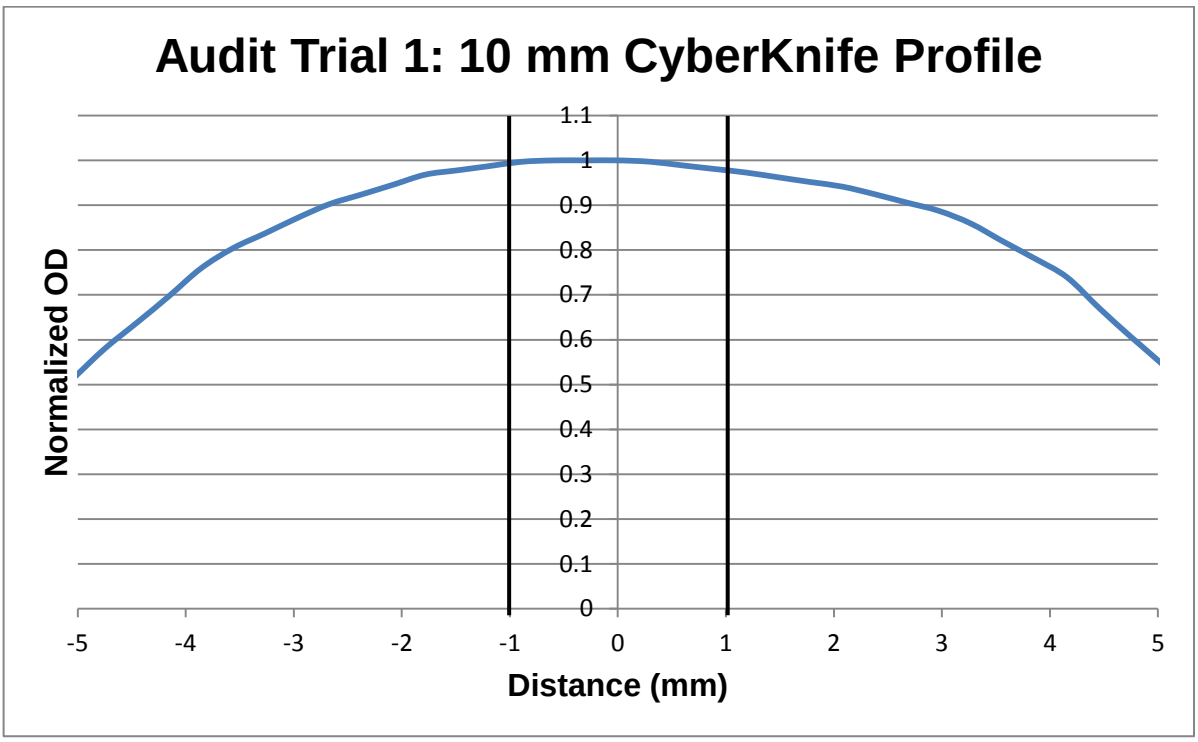

Figure 3.19: Trial 1 dose profile for a 10 mm diameter field.

4 Discussion

4.1 System Sensitivity

The system sensitivity defined for this study used masked OSLDs that were highly reproducible. The RPC plans on using the regular unmasked OSLDs to define the system sensitivity of the masked system for their remote audits. Therefore a scaling factor is needed to convert the unmasked to masked OSLD system sensitivity. This scaling factor was determined to be 3.9 from this study by taking the ratio of the average dose to count ratio of the unmasked to mask OSLDs irradiated under identical conditions on the same day. Six masked and unmasked OSLDs were irradiated the same way normal standard OSLDs were irradiated described in Section 2.2.2.2. This factor should be verified when new masked OSLDs are commissioned by the RPC.

4.2 Linearity

The resultant linearity correction factor from this work was compared with the RPC's commissioning linearity correction factor for unmasked OSLDs. The RPC's linearity correction factor shown in Equation 2.6 for the same batch is displayed again here for reference.

$$\mathrm{K_{L,RPC}} = -0.000245071 * (\text{raw dose}) + 1.02451 \tag{2.6}$$

The study's linearity correction factor and the RPC's linearity correction factor are compared in Figure 4.1. The normalized average measured K_L values are also plotted with standard deviation (1σ) error bars.

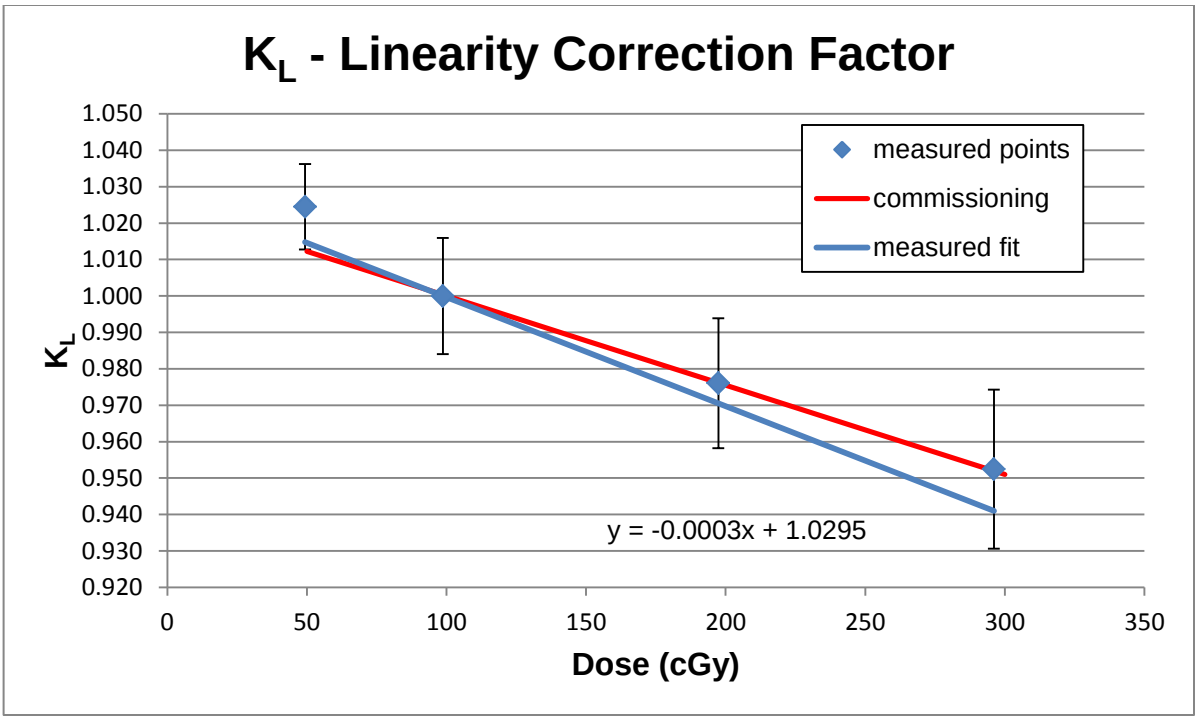

Figure 4.1: Linearity curves of measured and commissioning data. The masked OSLD measured points are compared to the commissioning data of non-masked OSLDs determined by the RPC.

The RPC wishes to use the already existing linearity correction factor for unmasked OSLDs determined during commissioning of the batch. The average measured linearity correction factors line up directly over the commissioning curve in Figure 4.1. The results from the study agree with the RPC's commissioning. It can be expected that the linearity correction factor of unmasked OSLDs obtained during commissioning of a batch can be used for masked OSLDs for the same batch.

4.3 Fading

Another study was performed that investigated the fading after two weeks to a month and showed a signal drop of 2%[58]. Both of these results matched the data obtained by the RPC which showed a 2% drop in signal after the first five days and two to four weeks post irradiation[31].

4.4 Energy and Phantom Scatter Correction Factor

A separate test was performed by irradiating the full phantom using a ^{60}Co beam and using the system sensitivity define by that test for a full phantom irradiate with a 6 MV beam. This test determined the combined K_E and K_{Sc} effect. Table 4.1 shows the results of six trials performed for this test.

Table 4.1: Energy and phantom scatter correction factor

Trial	K_E*K_{Sc}
1	1.016
2	1.010
3	1.013
4	1.040
5	1.030
6	1.040

The average of the six trials was 1.025 with a standard deviation (1σ) of 0.013. Multiplying the average K_E from section 3.7 and average K_{Sc} from section 3.8, K_E*K_{Sc} = 1.026. The test above confirms the results of both K_E and K_{Sc} measured independently in the previous sections.

4.5 Field Size Dependence Factor

The field size dependence factor was determined to be unity however the uncertainty associated with the correction factor must still be taken into account. Due to the complexities of small field dosimetry, the field size dependence factor accounts for differences in the field size, geometry, beam quality of the reference field and machine specific reference field[18,23,59]. The uncertainty in the system must be accounted for in the uncertainty calculations to address the issues of small field dosimetry.

4.6 Remote Audit Trials

The purpose of the remote audit trials were to compare the treatment planning system's (TPS) calculations to the RPC's OSLD measured results and determine if the TPS calculations were correct or not. The results from the mailable remote audit trials showed that the phantom with masked OSLDs can accurately measure dose down to 10 mm diameter cone sizes and a 1 x 1 cm^2 field size. The Elekta and Varian measurements showed good agreement with the RPC calculated dose; however the CyberKnife data showed a larger disagreement. Figure 4.2 shows a dose profile comparison of a 10 mm diameter field for both the CyberKnife and linac based cone system. The circular collimator has greater coverage over the masked OSLD compared to the CyberKnife profile. Greater coverage results in less volume averaging. CyberKnife units are a flattening filter free system, while TrueBeam units have a flattening filter or flattening filter free system, which can explain the profiles seen in Figure 4.2 and the lower dose calculations seen in Table 3.8. In addition to the profile, other CyberKnife disagreements such as the CyberKnife TPS calculation is more inaccurate and CyberKnife setup not having the same precision as a linac can result explain the ratio observed from the remote audit trial. The MLC ratio increased from a 1 x 1 cm^2 to 2 x 2 cm^2 field. There is field size dependence factor for MLC leakage due to increase in leaf scatter with increasing field size[60].

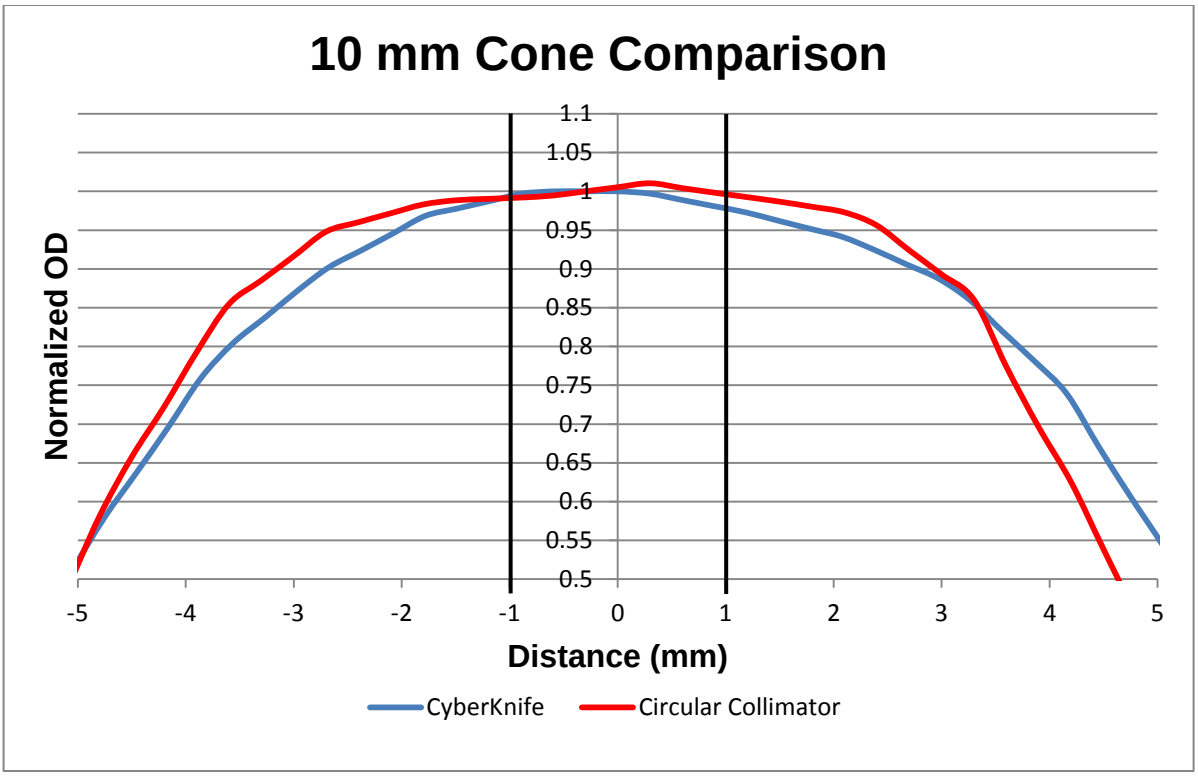

Figure 4.2: Dose profile comparison of a 10 mm diameter field defined by a CyberKnife unit and a linac based cone system.

The RPC to institution dose ratio for CyberKnife units using 10 mm cones averaged to 0.96 while the 1 x 1 cm^2 MLC defined field had an ratio of 1.006. The linac based cones audits performed very well with an average ratio of 0.978 for the 10 mm field noting that one institution showed a 5% under response while the other two had less than a 2% difference. Although the 7.5 mm audits had good profile coverage over the masked OSLDs, the RPC has decided to limit the minimum field size for the SRS masked OSLD phantom to 10 mm and 1 x 1 cm^2 to reduce any uncertainty in user position error.

4.7 Uncertainty Analysis

Equation 2.3 depicts the dose equation for the masked OSLD system used in this study and is repeated again here.

$$\text{Dose} = (\text{Avg Corrected Rdg}) * \text{ECF} * \text{S} * \text{K}_\text{L} * \text{K}_\text{F} * \text{K}_\text{E} * \text{K}_\text{Sc} * \text{K}_\text{FSD} \tag{2.3}$$

System sensitivity, shown in Equation 2.5, combines multiple components that need to be analyzed individually to provide the final system sensitivity uncertainty. Aguirre et al.[4] has already determined the individual uncertainties for system sensitivity by adding them in quadrature.

$$\begin{aligned} \sigma_\text{S} &= \sqrt{\sigma^2_{\text{Dose to std}} + \sigma^2_{\text{Avg Avg Rdg}} + \sigma^2_{\text{F,std}} + \sigma^2_{\text{L,std}}} \\ &= \sqrt{(0.6\%)^2 + (0.4\%)^2 + (0.3\%)^2 + (0.1\%)^2} \\ &= 0.8\% \end{aligned} \tag{4.1}$$

Where $\sigma_{\text{Dose to std}}$ the uncertainty of the dose is delivered to standards, $\sigma_{\text{Avg Avg Rdg}}$ is the uncertainty in the averages of the two standards, $\sigma_{\text{F,std}}$ is the uncertainty in the fading correction factor, and $\sigma_{\text{L,std}}$ is the uncertainty in the linearity correction factor. The linearity uncertainty for the standard was determined by the 95% confidence interval in the linear fit while the other uncertainties are defined at one standard deviation.

Dose measurement uncertainty analysis can be applied to the dose equation by adding the individual term's uncertainty in quadrature.

$$\sigma_\text{Dose} = \sqrt{\sigma^2_{\text{Avg Inst Rdg}} + \sigma^2_\text{ECF} + \sigma^2_\text{S} + \sigma^2_{\text{K}_\text{L}} + \sigma^2_{\text{K}_\text{F}} + \sigma^2_{\text{K}_\text{E}} + \sigma^2_{\text{K}_\text{Sc}} + \sigma^2_{\text{K}_\text{FSD}}} \tag{4.2}$$

$\sigma_{\text{Avg Inst Rdg}}$ is the percent uncertainty in the institution's OSLD reading and does not include standards or controls. The uncertainty in the institution's reading is larger than the uncertainty in controls and standards because the irradiation conditions are

not as well defined. Aguirre defined $\sigma_{\text{Avg Inst Rdg}}$ = 0.57% and includes the uncertainty in ECF. Therefore σ_{ECF} = 0 in Equation 4.2. The linearity correction uncertainty was given by the 68% confidence interval for doses between 190 to 210 cGy. The linearity uncertainty shown in Figure 3.9 was 0.55%. The fading correction uncertainty was provided by Aguirre to be 0.15%4. The energy correction and phantom scatter correction uncertainty were 0.5% and 1.3% respectively. The field size dependence uncertainty was also determined by using the 68% confidence interval in Figure 3.14. The field size dependence uncertainty was defined for a 1 x 1 cm^2 field size and determined to be σ_{FSD}= 0.5%. Using Equation 4.2, the total dose uncertainty of the system can be calculated.

$$\begin{aligned}\sigma_{\text{Dose}} &= \sqrt{(0.57\%)^2 + (0\%)^2 + (0.8\%)^2 + (0.55\%)^2 + (0.15\%)^2 + \cdots} \\ &\quad + (0.5\%)^2 + (1.3\%)^2 + (0.5\%)^2 \\ &= 1.86\%\end{aligned} \tag{4.3}$$

If we assume that the OSLD dose measurements follow a normal distribution, approximately 95.4% of the measurements will fall within two standard deviations (2σ) of the mean. The total dose uncertainty for the masked OSLD system is 3.72% at 2σ. Kirby et al.2 performed an uncertainty analysis of the RPC mailed TLD program and established a ±5% acceptance criterion for institutional measurements. This criterion was based on the TLD system calculated dose to be within 5% of ion chamber measurements 93% of the time. A ±5% acceptance criterion represents four standard deviations. With a dose uncertainty of 1.86%, greater than 95.4% of dose measurements will fall within four standard deviations of the mean. Therefore using a ±5% acceptance criterion for this system was appropriate for SRS measurements.

The dose uncertainty was analyzed experimentally by taking the ratio of the measured to expected doses from 73 separate dose measurements. These measurements were taken from various parts of the study and also included the remote audits. The measured doses were calculated from the OSLD readings using the dose equation from Equation 2.3 while the expected doses were calculated by using Equation 2.2 or provided by the institutions. The results from all the measurements are shown in Figure 4.2.

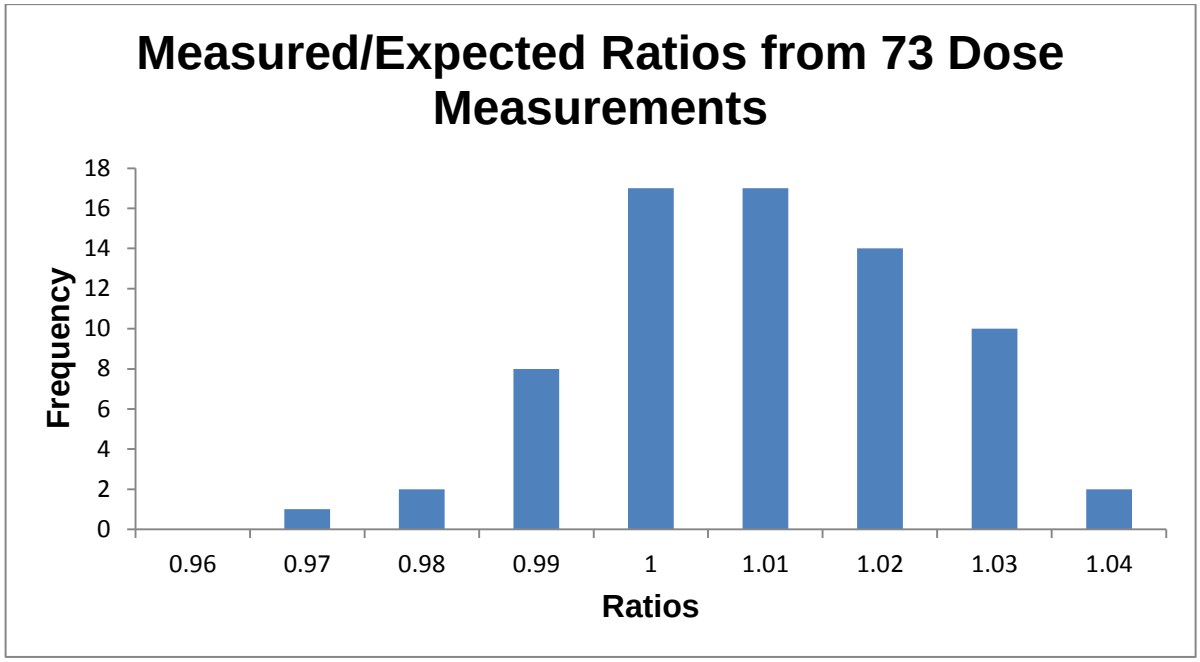

Figure 4.3: Histogram of the measured to expected dose ratios for 73 separate measurements.

The average ratio for all 73 measurements was 1.005 with a standard deviation of 0.017. A two standard deviation uncertainty of 3.4% of measured to expected dose ratio is within the 3.72% total system uncertainty determined previously.

5 Conclusion

5.1 Conclusion

The hypothesis for this study was: *Optically stimulated luminescent dosimeters whose visible active luminescent area have been masked can be used as a remote audit tool to measure small photon fields down to a 7.5 mm diameter field size with an accuracy of ±5% as compared to existing dosimetry measurements and Monte Carlo calculations with an uncertainty of less than 2%.*

This study determined that a masked OSLD and phantom system can be used as an RPC mailed remote audit tool for small field dosimetry. The phantom was made of High Impact Polystyrene, which provides a durable and cost efficient tool for the mailed dosimetry program. The 2 mm masked OSLDs showed good reproducibility and were accurately characterized to measure small photon beams. The OSLD system will replace the existing TLD program, which will allow the RPC to measure field sizes down to a 10 mm cone compared to the 12.5 mm cone size for TLDs. A 7.5mm diameter field size was achievable under controlled conditions; however the RPC will limit the system to the 10 mm diameter field to reduce any positioning uncertainty by the user. Irradiations performed on the phantom should be simple and straightforward for institutions through the clear and concise instructions provided.

The total dose uncertainty of the masked OSLD and phantom design was 3.72%. The accuracy of the system seen in this work was sufficient to establish a ±5% acceptance criterion for comparing the OSLD dose measurements with the

institution's reported dose. Multiple remote audit trials have been performed with the majority of the RPC measured to institution reported dose ratios falling within the criteria.

Initially, the project aimed at using the 1 mm diameter masked OSLDs throughout the study; however results showed that a 1 mm mask was not appropriate for the system. Although measuring a 7.5 mm diameter field size with a total system uncertainty of 2% was not accomplished through this study, it has been shown that the masked OSLD and phantom system are capable of improving the existing SRS remote audit dosimetry program, allowing the RPC to measure smaller field sizes than before.

5.2 Future Work

Before this system becomes implemented into the RPC remote audit tool program, several steps will need to occur first. OSLDs are batch specific and each batch will need to be recharacterized. Most of the correction factors have been determined throughout this work and the RPC commissioning data for non-masked OSLDs can be used for the masked OSLD system. A new set of masks need to be carefully cut and applied to each OSLD. A new ECF value must be determined for each masked OSLD. The RPC will be using the system sensitivity factor from non-masked OSLDs for the masked OSLD system requiring a scaling factor to obtain the correct dose per count ratio.

Current instructions ask institutions to line up the phantom using the crosshairs. However, crosshairs are not used clinically during patient setup. A

further redesign of the phantom can incorporate laser markings on the phantom for irradiation setup.

A full Monte Carlo calculation can be performed where the SRS phantom can be modeled with masked OSLDs inside the phantom. The calculations can be compared with the measured OSLD data.

6 Appendix

6.1 Phantom Design

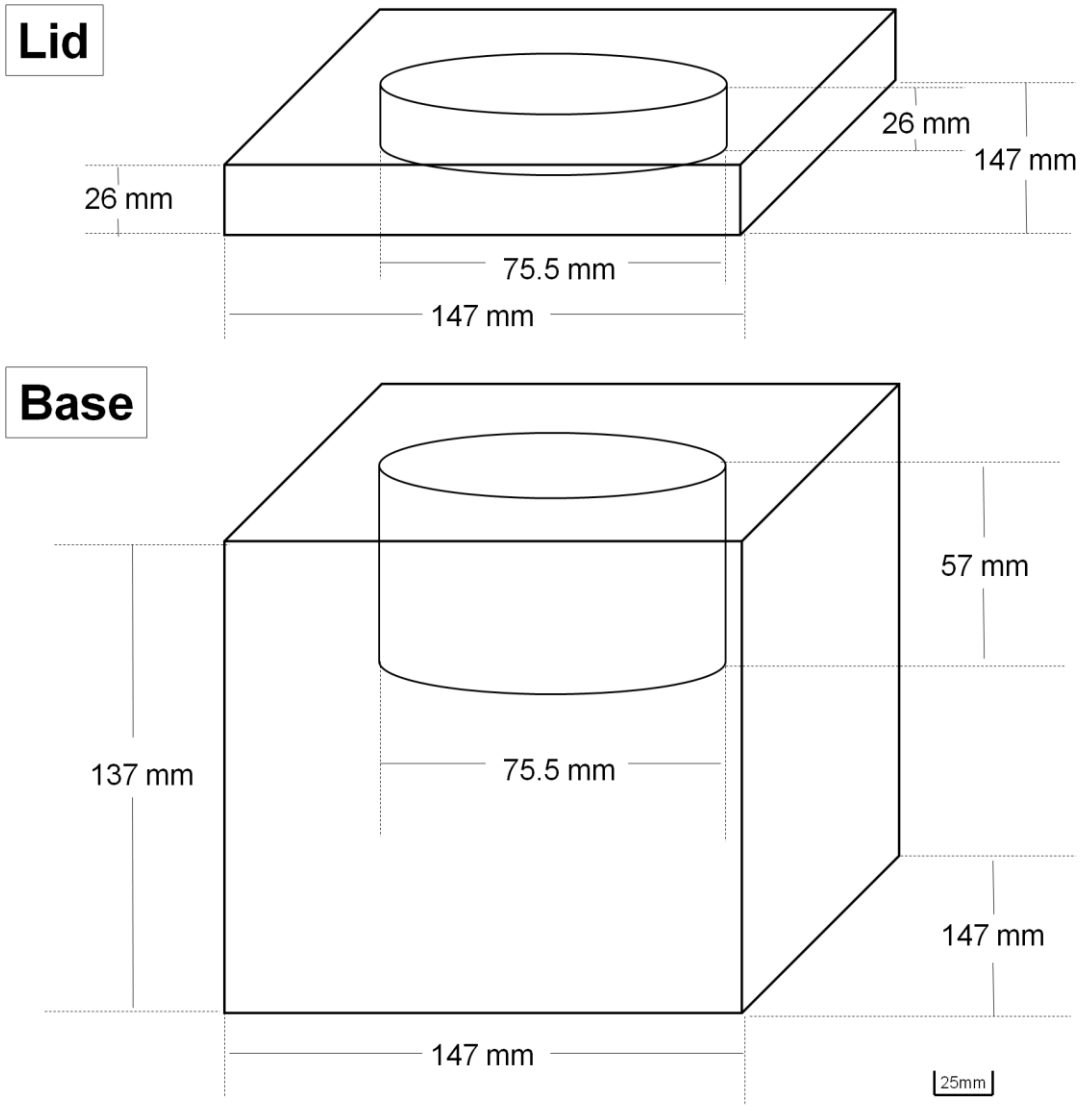

Figure 6.1: Phantom dimensions of lid and base. The cylindrical insert is placed in the center of the base followed by a lid which is screwed down to the base to reduce air gaps and lock the cone in place.

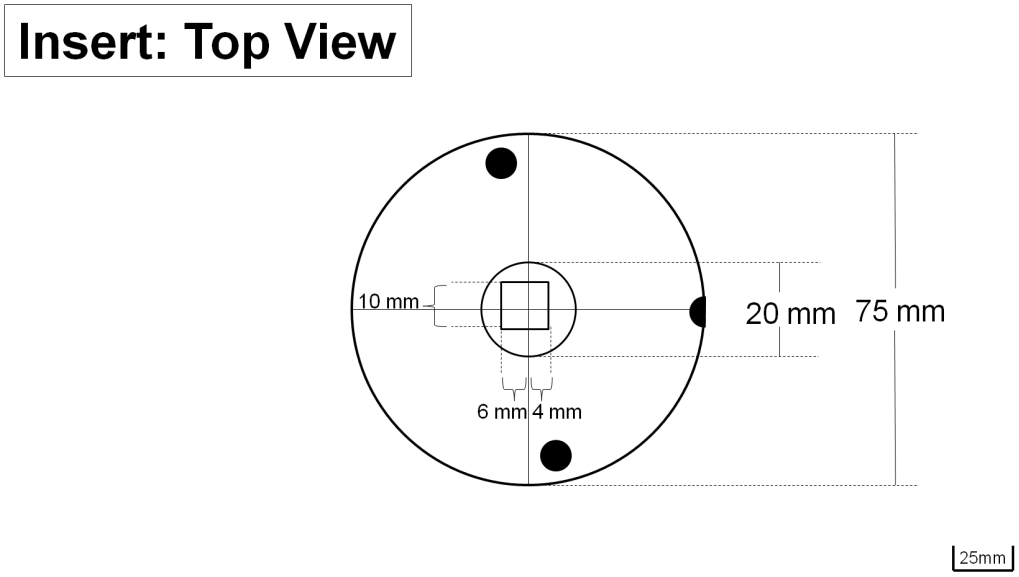

Figure 6.2: Top view of the insert. Thin cross hairs are drilled into the top of the insert used to center the phantom with the field. The square in the middle represents the shift in the OSLD due to the non-centered location of the Al_2O_3:C.

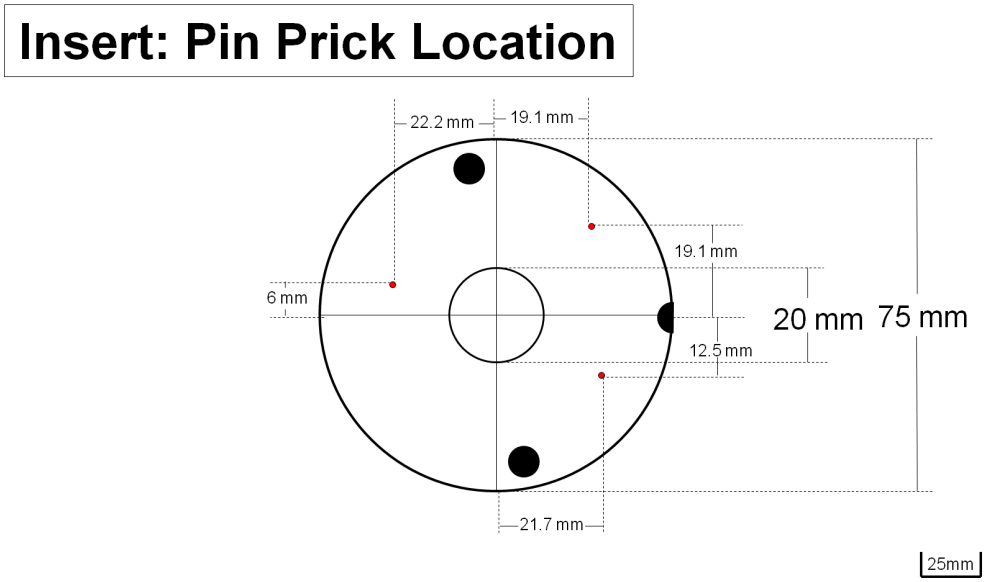

Figure 6.3: Pin prick location. The cone insert has three pin prick locations that relate the pin pricks to the center of the phantom.

6.2 Film Profiles

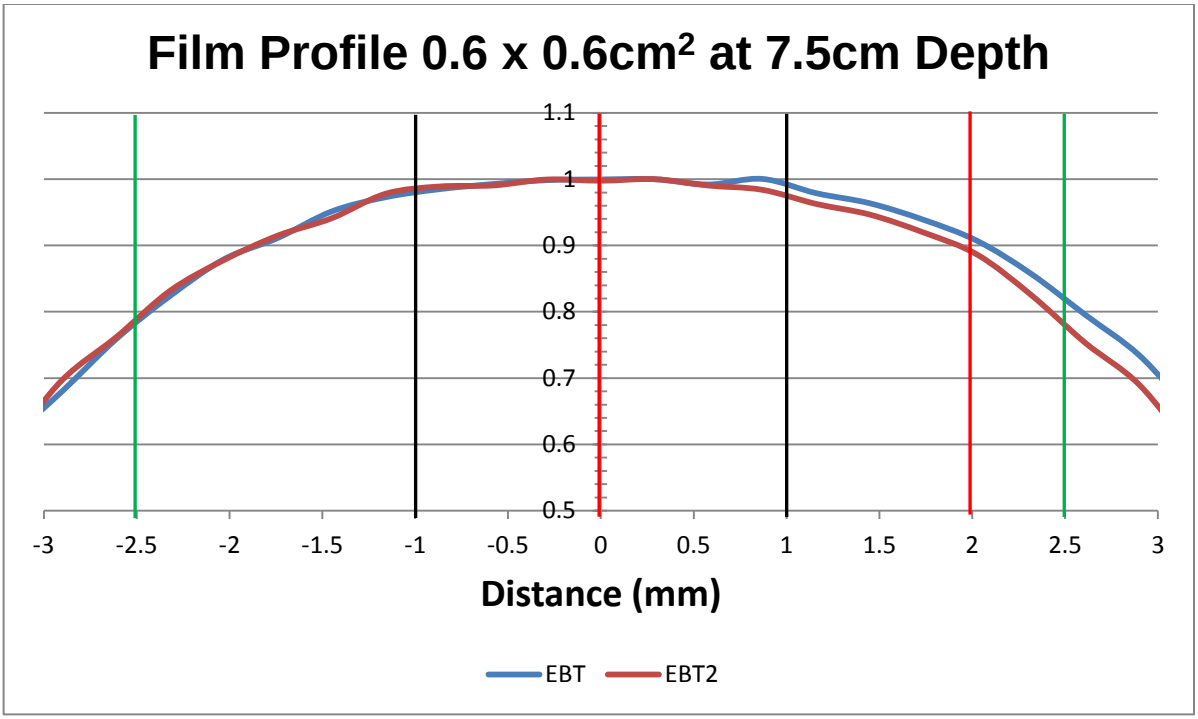

Figure 6.4: Film profiles of EBT and EBT2 for a 0.6 x 0.6 cm^2 field size at 7.5 cm depth.

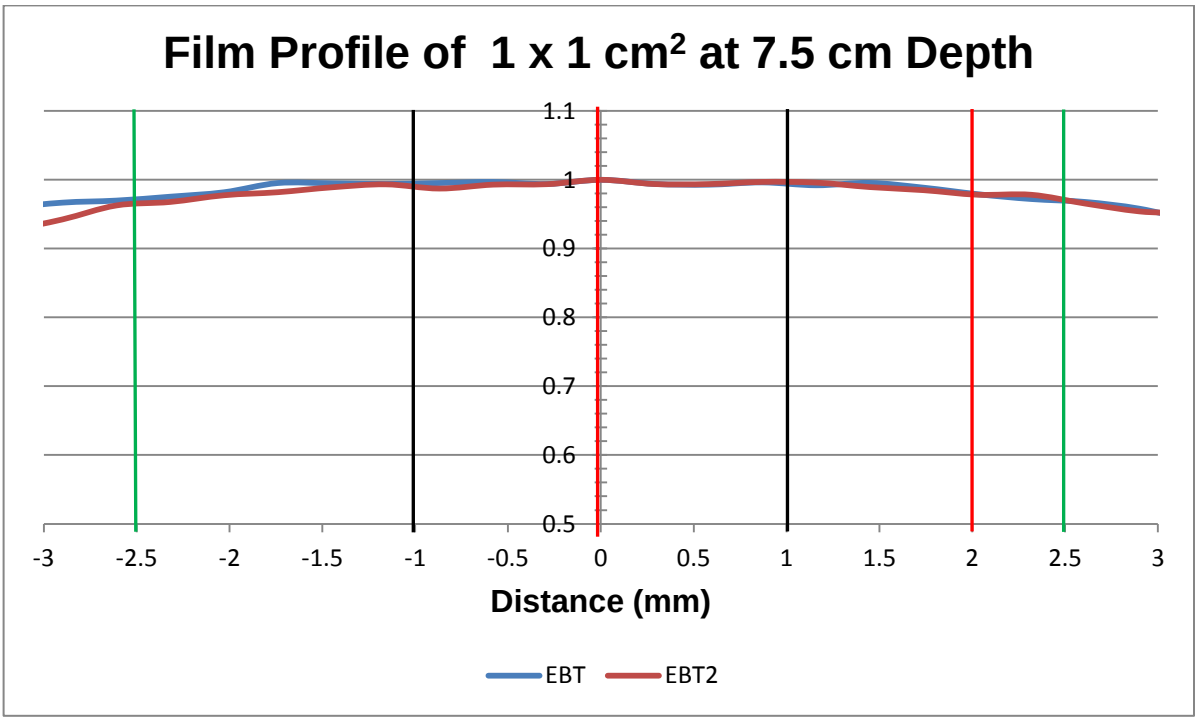

Figure 6.5: Film profiles of EBT and EBT2 for a 1 x 1 cm^2 field size at 7.5 cm depth.

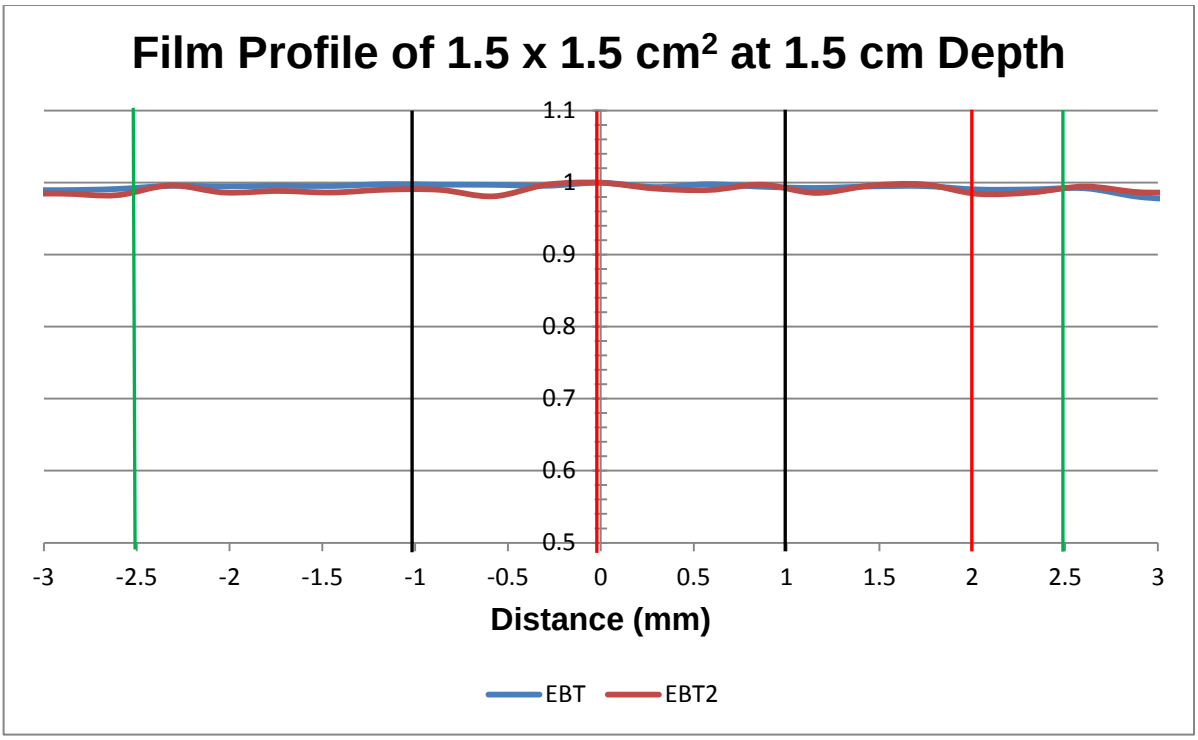

Figure 6.6: Film profiles of EBT and EBT2 for a 1.5 x 1.5 cm^2 field size at 1.5 cm depth.

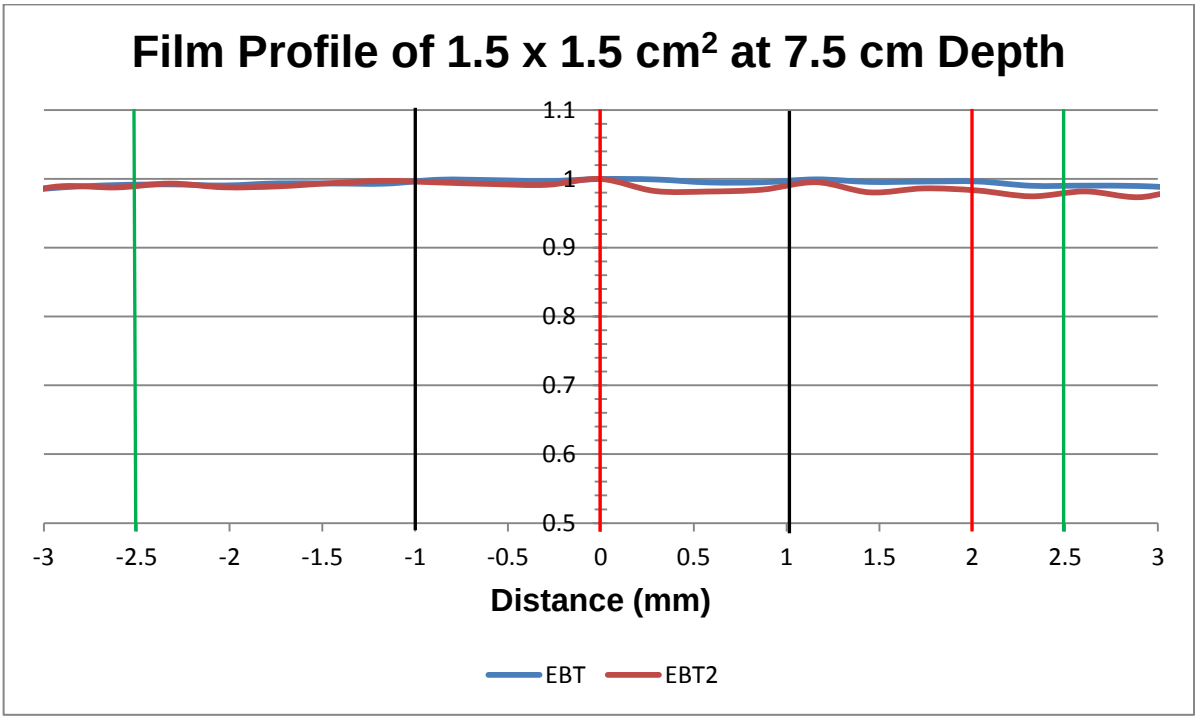

Figure 6.7: Film profiles of EBT and EBT2 for a 1.5 x 1.5 cm^2 field size at 7.5 cm depth.

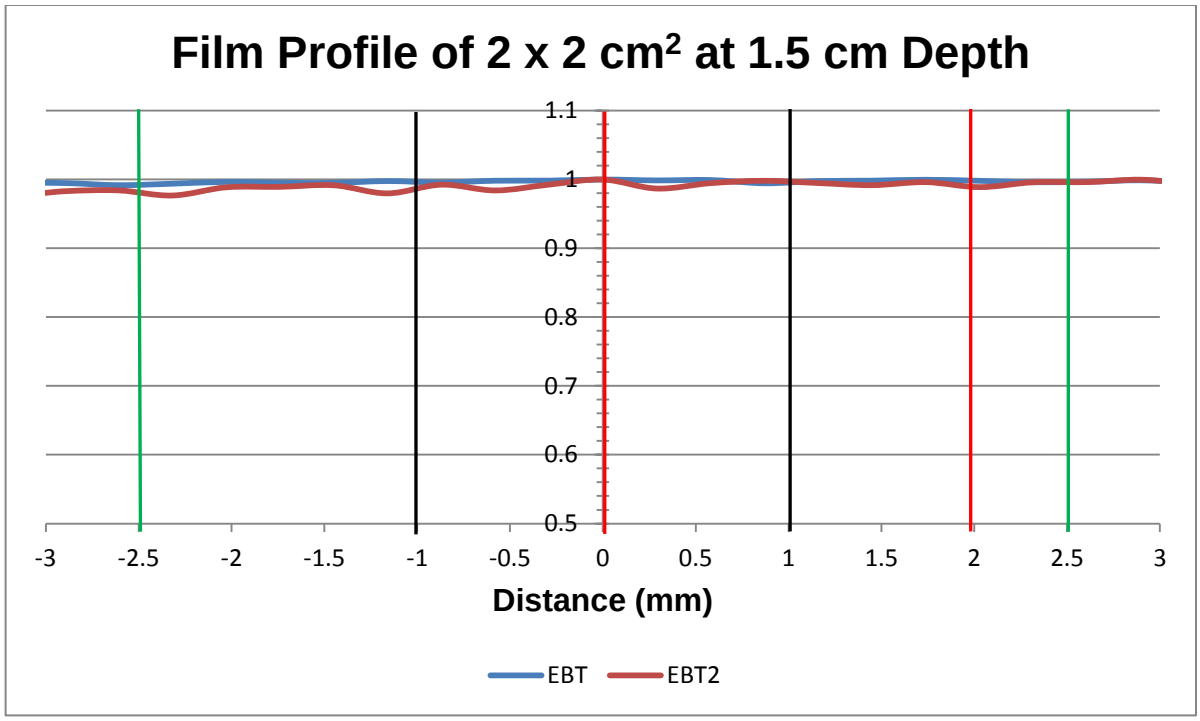

Figure 6.8: Film profiles of EBT and EBT2 for a 2 x 2 cm^2 field size at 1.5 cm depth.

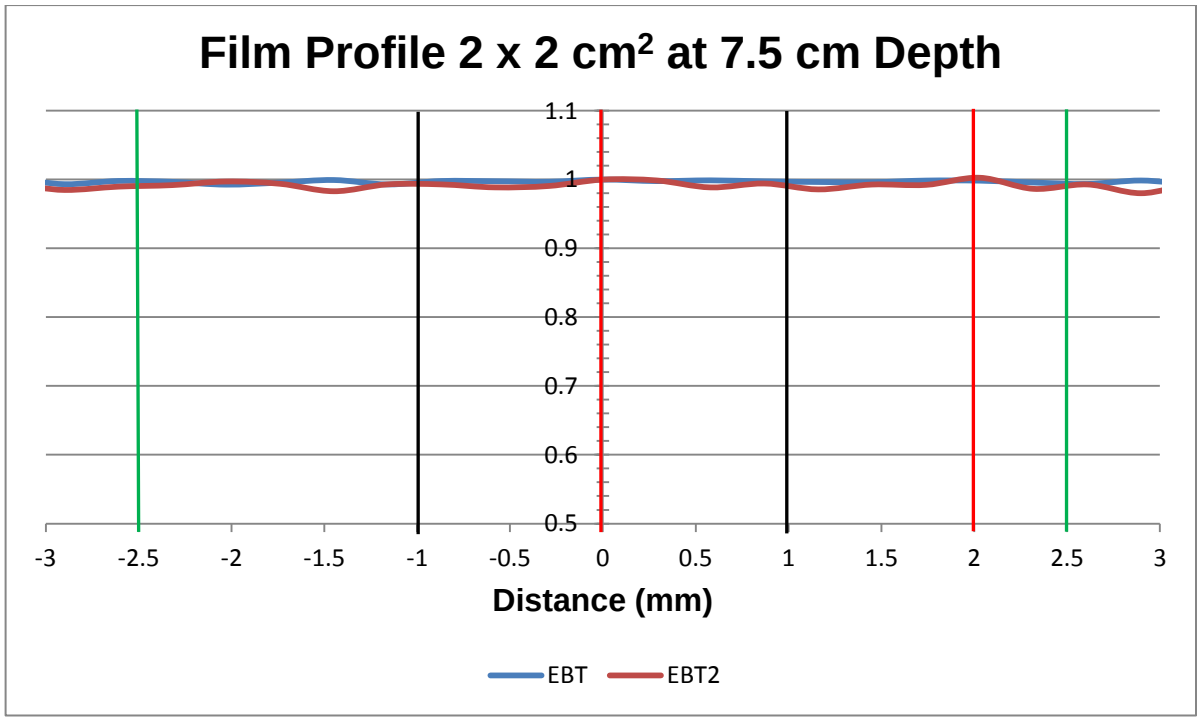

Figure 6.9: Film profiles of EBT and EBT2 for a 2 x 2 cm^2 field size at 7.5 cm depth.

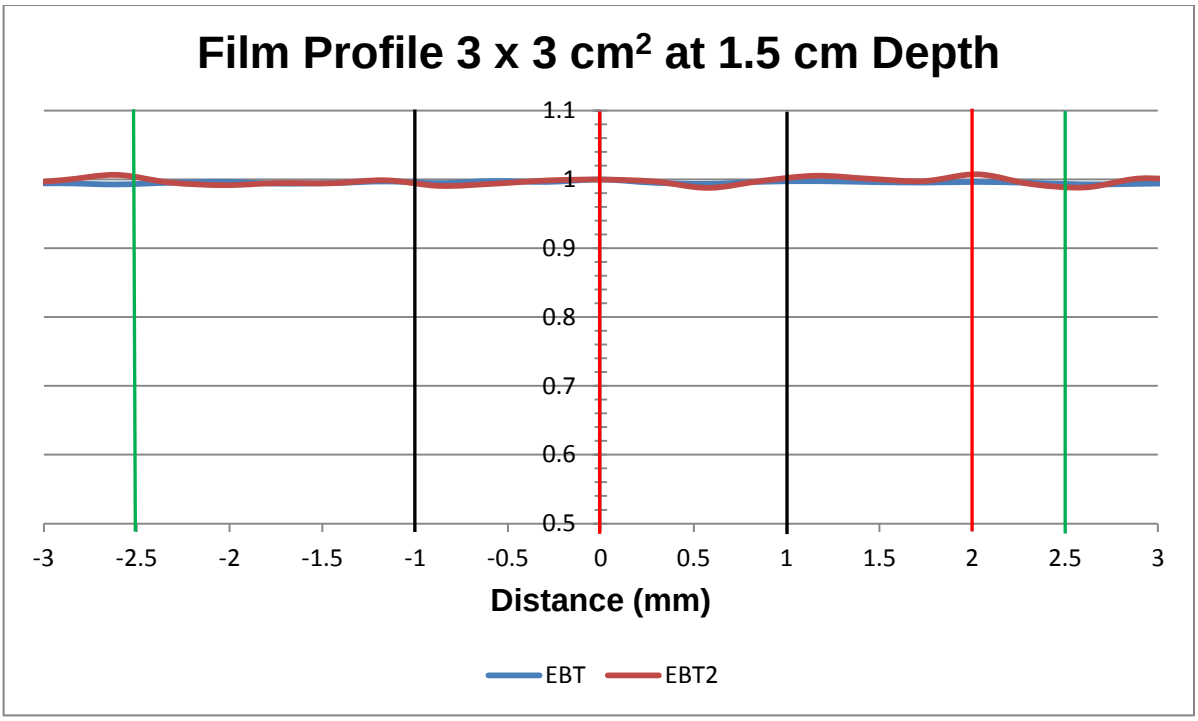

Figure 6.10: Film profiles of EBT and EBT2 for a 3 x 3 cm^2 field size at 1.5 cm depth.

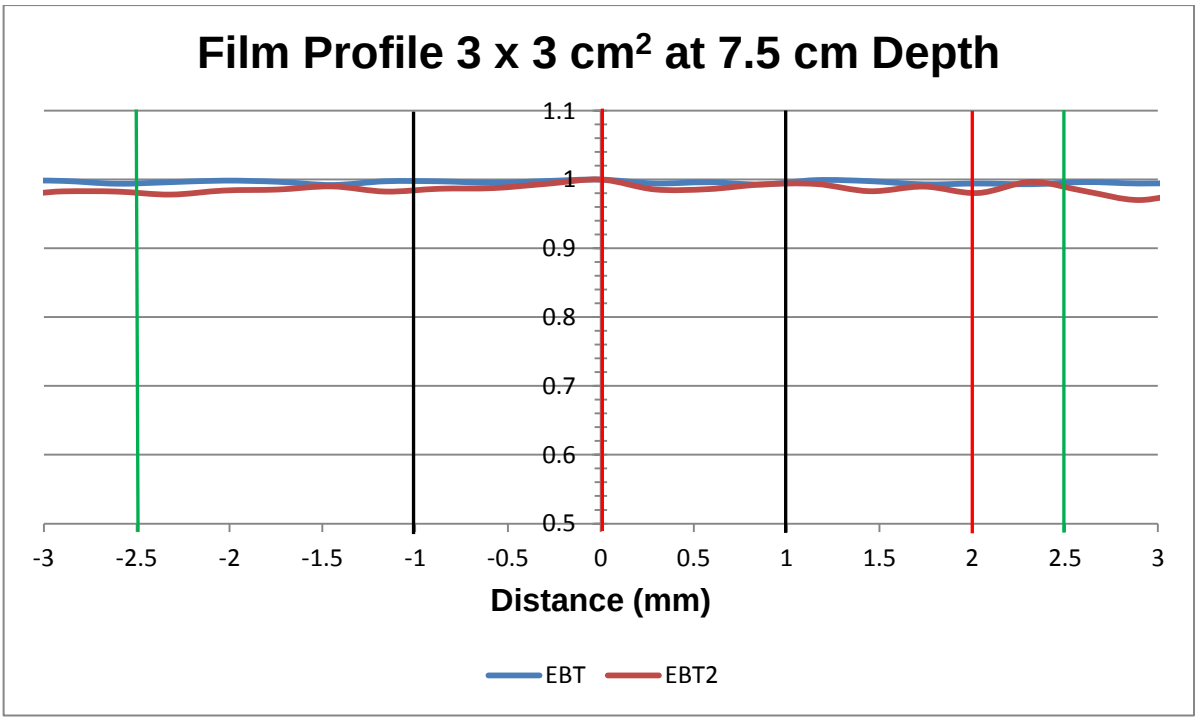

Figure 6.11: Film profiles of EBT and EBT2 for a 3 x 3 cm^2 field size at 7.5 cm depth.

6.3 Remote Audit Forms

6.3.1 Instructions

INSTRUCTIONS FOR USE OF SINGLE-BEAM STEREOTACTIC RADIOSURGERY PHANTOM

Version: July 2013

If you have any questions, please contact:

Christopher Pham	Office: (713) 745-8989	Email: cpham1@mdanderson.org
	Cell: (408) 421-6215	Personal: chrispham62@gmail.com

Please find enclosed the “Single-Beam Stereotactic Radiosurgery” verification system (Fig. 1). This system is comprised of a phantom base, a top plate and, and a cylindrical dosimetry insert. Each dosimetry insert contains 2 OSLD, located at a depth of 1.5 cm, and a film plate, located above the OSLDs. The phantom base and top plate provide adequate scattering conditions.

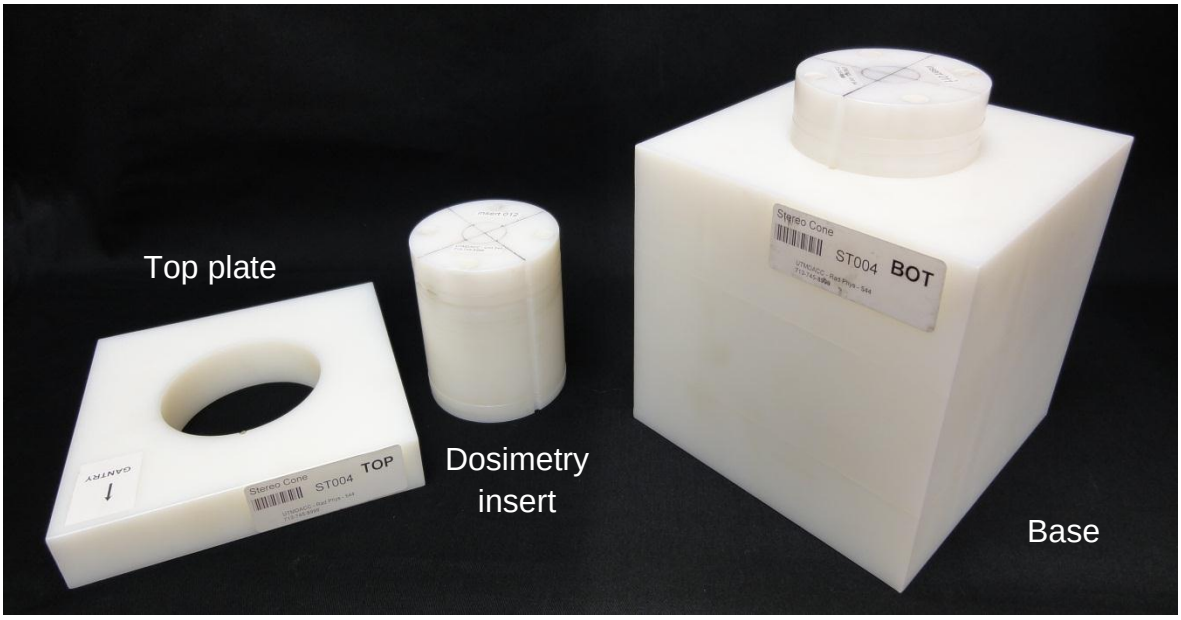

Figure 1: Single-Beam Stereotactic Radiosurgery verification system

Instructions for use:

1. Verify the machine reference output.

2. Place the phantom base block on the treatment couch, with the side labeled “G” towards the gantry. Use a level to ensure that the block is level. Shim the phantom, or move it to a more level segment of your treatment couch, if necessary.

3. Insert the cylindrical insert into the base if not already done so. The cylinder will fit into the phantom base in only one orientation, determined by the key in the block.

4. Slide the top plate over the insert, with the gantry arrow pointing towards the gantry. The SRS Single-Beam verification system will look like the setup in Fig.2.

Figure 2: Assembled SRS Single-Beam verification system

5. Set your SRS machine to 100cm SSD (if possible) to the surface of the cylindrical insert.

6. Attach the SRS cone to be verified to your accelerator. **(NOTE: The smallest cone diameter that can be used is 7.5 mm.)** Use a spirit level to ensure that the cone and as such, the photon beam are vertical. The level should be

placed on a machined surface; the attachment plate for the cone is generally a convenient place.

7. Center the phantom in your treatment field. The cylindrical insert is marked with a 2 cm diameter circle as well as two perpendicular scribe marks intersecting at the center of the cone. The block should be set up based on the projection of the **light field** rather than lasers. **(NOTE: The small field sizes, sharp dose gradients and dosimeter size associated with the SRS verification require lining up the SRS cone delivery system and SRS verification phantom dosimetry insert as accurately as possible in order to ensure an accurate measurement.)**

8. Calculate the monitor unit setting to deliver approximately **200 cGy** to a point at a 1.5 cm depth in water for 6MV beam, centered in the field (the location of the OSLD).

9. Irradiate the phantom to the monitor units calculated.

10. Record the cone identification (7.5mm, 10mm, 12.5mm, etc.) or MLC field size (1x1cm), the monitor unit setting, and the calculated doses at 1.5 cm depth in a water phantom on the attached irradiation form.

11. Remove the top plate and place it aside.

12. Remove the irradiated dosimetry and store it outside the treatment room (more information on replacing the OSLDs in the cone is attached).

13. Repeat steps 3 through 12 for any additional SRS cones you wish to verify.

14. Ensure that the irradiation form has been completely filled out (the irradiation form has 2 pages).

15. Place all of the SRS Single-Beam verification system materials in the original packaging and return using the prepaid enclosed shipping label. Be sure to lock the case, using the lock provided.

INSTRUCTIONS FOR REPLACING THE OSLDs AND FILM IN THE SINGLE BEAM SRS PHANTOM

1. Once irradiations are performed, remove entire phantom from current position on the table. (We want you to reposition the phantom every time)

2. Remove top plate by first unscrewing the large screws located at the edges of the top plate followed by removing the cylindrical insert.

3. Unscrew and remove one of the screws from the insert. Loosen the other screw enough such that the individual compartments of the cylinder can be rotated about the screw axis (Figure 1).

Figure 1: Film and OSLD cylindrical insert

4. Carefully remove the film with the gloves provided and place in the black envelope labeled “Institution Film”.

5. Remove the OSLDs by tipping the insert sideways or lightly tapping on a surface. Place OSLDs in the corresponding field size bag.

6. Replace the film with a new film from the black envelope labeled “Block Phantom Film New” using the gloves provided. Place the film with the

number facing up and the black dot pointing at the indent on the side of the plate.

7. Place new OSLDs in the OSLD slot with the barcode facing up and pointed towards the “QRC” label (Figure 1).

8. Record the last 3 digits of the OSLD located on the back (i.e. DN080 709 57H) and the film number on the forms provided for the corresponding cone or MLC.

9. Rotate the plates back to center (carefully rotate the film plate such that it does not shift out of the groove). Place the screw back into the insert and tighten both.

10. Use the needle provided and place into the 3 black holes located at the top of the insert. Apply enough pressure such that you make an indent or hole in the film.

11. Place insert back into the base and place the top on afterwards such that no air gaps are present. (Note: you do not need to screw the large screws as long as the insert and top are firmly in place.)

12. Repeat steps 1-11 for any additional SRS cones or MLCs you wish to verify.

6.3.2 Irradiation Forms

SRS Single-Beam Phantom Verification System
Irradiation Form

Institution: _____

Address:_____

_____

Person performing irradiation: _____

Person to receive report: _____

Person to call in case of questions: _____

Phone number: _____ Fax Number:_____

E-mail address:_____

Treatment Unit: _____

Manufacturer: _____Model_____Photon Energy: _____

In-house specification:_____Serial number _____

Stereotactic system:_____

Manufacturer:_____ Model: _____

Date of Irradiation:_____

SSD: _____ cm to top of insert.

Cone/MLC Designation	Monitor Unit Setting	Dose (cGy) at 1.5 cm	OSLD #1	OSLD #2	Film #

SRS Single-Beam Phantom Verification System
Irradiation Form (cont'd)

Output of the beam: _____ cGy/MU to: □ Muscle □ Water

□ SAD □ SSD Reference field size:_____
depth:_____

Please complete the following information for each cone designation:

Cone/MLC Designation	d_{max} (cm)	Output factor at d_{max}	PDD At 1.5 cm

6.4 Remote Audit Trial Film Profiles

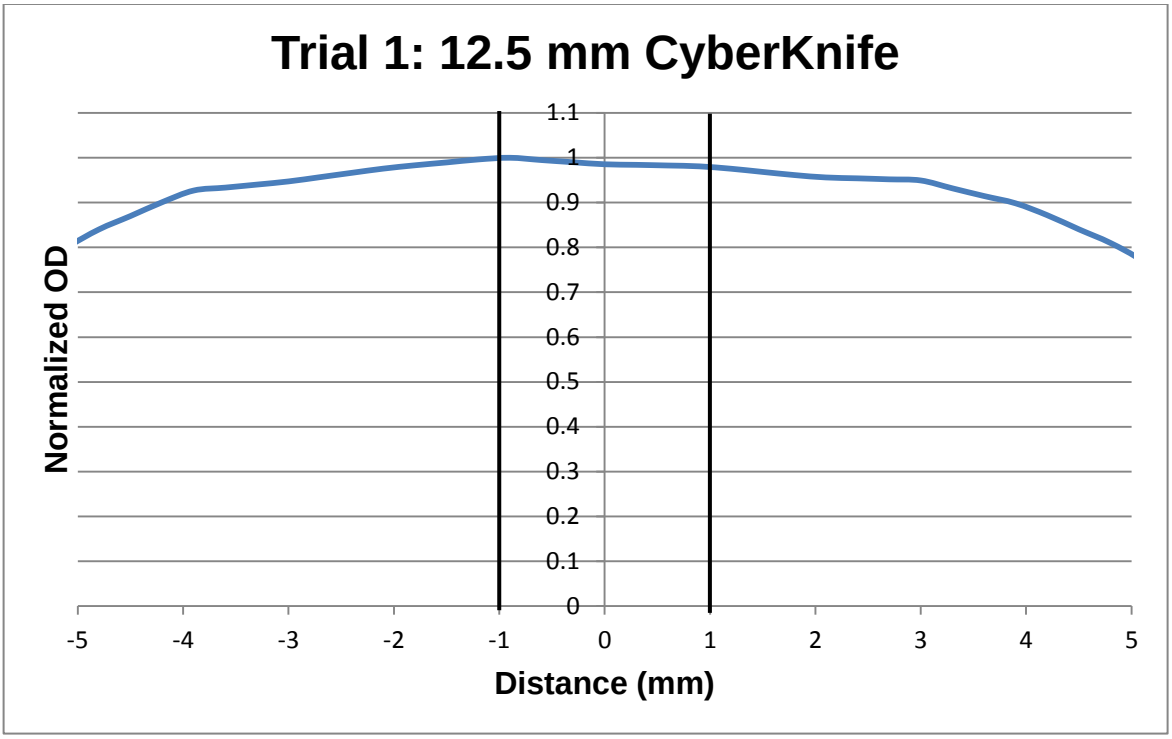

Figure 6.12: Trial 1 dose profile for a 12.5 mm diameter field.

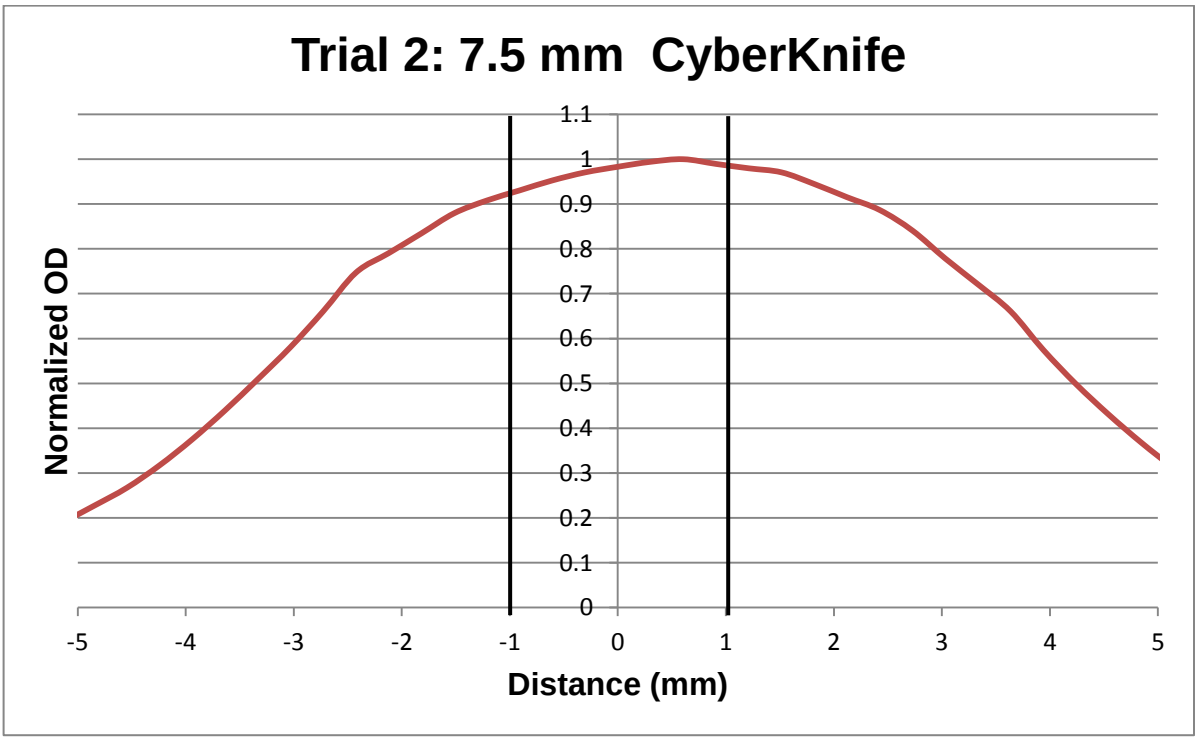

Figure 6.13: Trial 2 dose profile for a 7.5 mm diameter field.

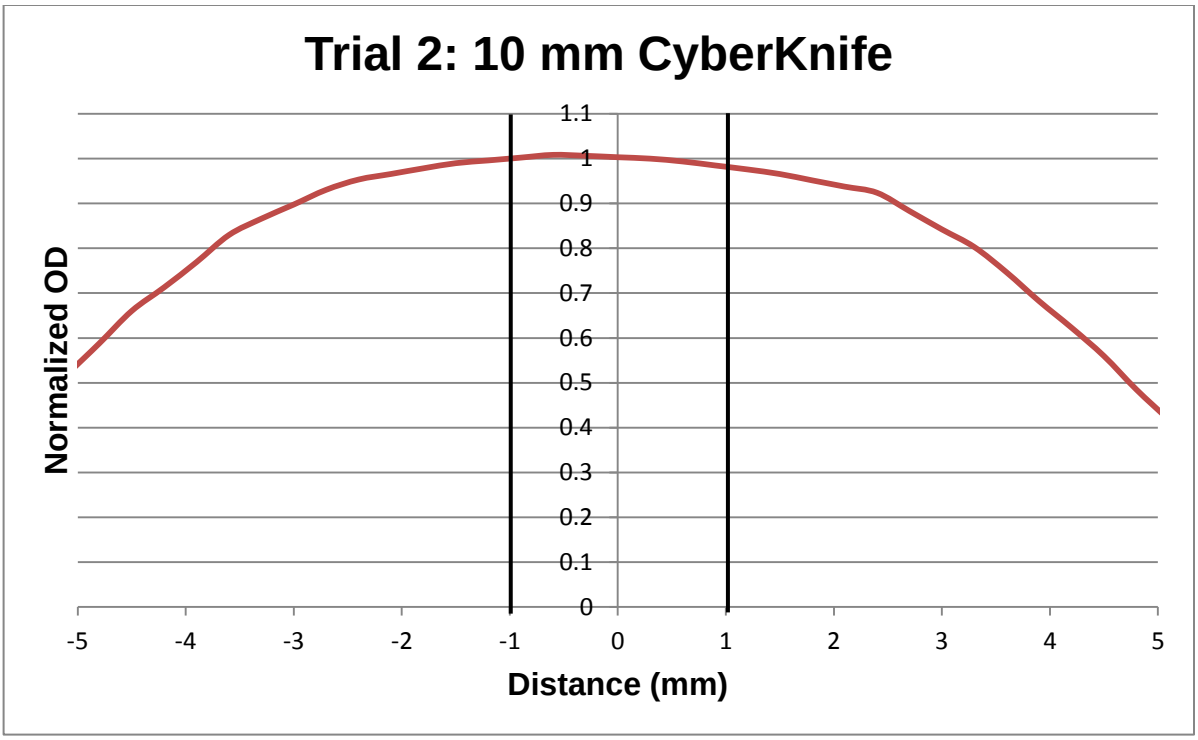

Figure 6.14: Trial 2 dose profile for a 10 mm diameter field.

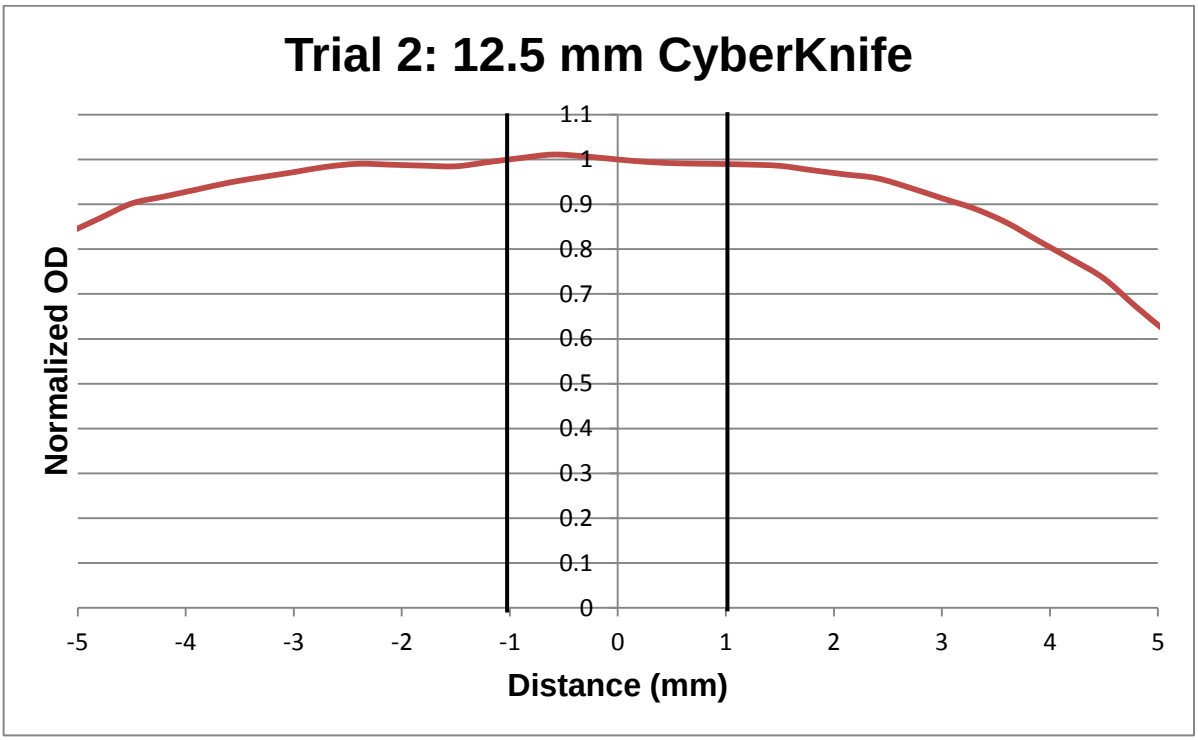

Figure 6.15: Trial 2 dose profile for a 12.5 mm diameter field.

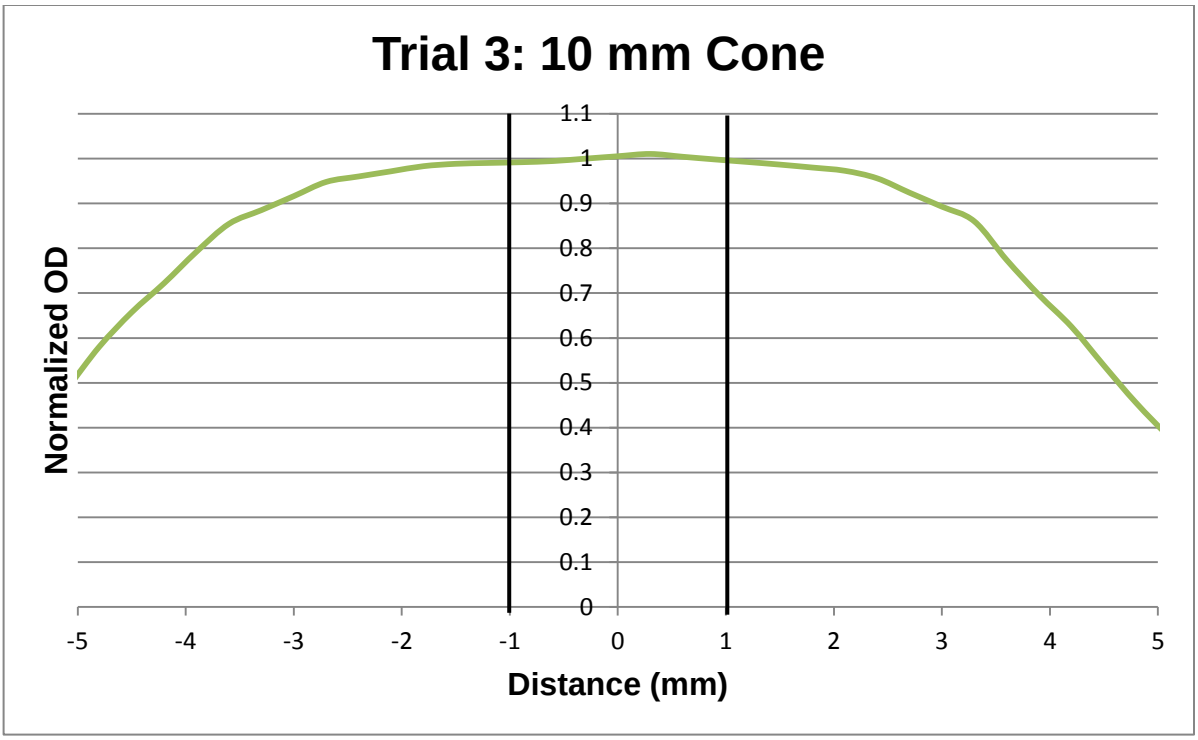

Figure 6.16: Trial 3 dose profile for a 10 mm diameter field.

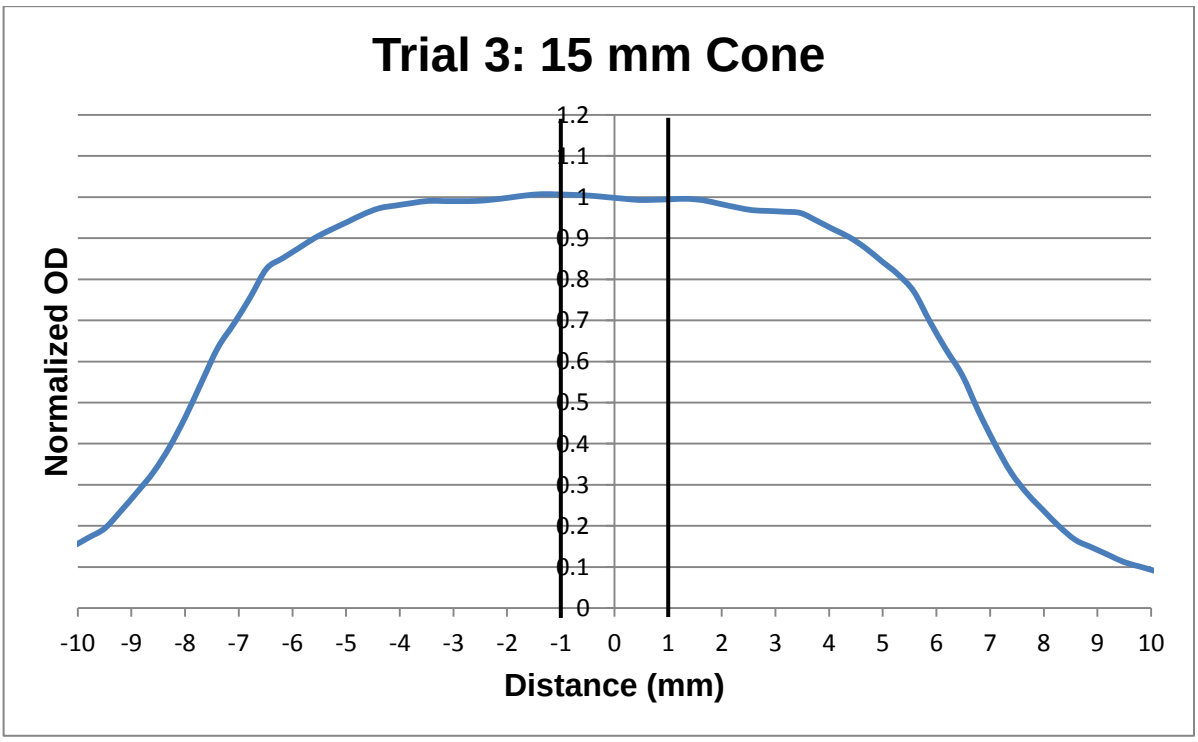

Figure 6.17: Trial 3 dose profile for a 15 mm diameter field.

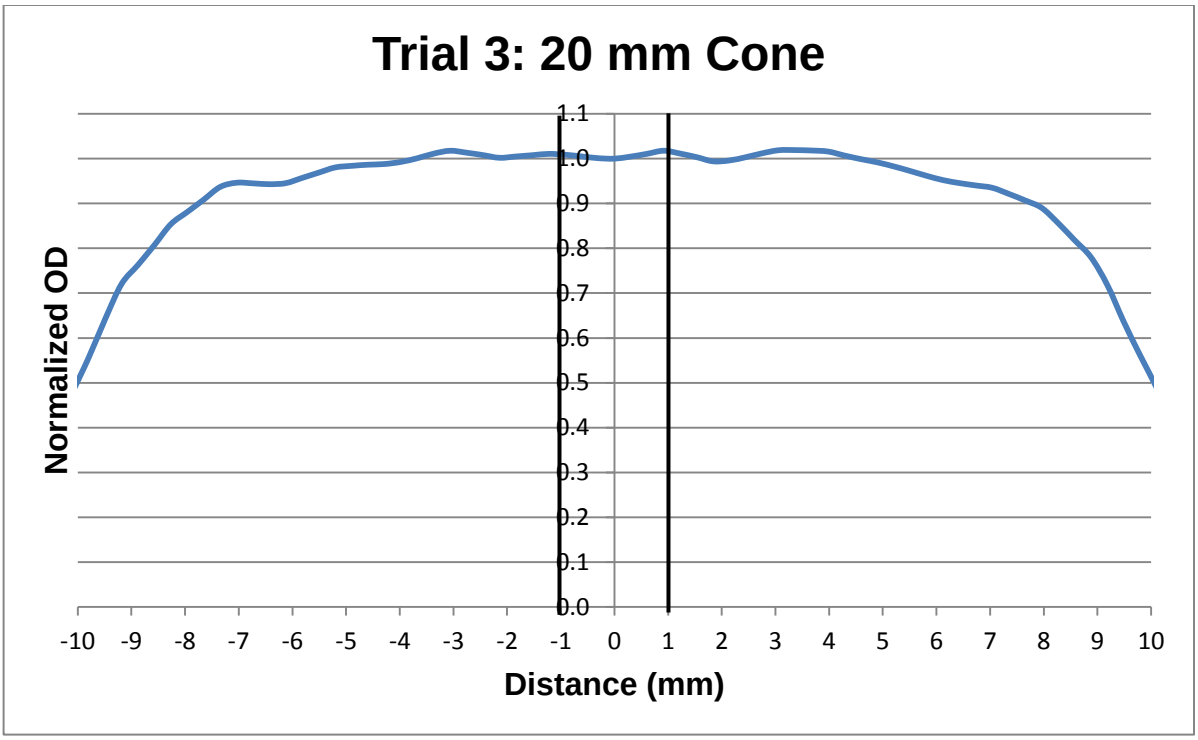

Figure 6.18: Trial 3 dose profile for a 20 mm diameter field.

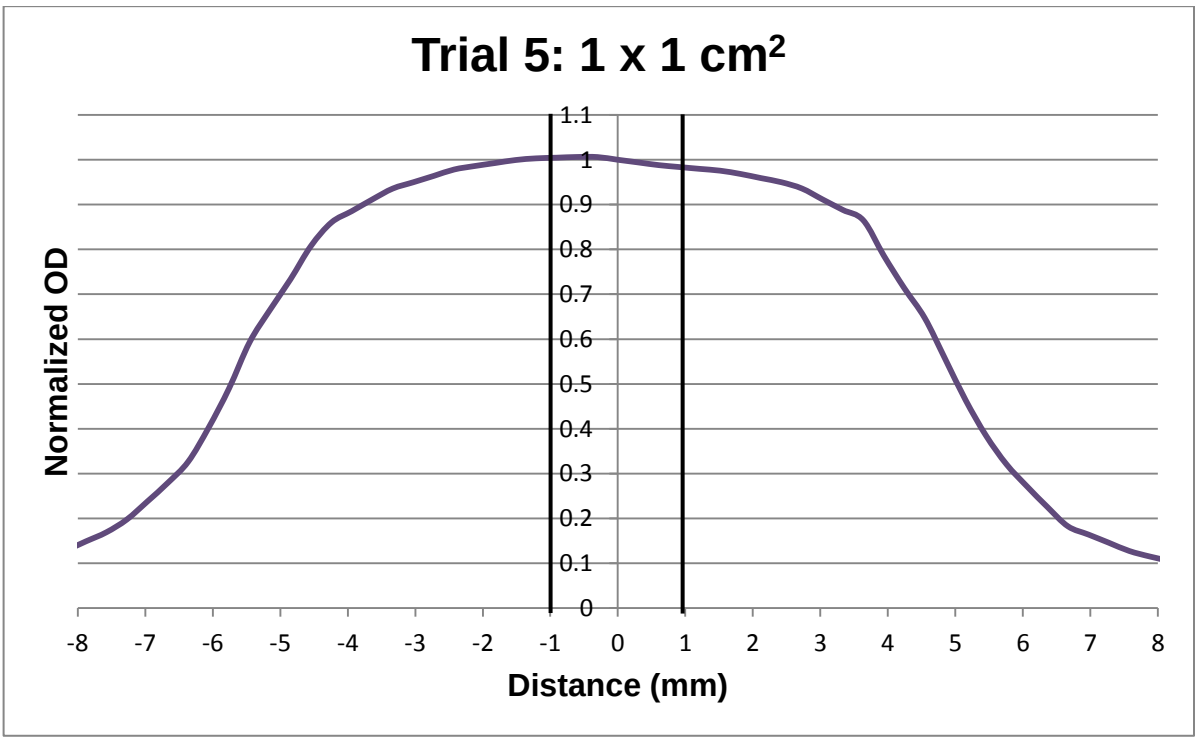

Figure 6.19: Trial 5 dose profile for a 1 x 1 cm^2 field size.

Figure 6.20: Trial 5 dose profile for a 2 x 2 cm^2 field size.

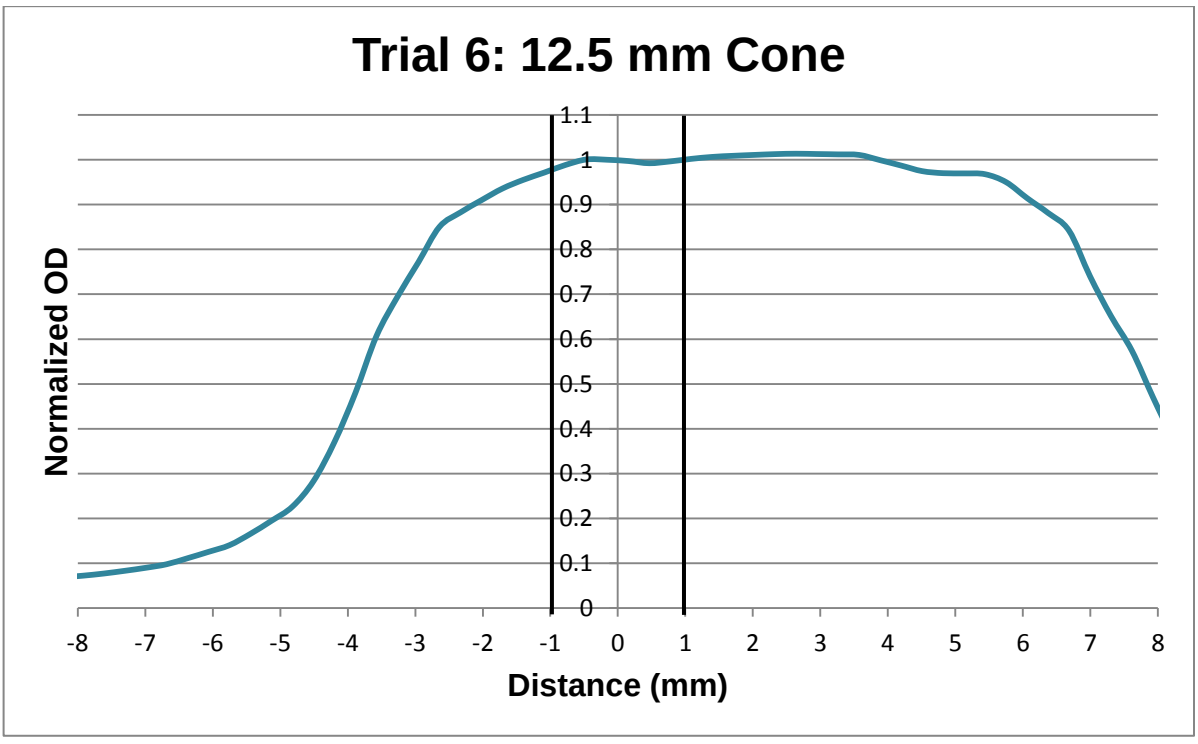

Figure 6.21: Trial 6 dose profile for a 12.5 mm diameter field.

References

1. T. H. Kirby, W. F. Hanson, R. J. Gastorf, C. H. Chu, and R. J. Shalek, “Mailable TLD system for photon and electron therapy beams,” Int. J. Rad. Onc. Bio. Phys **12**, 261-265 (1986).
2. T. H. Kirby, W. F. Hanson, and D. A. Johnston, “Uncertainty analysis of absorbed dose calculations from thermoluminescence dosimeters,” Med. Phys. **19** (6), 1427-1433 (1992).
3. J. Aguirre, P. Alvarez, C. Amador, A. Tailor, D. Followill and G. Ibbott, "WE-D-BRB-08: Validation of the commissioning of an optically stimulated luminescence (OSL) system for remote dosimetry audits, " Med. Phys. **37**, 3428 (2010).
4. J. Aguirre, P. Alvarez, G. Ibbott, and D. Followill, "SU-E-T-126: Analysis of uncertainties for the RPC remote dosimetry using optically stimulated light dosimetry (OSLD)," Med. Phys. **38**, 3515 (2011).
5. P. Alvarez, J. Aguirre, and D. Followill, "SU-E-T-86: Evaluation of the OSLD system for remote dosimetry audits implemented by the RPC," Med. Phys. **38**, 3505 (2011).
6. AAPM Report 54, *Stereotactic Radiosurgery Report of Task Group 42 Radiation Therapy Committee*. (American Institute of Physics, New York, NY, 1995).
7. V. Sturm, B. Kober, K. H. Höver, W. Schlegel, R. Boesecke, O. Pastyr, G. H. Harmann, K. Zum Winkel, and S. Kunze, “Stereotactic percutaneous single dose irradiation of brain metastases with a linear accelerator,” Int. J. Rad. Onc. Bio. Phys. **13** (2), 279-282 (1987).

8. B. Larson, P. H Gutin, and S. A. Leibel, “Stereotactic irradiation of brain tumors,” Cancer **65**, 792-799 (1990).

9. O. O. Betti, C. Munari, and R. Rosler, “Stereotactic radiosurgery with the linear accelerator: treatment of arteriovenous malformations,” Neurosurgery **24** (3), 311-321 (1989).

10. D. B. Kamerer, L. D. Lunsford, and M. Miller, “Gamma Knife: an alternative treatment for acoustic neuromas,” Ann. Otol. Rhinol. Laryngol. **97**, 631-635 (1988).

11. F. M. Khan, *The Physics of Radiation Therapy*. 4th Edition. Lippincott Williams and Wilkins. 2010.

12. S. Kim and J. Palta, “The Physics of Stereotactic Radiosurgery,” *The Principles and Practice of Stereotactic Radiosurgery*, L. S. Chin and W. F. Regine. Springer, 2008. 33-50.

13. S. Kim and J. Palta, “Treatment Planning for Stereotactic Radiosurgery.” *The Principles and Practice of Stereotactic Radiosurgery*, D. M. Shepard, C. Yu, M. Murphy, M. R. Bussiere, and F. J. Bova, 2008. 69-90.

14. R. J. Hamilton, F. T. Kuchnir, P. Sweeney, S. J. Rubin, M. Dujovny, C. A. Pelizzari, and G. T. Chen, “Comparison of static conformal field with multiple noncoplanar arc techniques for stereotactic radiosurgery or stereotactic radiotherapy,” Int. J. Rad. Onc. Biol. Phys. **33** (5), 1221-1228 (1995).

15. R. W. Laing, R. E. Bentley, A. E. Nahum, A. P. Warrington, and M. Brada, “Stereotactic radiotherapy of irregular targets: a comparison between static conformal beams and non-coplanar arcs,” Rad. Onc. **28** (3), 241-246 (1993).

16. D. Schofield and G. Ramey, “The safe implementation of stereotactic radiosurgery in the community hospital setting,” 11 June, 2012.

17. A. S. Shiu, H. H. Kooy, J. R. Ewton, S. S. Tung, J. W. Wong, K. Antes, and M. H. Maor, “Comparison of miniature multileaf collimation (MMLC) with circular collimation for stereotactic treatment,” Int. J. Rad. Onc. Biol. Phys. **37** (3), 679-688 (1997).

18. I. J. Das, P. Francescon, A. Ahnesjö, M. M. Aspradakis, C. W. Cheng, G. X. Ding, G. S. Ibbott, M. Oldham, M. S. Huq, C. S. Reft, and O. A. Sauer, *Task Group Report 155: Small fields and non-equilibrium condition photon beam dosimetry v25*, (2012). (Unpublished)

19. I. J. Das, M. B. Downes, A. Kassaee, and Z. Tochner, “Choice of radiation detector in dosimetry of stereotactic radiosurgery-radiotherapy,” Journal of Radiosurgery **3** (4), 177-186 (2010).

20. S. Li, P. Medin, S. Pillai, and T. Solberg, “SU-EE-A1-02: Analysis of photon beam data from multiple institutions: an argument for reference data,” Med. Phys. **33** (6), 1991 (2006).

21. M. M. Aspradakis, J. P. Byrne, H. Palmans, J. Conway, K. Rosser, J. Warrington, and S. Duane, *Report Number 103: Small field MV photon dosimetry*. (Institute of Physics and Engineering in Medicine, IPEM, York, England, 2010).

22. F. Crop, N. Reynaert, G. Pittomvils, L. Paelinck, C. De Wagter, L. Vakaet, W. De Neve, and H. Thierens, “The influence of small field sizes, penumbra,

spot size and measurement depth on perturbation factors for microionization chambers," Phys. Med. Biol. **54** (9), 2951-2969 (2009).

23. I. J. Das, G. X. Ding, and A. Ahnesjö, "Small fields: Nonequilibrium radiation dosimetry," Med. Phys. **35** (1), 206-215 (2008).

24. G. X. Ding, D. M. Duggan, and C. W. Coffey, "A theoretical approach for non-equilibrium radiation dosimetry," Phys. Med. Biol. **53** (13), 3493-3499 (2008).

25. F. Sánchez-Doblado, P. Andrea, R. Capote, A. Leal, M. Perucha, R. Arráns, L. Núñez, E. Mainegra, J. I. Lagares, and E. Carrasco, "Ionization chamber dosimetry of small photon fields: A Monte Carlo study on stopping-power ratios for radiosurgery and IMRT beams," Phys. Med. Biol. **48** (14), 2081-2099 (2003).

26. F. Crop, N. Reynaert, G. Pittomvils, L. Paelinck, W. De Gersem, C. De Wagter, L. Vakaet, W. De Neve, and H. Thierens, "Monte Carlo modeling of ModuLeaf miniature MLC for small field dosimetry and quality assurance of the clinical treatment planning system," Phys. Med. Biol. **52** (11), 3275-3290 (2007).

27 . F. Araki, "Monte Carlo study of a Cyberknife stereotactic radiosurgery system," Med. Phys. **33** (8), 2955-2963 (2006).

28. K. A. Paskalev, J. P. Seuntijens, H. J. Patrocinio, and E. B. Podgorsak, "Physical aspects of dynamic stereotactic radiosurgery with very small photon beams (1.5 and 3mm in diameter)," Med. Phys. **30** (2), 111-118 (2003).

29. J. U. Wuerfel, “Dose measurements in small fields,” Med. Phys. Int. Jour. **1**, 81-90 (2013).

30. G. S. Ibbott, "MO-A-BRA-01: Credentialing for Clinical Trials," Med. Phys. **37** (6), 3334 (2010).

31. J. Homnick, G. Ibbott, A. Springer, and J. Aguirre, “TH-D-352-05: Optically stimulated luminescence (OSL) dosimeters can be used for remote dosimetry services,” Med. Phys. **35** (6), 2994 (2008).

32. V. V. Antonov-Romanovskii, I. B. Keirum-Marcus, M. S. Poroshina and Z. A. Trapeznikova, *Conference of the Academy of Sciences of the USSR on the Peaceful Uses of Atomic Energy*, Moscow, 1955, USAEC Report AEC-tr-2435.

33. E. G. Yukihara and S. W. S. McKeever, “Optically stimulated luminescence (OSL) dosimetry in medicine,” Phys. Med. Biol. **53** (20), R351-R379 (2008).

34. D. J. Huntley, D. I. Godfrey-Smith and M. L. W. Thewalt, “Optical dating of sediments,” Nature **313** (5998), 105-107 (1985).

35. M. S. Akselrod, V. S. Kortov, D. J. Kravetsky and V. I. Gotlib, "Highly sensitive thermoluminescent anion-defect α-Al_2O_3:C single crystal detectors," Rad. Prot. Dosim. **33**, 119-122 (1990).

36. R. H. Bube, *Photoconductivity of solids*, New York: Wiley (1960).

37. P. A. Jursinic, “Characterization of optically stimulated luminescent dosimeters, OSLDs, for clinical dosimetric measurements,” Med. Phys. **34** (12), 4594-4604 (2007).

38. E. G. Yukihara and S. W. S. McKeever, “Ionization density dependence of the optically and thermally stimulated luminescence from Al_2O_3:C,”Rad. Prot. Dosim. **119**, 206-217 (2006a).

39. B. G. Markey, S. W. S. McKeever, M. S. Akselrod, L. Bøtter-Jensen, N. Agersnap, and L. E. Colyott, “The temperature dependence of optically stimulated luminescence from α-Al_2O_3 :C,” Rad. Prot. Dosim. **65**, 185–189 (1996).

40. E. G. Yukihara, V. H. Whitley, J. C. Polf, D. M. Klein, S. W. S. McKeever, A. E. Akselrod, and M. S. Akselrod, “The effects of deep trap population on the thermoluminescence of Al_2O_3:C,” Rad. Meas. **37** (6), 627-638 (2003).

41. M. S. Akselrod, "Fundamentals of materials, techniques, and instrumentation for OSL and FNTD dosimetry," AIP. Conf. Proc. **1345**, 274-302 (2011).

42. S. W. S. McKeever, M. S. Akselrod, L. E. Colyott, N. Agersnap-Larsen, J. C. Polf, and V. Whitley, “Characteristics of Al_2O_3 for use in thermally and optically stimulated dosimetry,” Rad. Prot. Dosim. **84**, 163–168 (1999).

43. L. Bøtter-Jensen, N. A. Larsen, B. G. Markey & S. W. S. McKeever, "Al_2O_3:C as a sensitive OSL dosimeter for rapid assessment of environmental photon dose rates." Rad. Meas. **27** (2), 295-298 (1997).

44. A. J. J. Bos, "High sensitivity thermoluminescence dosimetry," Nucl. Instrum. Meth. B **184**, 3-28 (2001).

45. R. Hill, Z. Kuncic, and C. Baldock, "The water equivalence of solid phantoms for low energy photon beams," Med Phys **37** (8), 4355-4363 (2010).

46. C. A. Perks, C. Yahnke, and M. Million, “Medical dosimetry using Optically Stimulated Luminescence dots and microStar readers,” 12th International Congress of the International Radiation Protection Association, Buenos Aires, Argentina (2008).

47. A. Viamonte, L. A. da Rosa, L. A. Buckley, A. Cherpak, and J. E. Cygler, “Radiotherapy dosimetry using a commercial OSL system,” Med. Phys. **35** (4), 1261-1266 (2008).

48. P. R. Almond, P. J. Biggs, B. M. Coursey, W. F. Hanson, M. S. Huq, R. Nath, and D. W. Rogers, “AAPM’s TG-51 protocol for clinical reference dosimetry of high-energy photon and electron beams,” Med. Phys. **26** (9), 1847-1870 (1999).

49. R. Alfonso, P. Andreo, R. Capote, M. S. Huq, W. Kilby, P. Kjäll, T. R. Mackie, H. Palmans, K. Rosser, J. Seuntjens, W. Ullrich, and S. Vatnitsky, “A new formulism for reference dosimetry of small and nonstandard fields,” Med. Phys. **35** (11), 5179-5186 (2008).

50. P. Francescon, S. Cora, and N. Satarioano, “Calculation of $k_{Q_{clin},Q_{msr}}^{f_{clin},f_{msr},}$ for several small detectors and for two linear accelerators using Monte Carlo simulations,” Med. Phys. **38** (12), 6513-6527 (2011).

51. P. Francescon, W. Kilby, N. Satariano, and S. Cora, “Monte Carlo simulated correction factors for machine specific reference field dose calibration and output factor measurement using fixed and iris collimators on the CyberKnife system,” Phys. Med. Biol. **57** (12), 3741-3758 (2012).

52. G. Cranmer-Sargison, S. Weston, J. A. Evans, N. P. Sidhu, and D. I. Thwaites, “Implementing a newly proposed Monte Carlo based small field dosimetry formalism for a comprehensive set of diode detectors,” Med. Phys. **38** (12), 6592-6602 (2011).

53. E. Pantelis, A. Moutsatsos, K. Zourari, L. Petrokokkinos, L Sakelliou, W. Kilby, C. Antypas, P. Papagiannis, P. Karaiskos, E. Georgiou, and I. Seimenis, “On the output factor measurements of the CyberKnife iris collimator small fields: Experimental determination of the $k_{Q_{clin},Q_{msr}}^{f_{clin},f_{msr},}$ correction factors for microchamber and diode detectors,” Med. Phys. **39** (8), 4875-4885 (2012).

54. F. Pönisch, U Titt, S. F. Kry, O. N. Vassiliev, and R. Mohan, “MCNPX simulation of a multileaf collimator,” Med. Phys. **33** (2), 402-404 (2006).

55. S. F. Kry, U. Titt, F. Pönisch, D. Followill, O. N. Vassiliev, R. A. White, R. Mohan, and M. Salehpour, “A Monte Carlo model for calculating out-of-field dose from a Varian 6 MV beam,” Med. Phys. **33** (11), 4405-4413 (2006).

56. A. Niroomand-Rad, C. R. Blackwell, B. M. Coursey, K. P. Gall, J. M. Galvin, W. L. McLaughlin, A. S. Meigooni, R. Nath, J. E. Rodgers, C. G. Soares, “Radiochromic film dosimetry: recommendations of AAPM radiation therapy committee task group 55,” Med. Phys. **25** (11), 2093-2115 (1998).

57. M. S. Akselrod, V. S. Kortov, and E. A. Gorelova, “Preparation and properties of α-Al_2O_3:C,” Rad. Prot. Dos. **47**, 159-164 (1993).

58. L. Bøtter-Jensen, S. W. S. McKeever, and A. G. Wintle, *Optically stimulated luminescence dosimetry*, Elsevier, (2003).

59. C. Bassinet, C. Huet, S. Derreumaux, G. Brunet, M. Chéa, M. Baumann, T. Lacornerie, S. Gaudaire-Josset, F. Trompier, P. Roch, G. Boisserie, I. Clairand, “Small fields output factors measurements and correction factors determiniation for several detectors for a CyberKnife and linear accelerators equipped with microMLC and circular cones,” Med. Phys. **40** (7), 071725-1-13 (2013).

60. T. Kron, A Clivio, E. Vanetti, G. Nicolini, J. Cramb, P. Lonski, L. Cozzi, and A. Fogliata, “Small field segments surrounded by large areas only shielded by a multileaf collimator: Comparison of experiments and dose calculation,” Med. Phys. **39** (12), 7480-7489 (2012).

Vita

Christopher Pham was born on March 8, 1988 in Fountain Valley, CA to Minh Pham and Helene Loi. He graduated from the University of California, Berkeley in 2010 with a Bachelor of Science degree in Nuclear Engineering. In August 2011, he entered into the Specialized Master of Science in Medical Physics program at the University of Texas Health Science Center at Houston Graduate School of Biomedical Sciences and M. D. Anderson Cancer Center.